Dissertation

Optimizing single molecule localization microscopy as a tool in chemistry, biology, and physics

Stephan Bergmann

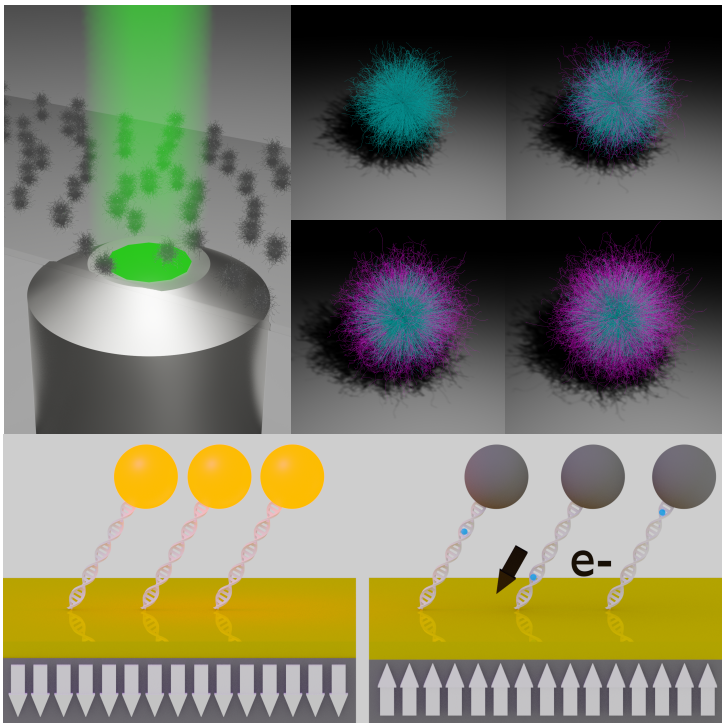

Bielefeld University
Faculty of Physics

Dissertation

Optimizing single molecule localization microscopy as a tool in chemistry, biology, and physics

Author:
Stephan Bergmann

December, 2019

Referees:
Prof. Dr. Thomas Huser
Prof. Dr. Thomas Hellweg

Printed on non-aging paper °° ISO 9706

Contents

1. Introduction

Since the 16th century, the development and improvement of optical microscopes has continued. The first multi-lens microscope was attributed to Zaccharias (1587-1638) and Hans Jannsen (1534-1592) and was able to produce a magnification factor of 10. It took more than 50 years until the microscope was widely used among scientists for drawings of capillary vesicles in the lungs of frogs.. Robert Hooke (1635-1704), known for his bibliography Micrographia [1], modified the proposed basic concept with a biconvex lens, which led to an image suffering from chromatic and spherical aberrations and resulting in a blurred image. Adding a small diaphragm to the optical path could sharpen the image, but most of the light was blocked, resulting in a very dark image. His contribution to the latest microscopes was therefore to add a light source in front of a water-filled glass to generate a diffusely illuminated sample. The Dutchman Anton van Leeuwenhoek was inspired by Hooke's work and obtained improved images with a single lens microscope where he achieved up to 270x magnification. He was not the inventor of the microscope, but his microscopes were the best at the time, allowing him to observe bacteria from tooth scraps.

From that time on, microscopes attracted more and more attention in the scientific community. The achieved image quality benefits in particular from the improved manufacturing processes for objective lenses with higher quality and less contamination. Therefore, lens compositions were produced to reduce the spherical and chromatic aberrations that were the main sources of degradation of the obtained images. Thus, it can be said that the development of new and better microscopes is directly linked to advances in the understanding of cell biology. Even before the theoretical description by Ernst Abbe in 1873 [6], Gioavanni Battist Amici (1786-1863) developed a semispherical objective lens to minimize chromatic aberrations. He also described a relationship between image quality and coverslip thickness and introduced the first water immersion objectives. At about the same time, inventions such as a mechanical x-y table for moving the sample across the objective or stereomicroscopes with two eyepieces were made. All these components can be found in modern microscopes.

Another key to better image quality with microscopes is to improve the contrast of a desired target compared to the rest of the sample. First important observations of a phenomenon later called fluorescence were made by Sir John Herschel in 1845 [2]. He observed distinct colours dispersed by a prism, originating from a

highly concentrated quinine solution, after illumination of sun light passing blue lead glass. Compared to Sir George Stokes, he did not notice that in the case of quinine and also some fluorite crystals, the emission spectrum was shifted to the red side of the colour spectrum [3]. In his publication 1853 he used the term fluorescence [4] for the first time. Only a few years later, in 1858, a fluorescent molecule called fluorescein [5] was synthesized for the first histological staining approaches. From now on, the development of new dyes plays an important role in the further development of different microscopy techniques, as different properties of the fluorescent markers are required. Further milestones on the way to a versatile tool for biomedicine and biology were the discovery of the green fluorescent protein (GFP) [17] and later the possibility to insert the deoxyribonucleic acid (DNA) of GFP to genes responsible for the expression of specific proteins to visualize them. The other way to achieve a specific signal from a desired target is to use antibodies with a directly bound synthetic fluorescent molecule [14].

First observations of specific structures and transport processes in cells, which are important in biology and medicine, were made possible by fluorescent molecules and proteins. But until the beginning of the 21st century, imaging was limited by the diffraction limit. For example, protein interactions on the nanoscale could not be resolved with fluorescence imaging techniques. In 2014 Eric Betzig, William E. Moerner and Stefan Hell [29, 31, 41, 47] were awarded the Nobel Prize for Chemistry. Especially Eric Betzig and William E. Moerner paved the way for today's established methods of single molecule localization microscopy (SMLM) to exceed the diffraction limit. On the one hand, a precise description of the switchover between an on and off state of green fluorescent proteins [35] was necessary. On the other hand, a mathematical description and method for estimating the localization where the fluorescent light originated was also required [25, 30, 86]. Taken together, these two discoveries offer a number of new possibilities in imaging on scales one order of magnitude smaller than before. And it makes it possible to count localizations and link them to the number of molecules that contribute to an image or a specific area of interest.

Therefore, SMLM is the key tool used throughout my dissertation, e.g. to investigate material morphology to synthesize tailor-made polymer particles [232, 244, 260, 282, 288, 301, 317] with smart properties, identification of truncated proteins causing cardiac diseases [249, 250] and possibilities to apply SMLM to probe magnetic fields [314] and how it is not working [258]. Polymer particle with special properties regarding to changes in temperature [44, 49], pH [72, 100, 191], ionic strength [34] or electrochemical potentials [87] respond with a collapse or swelling of the polymer network. This can be used in different application in life science [147, 251, 295, 316] medicine [122, 306, 315], as sensors [310], as nanoparticle carrier [91] or nanoreactors [156, 161]. To tune the response to a certain external stimuli an accurate knowledge of the internal morphology is crucial. So far, the inner struc-

ture and especially the cross-linking density of microgels could only be resolved by small angle neutron scattering (SANS) experiments. The preparations are time-consuming, expensive and the access to the beam lines is limited and associated with waiting times. By using the easy to use and established method of the SMLM it is possible to localize single fluorescent molecules within a single microgel and to draw conclusions about the inner structure through the radial localization density. Due to the possibility and necessity of SMLM working in liquid solvents, the microgels can be observed in swollen state and control over stimulus parameters such as temperature is possible. Recently, great progress has been made with a diffusion approach to studying the polarity of microgels based on an emission shift that depends on the polarity [317] and the influence of the substrate on deformation of microgels mounted on a coated coverslip [308].

For biology and medicine, fluorescence microscopy provides a toolbox for investigating the dynamics and interactions between proteins with high specificity [84], temporal and spatial resolution [138]. Even before Gregor Mendel did his pioneering work on genetics through plant hybridization, Giovanni Maria Lancisi recognized repeated symptoms in a four-generation family suffering from palpitations, dilatation and aneurysm in the right ventricle. This was one of the first written records of a genetic disease. The basic and most common mutations occur in genes coding for proteins in desmosomes [198]. These compartments are important for cell-cell interaction and cell integrity. Detailed knowledge about the interaction of the main proteins could provide crucial information about the main mechanisms of these heart diseases. By using a photoconvertible fluorescent protein fused with the protein of interest, a sparse subset of molecules can be shifted red in their emission so that individual proteins can be localized with high precision [86]. Here it could be shown that for the PKP2 gene encoded plakophilin-2 a shortening of the armadillo repeats leads to a dislocalization within the cell and can be pathological or furthermore lethal. For a single protein it is not necessary to apply SMLM, as the qualitative dislocation of the truncated protein can also be detected by standard wide-field fluorescence microscopy or confocal laser scanning microscopy. However, in order to investigate the effects and interaction of proteins, it is necessary to use super-resolution techniques due to the very narrow distances within the desmosome complex. A truncated protein that is still located at the same position as the unmodified protein, but the cell integrity might be distorted by a weaker protein-protein interaction at the desmosome. In a further step, different mutations in the genes will be investigated by artificial constructs in cell culture and compared with samples from heart muscle sections of patients with this disease. The estimated prevalence for the public is about 1 to 5000 [190] and is therefore of high relevance for the understanding of the underlying mechanisms.

The use of super-resolution microscopy can also push the knowledge of very small magnetic domains visualized with wide-field methods to new limits. An established

method for indicating the magnetization direction is the Kerr magneto-optical effect [220]. Here, the polarization properties of light are used to visualize the change in polarization caused by the magnetization of a ferromagnetic surface. The detection is realized by two polarizers with a perpendicular orientation to each other. Due to the diffraction limit it is only possible to detect different magnetizations in the microscopic, but not in the nanoscopic range. Therefore, an idea to overcome the diffraction limit with SMLM was based on a publication in which a magnetic field was used to increase the photon yield [229]. According to the assumption that an external magnetic field increases the number of photons emitted, it would be possible to count them with the tools of SMLM. By using an immobilized layer of fluorophores to produce a map of emitted photons in correlation with a known magnetic field, a calibration measure can be generated. The expected change of the emitted photons was not reproducible in single molecule experiments, so that the same mass measurements are performed in a fluorimeter. The experiment revealed a systematic error due to the reflectivity of the shiny surface of the neodymium magnet, which led to an increased detected fluorescence. However, a promising way to explore magnetic domains could be the use of special chiral molecules acting as spin filters [152, 215, 283, 314]. By combining the properties of chiral molecules with quantum dots that generate exciton pairs by ultraviolet illumination, the luminescence of the quantum dot can be used as a measure of the magnetic field direction [241]. Problems encountered in the realization of a method for measuring magnetic domains with different magnetization on the nanoscale were the weakness of the effect for single quantum dots and the microscope stability in the magnetic field.

Overall, in my thesis I was able to show the variety of issues that can be addressed with the use of SMLM and the different measures available through the localisation process. For the study of microgel morphology, the number of localizations per ring area can be used as an estimate of density. Using symmetry, this 2D information can be converted into 3D information [272, 276]. This uncomplicated and easy-to-use method provides a way to obtain morphology information without integrating a fluorescence labeling system that changes the network structure and properties of the microgel. Different architectures can be studied and microgels can be fine-tuned more easily. With the resolution capabilities of SMLM, the dislocation of desmosomal proteins can be resolved with higher precision than with conventional wide-field fluorescence microscopy or confocal laser scanning microscopy. For ongoing studies on genetically caused heart diseases, knowledge of the interacting proteins is of great interest in order to obtain information on which combinations of types and combinations lead to pathological changes in the heart muscle. Not only the correct position of the protein is important for cell-cell interaction, but also the total number of proteins that can be counted in SMLM [212, 305] can be a key for cell stability. The number of photons emitted can also be used

to obtain information about material properties, such as magnetization. Overall, SMLM is therefore a versatile toolbox for counting localizations or even molecules, the underlying photon number that can change due to external influences, and perhaps the most widespread application of reconstructing images based on estimated localizations to bypass the diffraction limit and gain new insights in completely different subject areas.

2. Theoretical background

2.1. Widefield microscopy

2.1.1. Luminescence of fluorescent molecules, nanodiamonds and semiconductor particles

Over the past 30 years, fluorescence microscopy has been continuously developed by improving standard fluorescence markers, developing new luminescence probes and novel microscopy techniques. Fluorescence microscopy has the ability to highlight molecules and structures of interest with a high contrast compared to a dark background. Fluorescence emitters can be excited by absorption of a photon, where one photon transfers the energy E according to Planck's relation

$$E = h\nu = \frac{hc}{\lambda}, \tag{2.1}$$

with h Planck's constant, c the speed of light, ν the photon frequency and λ the photon wavelength in vacuum. The transition of an electron from the ground state to an excited state due to the energy transfer by absorption of the photon follows the Franck-Condon principle [8–10], whereby transitions to an vibrational state with a high overlap of wave functions are preferred. By predominantly non-radiating transitions the electron relaxes into the ground state of the first excited electronic state, this event is called internal conversion. From this state, energy can be released in the form of an emitted photon, where the energy corresponds to the difference between the different states, called fluorescence. Due to the non-radiative transitions into the first excited singlet state, the emitted photon has a longer wavelength than the light used to excite the molecule. This can be seen directly from Planck's equation, 2.1. This spectral shift between the excitation wavelength and the emission wavelength is called Stokes shift [3] (see figure 2.2 **A**).

The processes within a molecule can be summarized in a so-called Jablonski diagram (see figure 2.1 **A**). By absorption of a photon an electron can be brought from the ground state S_0 to the first excited state of the dye molecule, the singlet state S_1 or even to a higher singlet state S_2, S_3... (blue arrows). Radiation-free processes which are called internal conversion and vibration relaxation (black wave arrow and grey wave arrow) occupy the ν_0 vibrational state of the S_1 state. From

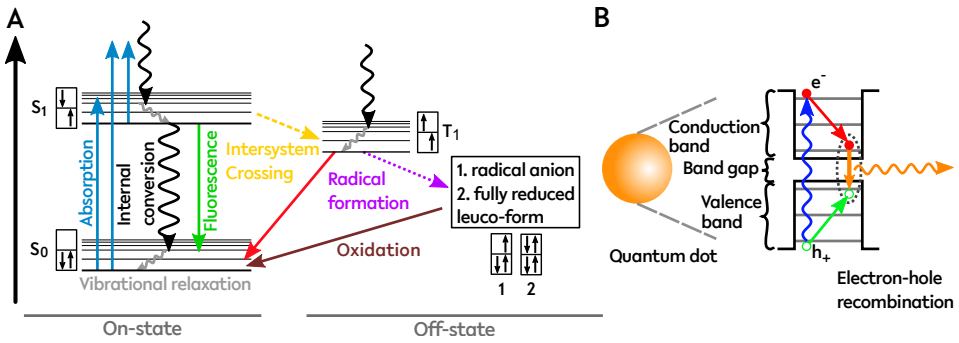

Figure 2.1.: The subfigure **A** shows an extended Jablonski diagram with the relaxation path of fluorescence, phosphorescence, non-radiative paths due to internal conversion or oxidation of reduced dye molecule states. The boxes represent the participating HOMOs and LUMOs with their representative electron spins up and down. The subfigure **B** shows a semiconductor quantum dot with its associated path forming an exciton pair with a subsequent recombination of the electron-hole pair under emission of a photon.

here, the molecule can be excited to even higher states or return to the ground state in two different ways. Again, an internal conversion can take place, which leads to a radiation-free transition into the singlet ground state S_0. The desired path back to the ground state S_0 is coupled with the emission of a spectrally red shifted photon, compared to the wavelength of the absorbed photon. All these processes take place on different time scales, including a range of femtoseconds (10^{-15} s) for the absorption process, picoseconds (10^{-12} s) for the internal conversion, and nanoseconds (10^{-9} s) for the fluorescence lifetime.

The boxes next to different energy states represent the highest occupied molecular orbit (HOMO) of the unexcited dye molecule and the lowest unoccupied molecular orbit (LUMO) as well as the electron spin. In the initial state, the fluorophore has two distinguishable electrons in HOMO due to its spin. The excitation lifts one of the electrons to the LUMO. During the absorption process, one electron is transferred from HOMO to LUMO and returns to the former HOMO.

A competing mechanism for fluorescence is phosphorescence, which occurs from the transition to the triplet state T_1, where the electron spin of the excited electron inverts and the transition back to the ground state S_0 is forbidden according to Pauli's principle, where two fermions must be distinguishable by at least one quantum number. The electron thus remains in the triplet state, which has a long lifetime of up to several seconds compared to the singlet states. A mechanism comparable with the fluorescence pathway is also possible from the T_1 state, in which an even further red shifted photon is emitted. This process is called phosphores-

cence. Other possible transitions during the lifetime of the triplet state are coupled to the chemical environment. During the occurrence of the triplet state, a higher reactivity to a radical anion or a completely reduced leukoform of the dye is given in the presence of a thiol. Both the radical anion form and the completely reduced leukoform return to the ground state by oxidation, which is a radiation-free process. If the molecule is not oxidized, it remains in a long-lived, non-emitting, dark state with a lifetime of up to several seconds [61, 127]. Due to the higher reactivity in the triplet state, it is also more likely that the molecule is photobleached or photodestroyed. Special buffer conditions can provide a higher surviving fraction of fluorescent molecules over time [52]. The energy loss due to non-radiating vibration relaxation in the excited S_1 and ground state S_0 can be detected as a red shifted photon compared to the photon that excited the molecule. The corresponding energy can be calculated from Planck's equation 2.1 and results from the energy difference of

$$\Delta E_{Photon} = hc \left(\frac{1}{\lambda_{out}} - \frac{1}{\lambda_{in}} \right). \tag{2.2}$$

This energy loss is specific for every molecule and is called Stokes shift, which is the fundamental effect which enables fluorescent microscopy with the known low background by efficiently separating the excitation light from the emission signal. A widely used fluorescent probe, in particular for SMLM, is Alexa Fluor 647. The absorption and emission spectrum including the Stokes shift is shown in figure 2.2 **A**.

Further prominent luminescent nanoparticles are so-called quantum dots (Qdots), which consist of a semiconductor material that forms a valence and conduction band with a band gap (see figure 2.1 **B**), which corresponds to the emission wavelength that can be described by a particle in a box potential. Therefore, the desired emission wavelength can be tuned with the Qdot size. General properties can be controlled during Qdot synthesis by varying the used materials, such as lead sulfide (PbS) or cadmium selenide (CdSe). These types of Qdots are called core type Qdots. An additional shell around the Qdots core (Core-Shell Qdots) changes the transition from a bright and a complete dark state to a bright and a grey state and even to longer on-periods [233]. Qdots are used in fluorescence microscopy for various purposes, e.g. as reference markers for drift correction or directly as a fluorescence markers. One of their biggest advantages is the higher photostability over long time scales [103, 124, 135] compared to conventional organic fluorescent dyes. In addition, their unique blinking properties can be used for advanced fluorescence microscopy techniques to improve image resolution beyond Abbe's proposed limit (see chapter 2.1.4). Another interesting feature of Qdots is the possibility of multicolor imaging with a single laser wavelength for excitation, since Qdots of different sizes and emission wavelengths share a similar absorption spectrum in the far UV range (see figure 2.2 **B**).

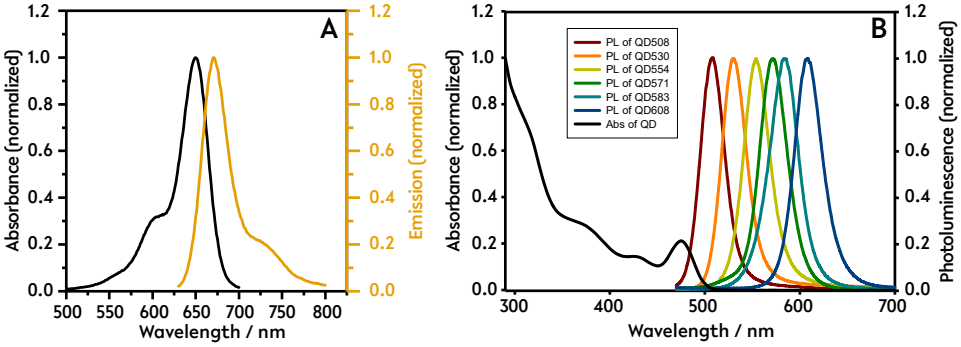

Figure 2.2.: Quantum dots and fluorescent organic dyes have unique excitation and emission properties. **A** shows the excitation and emission spectrum of Alexa Fluor 647 (digitized from [294]), a widely used fluorescent dye in SMLM that belongs to the group of cyanine dyes. **B** shows the normalized absorption of cadmium telluride-based quantum dots (Qdots). One advantage of using Qdots for fluorescence microscopy is the broad and emission-independent absorption in the ultraviolet and violet regions of the visible spectrum. This enables multi-color imaging with a single excitation wavelength (adapted from [162]). Unlike Qdots, the absorption spectrum of organic dyes is unique for each dye.

Another alternative to organic dyes are nanodiamonds, i.e. nanoscale diamonds with multiple nitrogen vacancies (NV) that act as fluorescent sources [157]. In contrast to Qdots, nanodiamonds do not carry out intrinsic blinking events and show a very stable and environmentally unaffected fluorescence. The fluorescence intensity depends on the number of NVs within a single nanodiamond. Another feature is based on the unique energy level structure of the nanodiamond. Without a magnetic field the energy levels of different spins are degenerated, but within a magnetic field, a splitting of an energy level [200] occurs. Depending on the external magnetic field strength this effect is called anomalous Zeeman-effect or Paschen-Back-effect. Using a spin-dependent luminescence technique, luminescence decreases when an external microwave field is resonant to the splitted and populated energy level. Depending on the magnetic field strength, the two resonances appear at different frequencies, which can be used as a measure of the magnetic field [324]. This effect is called optically detected magnetic resonance (ODMR) [36].

2.1.2. General widefield fluorescence setup

A schematic drawing of a minimalist fluorescence microscope is shown in figure 2.3 **A**. Typically a microscope consists of a light source, a lens to focus on

the back focal plane of the objective lens, a dichroic mirror to reflect the excitation light towards the objective lens and separate the excitation light from the emitted fluorescence, a tube lens and a detector, here a camera.

One of the most important components in the microscope is the objective lens, which defines the achievable resolution of the microscope and is important to create different illumination schemes. Therefore, depending on the lateral focus position of the excitation beam to the back focal plane of the objective lens, it is possible to change the illumination scheme from epi fluorescence (figure 2.3 **D**) over a highly inclined and laminated optical sheet (HILO) [128] (figure 2.3 **C**) to total internal reflection (TIR) [21] (**B**). For TIR special properties of the objective lens are required. In detail, the mechanism of TIR is described in the following section.

2.1.3. Illumination schemes

Many modern commercial fluorescence microscopes are inverted microscopes in which the sample is illuminated from below. Therefore, the same objective lens is used to illuminate the sample and to collect the fluorescence signal. From above, a white light source is installed in combination with a condenser to gain a white light transmission image in addition to the fluorescence image. With this setting, typically three different illumination systems can be achieved as mentioned above (figure 2.3). Today, more advanced illumination systems can be used to get an optical sectioning [66, 167] or to create a 4π configuration to achieve self-interference of a single photon source and the ability to accurately determine the axial position of the emission [138].

Epi illumination is achieved by focusing the excitation beam on the center of the back focal plane of the objective lens. This results in a collimated beam that illuminates the entire volume above the objective lens (see figure 2.3 **D**). Thus it is possible to detect a fluorescence signal through the entire sample. The down side of this illumination technique is the out-of-focus fluorescence, which decreases the overall signal to background ratio. In addition these molecules are excited and can be photobleached and destroyed, and are not available for further imaging. This can lead to a signal degradation over time, which is a problem especially with long-term observations of the sample of interest.

By moving the excitation beam to the edge of the objective's back focal plane, the illumination beam forms an inclined excitation beam within the specimen. Depending on the numerical aperture of the objective lens, a strongly inclined and laminated optical sheet (HILO) [128] is formed near the coverslip. Compared to the epi illumination scheme, a small area above the coverslip is illuminated which contributes to the final fluorescence image and provides a better signal-to-background ratio due to the smaller excitation volume above the objective lens. A rough estimate of the light sheet's thickness dz can be given by the diameter R of

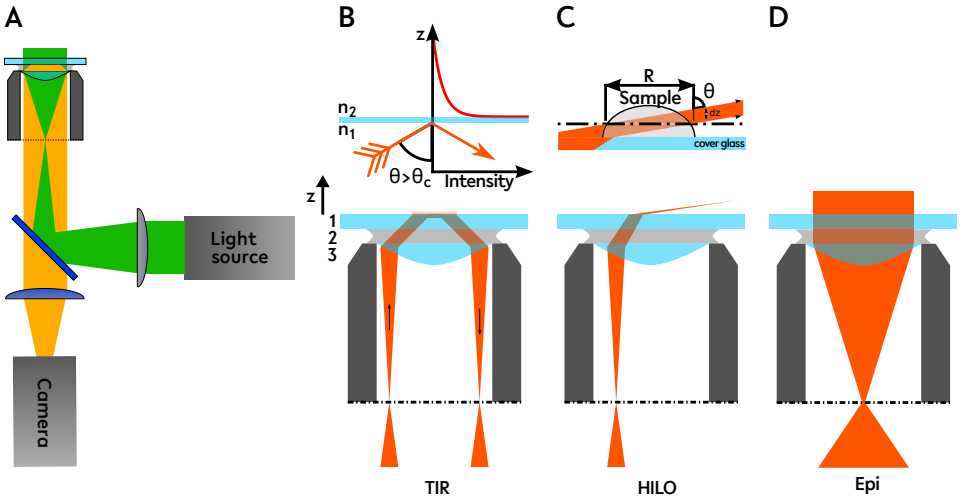

Figure 2.3.: **A** shows a schematic fluorescence microscope in which the excitation pathway is highlighted in green and originates from the light source. The fluorescence (yellow) emitted by the sample is collected by the same objective lens that is used to illuminate the sample. The excitation and fluorescence light are spectrally separated by the Stokes shift through a filter or in this case a dichroic mirror (blue), which acts as a mirror or is transparent to light of a specific wavelength. Finally, the tube lens focuses the fluorescence light onto a detector, in this case a camera. The sub-figure **B** shows the illumination scheme of total internal reflection (TIR), in which the electric field of the reflected excitation beam decreases exponentially above the coverslip and thus only a few hundred nanometers of the sample are excited. For the highly inclined and laminated optical sheet(HILO), the excitation beam is slightly moved to the center of the objective lens and forms a tilted narrow light sheet near the coverslip (**C**). The epi-fluorescence shown in **D** illuminates the entire sample volume above the objective lens.

the illuminated surface and θ_{Hilo}, which is the angle between the vertical surface of the inclined light sheet and the coverslip (see figure 2.3 **C**).

$$dz \approx \frac{R}{\tan\theta_{\mathrm{Hilo}}} \tag{2.3}$$

When the excitation beam is moved further to the edge of the objective lens, a total internal reflection occurs at the interface between the coverslip and the overlying medium of the sample. Typically, coverslips are made of borosilicate glass with a refractive index of $n = 1.518$, while water has a refractive index of $n = 1.33$ under ambient conditions. The majority of the samples examined are

polymer particles, so-called microgels with different compositions. Depending on the environmental temperature microgels exhibit different properties based on a volume phase transition. Therefore, the refractive index strongly depends on the state of the microgel. In the swollen state, the refractive index is close to $n = 1.34$, which corresponds to the refractive index of water, for a wavelength of about 600 nm at a temperature of $30\,°C$. The increase in temperature leads to a collapse of the microgel and an increasing refractive index up to $n = 1.39$ [130] is observable. The assignment of a general refractive index to biological samples is also difficult because different regions in a cell have different refractive indices from $n = 1.36$ for cytoplasm [101] to $n = 1.60$ for lysosomes [238]. The refractive index plays an important role for the occurrence of a total reflection according to Snell's law, at which a certain angle, the critical angle θ_c, must be reached between the plane perpendicular to the surface boundary and the incident beam.

$$\theta_c = \arcsin\left(\frac{n_2}{n_1}\right) \tag{2.4}$$

Here, n_2 is the medium above the coverslip, which can be the environment of the sample or the sample itself. For a high numerical aperture objective lens, the immersion medium n_1 is in most cases oil with a refractive index of $n = 1.518$, which corresponds to the refractive index of the coverslip. As shown in figure 2.3 **B**, the intensity of the remaining electromagnetic field above the coverslip decreases exponentially and its intensity I can be calculated by

$$I(z) = I_0 \exp\left(-\frac{z}{l}\right), \tag{2.5}$$

where z is the height above the coverslip, l the penetration depth and I_0 the intensity directly at the interface. The penetration depth l is linked to the excitation wavelength λ_{exc} in vacuum and the refractive indices n_1, n_2 and the angle θ between the perpendicular surface to the surface boundary and the incident excitation beam.

$$l = \frac{\lambda_{exc}}{4\pi\sqrt{n_1^2 \sin^2(\theta) - n_2^2}} \tag{2.6}$$

Based on the used angle of the incident beam the penetration depth can be adjusted down to ten nanometers [131], but it is typically in the range of 100 nm to 200 nm. The advantage of this very thin range is the enhanced signal-to-background ratio due to nearly missing fluorescent background from above the focus. However, the total internal reflection scheme has the disadvantage of being limited to the volume close to the coverslip's surface.

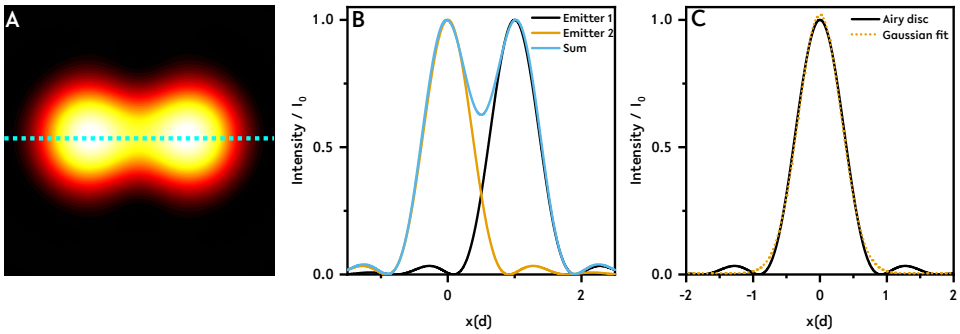

Figure 2.4.: A shows the resulting diffraction-limited image of two point emitters in the configuration of the Rayleigh criterion. The emission distribution of the first emitter is described by a Bessel function of the first type and first order. The second emitter is placed in the intensity minimum of the first emitter. In **B** a line profile (from cyan dotted line in **A**) is calculated for the summed intensities (blue) and the intensities of each emitter (first emitter black and second emitter orange). For later use, **C** shows the approximation of the airy disk by a Gaussian distribution, where an estimate of the achieved resolution can be given by the full width at half maximum (FWHM) of the Gaussian fit.

2.1.4. Resolution limit in microscopy

Based on observations with a diffraction grating Ernst Abbe found in 1873 [6] that the ability of microscopes to resolve two lines from each other depends on the used wavelength λ of the light and the ability of the objective lens to collect light from a very large angle θ. For the well known and famous formula

$$d = \frac{\lambda}{2 \cdot n \cdot \sin(\theta)} = \frac{1}{|k_{Abbe}|}, \tag{2.7}$$

he assumed that the grating is illuminated with a coherent light source at the angle θ and a lens with the ability to collect light from the same half aperture angle θ. In equation 2.7 d corresponds to the grating constant that can be resolved by the optical system. In the image of the frequencies transmitted by the optical system, $|k_{Abbe}|$ refers to the maximum spatial frequency transmitted. Typically the expression $n \cdot \sin\theta$ is summarized by the numerical aperture NA. Here, n is the refractive index of the medium between the last objective lens and the observed object. The given equation 2.7 is only valid if the sample is illuminated with a condenser lens corresponding to the numerical aperture of the objective lens. A

more general expression of equation 2.7 is

$$d = \frac{\lambda}{\mathrm{NA}_{\mathrm{condenser}} + \mathrm{NA}_{\mathrm{objective}}}. \tag{2.8}$$

In the sense of fluorescence microscopy, the observed objects are single points and incoherent fluorescent emitters, emitting a spherical wave. Only a part of this wave can be translated into a planar wave by the objective lens due to its limited angular aperture, with each point itself being the origin of a Huygens wave front. Due to the loss of information, the point emitter cannot be fully restored by the optical system. The resulting intensity distribution is called point spread function (PSF). Adding a lens to focus the planar wave into a single point results in a constructive interference where the optical path length is the same for all wavelets. Around this point, the path lengths are different and destructively interfere with each other, resulting in an interference pattern of the so-called airy disc. The field intensity I can be expressed as

$$I(\theta) = I(0)\left(\frac{2J_1\left(\frac{2\pi a}{\lambda}\sin\theta\right)}{\frac{2\pi a}{\lambda}\sin\theta}\right), \tag{2.9}$$

where $I(0)$ is the center intensity, J_1 is the first order Bessel function, and a is the opening radius. The first minimum is at $\sin\theta \approx 1.22\frac{\lambda}{2a}$. According to Lord Rayleigh's definition, two point sources can be distinguished if the maximum of one point source is in the minimum of the other point source. From this qualitative explanation and the intensity distribution described by equation 2.9, it is possible to define the minimum distance d at which two emission points are still distinguishable.

$$d = 1.22\frac{\lambda}{2\mathrm{NA}} \tag{2.10}$$

If two single emitters are positioned at the minimum distance d (see figure 2.4 **A**) defined in the Rayleigh criterion, a decrease of the summed intensity of 27.4% can be seen between the two emitters compared to the maximum intensity of a single emitter (figure 2.4 **B**). For the later described SMLM method in chapter 2.3, it is important to approximate the position of emitters by the acquired PSF of a single emitter to bypass the diffraction limit. In figure 2.4 **C** it can be seen that the Gaussian distribution approximates very well the intensity distribution of the airy disk. This allows a faster computation in comparison to calculation of the airy disc via the more complicated Bessel function. Since samples of interest are three-dimensional objects, it is necessary to consider the resolution limit of microscopes in axial direction. Here, a minimum distance z_{min} is defined as the objective lenses

travel distance from the maximum to the first intensity minimum [92].

$$z_{\min} = \frac{2\lambda}{\mathrm{NA}^2_{\mathrm{objective}}} \tag{2.11}$$

Like for lateral approach to bypass the diffraction limit with SMLM, there are possibilities to overcome the resolution limit in axial direction, which is described for single molecule localization methods in chapter 2.3.3. Until now, the optical system is the only limitation for the resolution, but in addition the detector and the sample itself plays a not negligible role for the image quality of a microscope. Especially in SMLM, the back-projected pixel width a is important to satisfy the Nyquist-Shannon sampling criterion, which generally states that the recorded frequency must be sampled at twice the frequency to be detected [11, 16]. For a camera, the pixel width must be selected to be at least half the system resolution. Thus, the criterion must also be applied to structures captured by the diagonal of the pixel detector, where the pixel width to reach the sampling criterion is as set forth below

$$a = \frac{d}{2\sqrt{2}}. \tag{2.12}$$

On the other hand, the specimen must also satisfy the requirements of the Nyquist-Shannon sampling criterion. For the one-dimensional case, the mean distance between two labels must be smaller than the shortest detectable spatial frequency f_{max}, which can be related to the early resolution measurements Ernst Abbe performed with a grid. Therefore, the shortest detectable space period is $T_{min} = 1/f_{max}$. The minimum required label density ρ is linked to the dimension D of the image so that $\rho \geq (2/T_{min})^D$ is fulfilled [126]. But this is only the necessary condition and not a sufficient one. In recent studies, the proposed distance between the molecules should therefore be one fifth of the system resolution [218, 236].

Image formation

From earlier observations that an optical system is limited by the transmission of frequencies, a point-like emitter has an intensity distribution of an airy disk. Theoretically, the image formation can be described as a convolution of the point-like emitter with the characteristic PSF of the system. A complete image g consists of distributed single emitter f which is convoluted with the microscopes specific PSF.

$$g = f \otimes \mathrm{PSF} \tag{2.13}$$

In Fourier space the convolution is a multiplication

$$\mathcal{F}\{g\} \propto \mathcal{F}\{f\} \cdot \mathcal{F}\{\mathrm{PSF}\}, \tag{2.14}$$

With the knowledge of the PSF or the optical transfer function (OTF), it is possible to reverse the convolution with the reverse operation named deconvolution. The OTF is defined as the Fourier transform of the PSF. It is important to note that the OTF has a cut-off frequency which is also linked to the achievable resolution of the microscope. From a mathematical point of view it should be possible to restore the original image, but effects like noise or motion blur will change the resulting deconvoluted image.

2.1.5. Photochemistry and photophysics of organic fluorophores and fluorescent proteins in specialized buffer

After the excitation process of a fluorescent molecule, as shown in figure 2.1 **A**, different paths back to the ground state S_0 are possible. Through the use of reducing agents (ascorbic acid, n-propyl gallate [109, 110], Trolox [95], ß-mercaptoethanol [22, 166] and oxidizing agents (methylviologists, Trolox quinone), several dyes from the different dye classes (see figure 2.5) can be reduced from the triplet state to a long-lived intermediate radical state in which no fluorescence occurs. These states are called dark- or off-states. In multi-color experiments, two or more different organic dyes or fluorescent proteins are used, whereby the emission spectra are well separated from each other and no spectral crosstalk occurs. Therefore, it is necessary to match the right chemical conditions to achieve a low temporal fluorescence density to obtain single localizations for all fluorescent dyes or proteins in the on-state. A key role in maintaining the off-state of the fluorescent molecule is to remove the molecular oxygen from the surrounding buffer medium. This can be achieved by various chemical reactions. There are two common oxygen scavenging methods. The first is based on glucose oxidase in combination with catalase (GODCAT) [62, 63, 89, 105, 106] and the second on protocatechuate dioxygenase (PCD) and protocatechuic acid (PCA) [48]. The GODCAT system was first developed in 1987 by Englander et al. [24] to generate anoxic conditions in biochemistry. In 1990, Harada and coworkers [26] used the GODCAT oxygen scavenging system in a composition comparable to that used by most research groups as *d*STORM image buffers. Their goal was to reduce the effect of photobleaching by removing oxygen for longer observation times of actin filaments. An advantage of using the PCD/PCA system is the long-term activity of the enzymatic reaction, the pH stability [177] and the fact that during the reaction no hydrogen peroxide is formed, which is very reactive and can lead to the destruction of the fluorescent molecules.

The standard imaging buffer for *d*STORM experiments, proposed by Heilemann et al. in 2008 [115], performs well for Alexa Fluor 647, which is a member of cyanine dyes, but does not perform well e.g. for Alexa Fluor 488, which belongs to the dye group of xanthenes [28, 300]. So it is necessary to find a compromise in the buffer conditions for the used fluorescent dyes, especially for the needs of

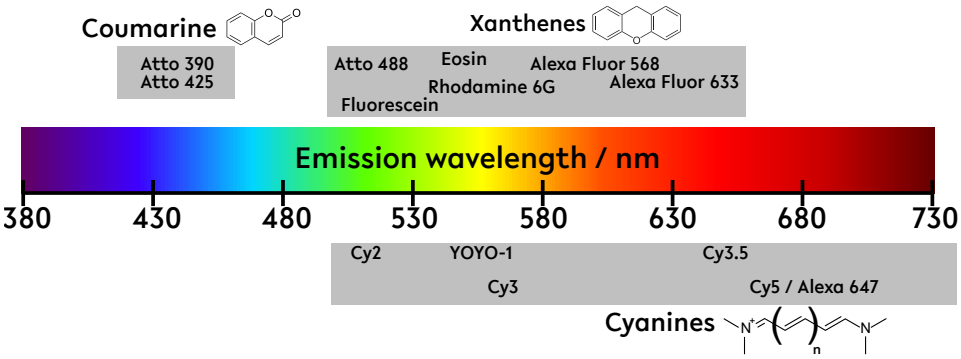

Figure 2.5.: Overview of organic fluorescent dyes in the entire visible range. The different dye families (coumarin, xanthene and cyanine) contain prominent dyes that are common in fluorescence microscopy. The color-coded bar visualizes the main emission wavelength of these dyes. Different regions in the visible emission spectrum are covered by different dye classes. Coumarine dyes are prominent in the blue emitting region, whereas xanthene and cyanine dyes cover the emission spectrum from green to near infrared.

dual- or multi-color experiments. A good overview which organic fluorophores can be used for SMLM under certain conditions is given by Dempsey et al. [150] and even more specific for the combination of Alexa Fluor 647 and Bodipy FL by Bittel et al. [277]. An earlier approach to improve the resolution in SMLM with Alexa Fluor 647 is the quenching of the triplet state by adding cyclooctatetraene [188] to gain more photons during the on-state. The kinetics between reduction from the triplet state and the triplet state itself can be influenced by the amount of reducing agents like β-mercaptoethylamine, β-mercaptoethanol or ascorbic acid. Via oxidation or UV illumination (405 nm) it is possible for some dyes to return back to the singlet state S_0 and fluorescence can take place again. A new approach by Nahidiazar et al. [243] is the usage of oxyrase, a deoxygenating reagent made from oxygen consuming membrane fractions of Escherichia coli [60], and DL-lactate as a substrate which also works as an antioxidant and radical scavenger [45]. To achieve a sufficient blinking of dyes from different dye classes the mentioned buffer shows a good compromise between the widely used Alexa Fluor 647 from the dye class of cyanines and the mostly used Alexa Fluor 488 from the xanthene dye class [42, 300].

All these buffer systems have to deal with the limitation of a refractive index of approximately 1.33. In comparison intracellular compartments of a cell have a refractive index between 1.355 in the cytosol and up to 1.600 in the lysosomes [238]. For the usage of high numerical aperture objective lenses it is favorable to have a

Table 2.1.: Small selection of photoswitchable fluorescence proteins. After excitation with the mentioned conversion wavelenght, typically 405 nm, the protein changes its fluorescence towards red shifted wavelengths.

Fluorescent protein	Conversion wavelength	Pre-conversion		Post-conversion	
		Absorption maximum	Emission maximum	Absorption maximum	Emission maximum
Dendra2[102]	$\sim$ 400 nm	490 nm	507 nm	553 nm	573 nm
mEosFP *thermo*[82, 98, 213]	$\sim$ 400 nm	505 nm	516 nm	569 nm	581 nm
mMaple[168]	$\sim$ 400 nm	489 nm	505 nm	566 nm	583 nm
PSmOrange2[176]	489 nm	546 nm	619 nm	561 nm	651 nm

refractive index match between sample and surrounding medium, especially for measurements of thicker samples and acquisition of 3D data. Due to the refractive index mismatch a squeezed or stretched image appears along the axial direction. But depending on the calibration method distortions can be taken into account [278, 311]. A new approach is the usage of a high fraction of glycerol with sodium sulfite as an oxygen scavenger [13] in the buffer to achieve the high refractive index and the oxygen reduced surrounding [281]. The drawback so far was that the enzyme activity of the oxygen scavenging system is strongly reduced by the glycerol in case of GODCAT. A solution for this might be given by the usage of sodium sulfite as a well known antioxidant in food industry. Therefore, it is cheaper in comparison to the established GODCAT and PCD/PCA.

The other important source of fluorescent labels are proteins. With the discovery of the green fluorescent protein (GFP) [17] a new way of observations in living cells and whole organisms is possible. Nowadays a "paint box" with different fluorescent proteins is available. On the one hand there are the fluorescent properties like emission wavelength, photoswitchability or photoconvertibility, and on the other hand the local specificity. In this way it is possible to label proteins of interest, with an additional fluorescent protein, and study aging, turnover, localization or motility. In addition, proteins are available with properties that make them valuable as sensors for protein activity, membrane potentials and analytes [140]. Therefore, dynamic measurement of protein interactions are of particular interest. An powerful application is the combination of super-resolution localization microscopy with fluorescent proteins. Thus, they must be switchable from a dark-state to a fluorescent state or change the emission wavelength with the usage of an external trigger like a specific wavelength (see e.g. table 2.1). The first type is called photoactivat-

able fluorescent proteins and the last type photoswitchable. The following table 2.1 lists some photoconvertible proteins with the conversion wavelength, the absorption and emission maximum and emission wavelength of the pre-converted state, and the wavelengths of the converted state. These few examples show that these fluorescent proteins have quite similar fluorescent properties. Later, mEosFP*thermo* is used for photoactivation localization microscopy (PALM), where there photoactivation is the change from green to red fluorescence conformation. The type of mEosFP used here is derived from the original form presented by Wiedenmann and colleagues in 2004 [74] and has a higher thermostability.

2.2. Approaches to super-resolution microscopy

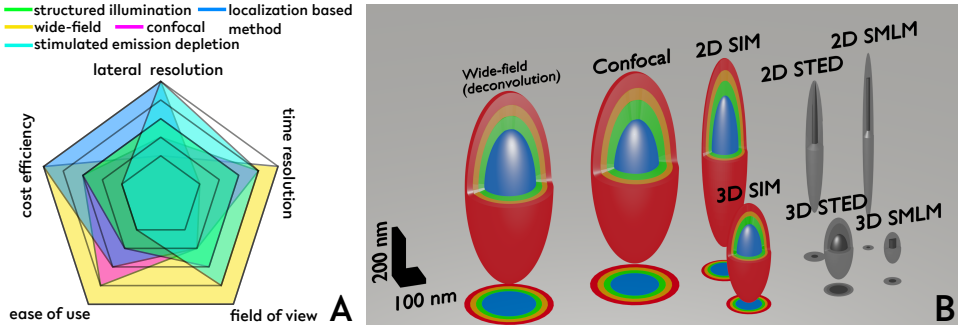

Figure 2.6.: The schematic drawing in **A** shows in a qualitative way the benefits and drawbacks of several basic concepts of fluorescence microscopy. The categorization is based on the review article by Schermelleh et al. [320]. For most of the shown techniques it is necessary to distinguish between the two and three dimensional operational mode. In **B** the schemes of theoretical PSFs for different microscopy techniques are depicted. The color coded PSFs for the widefield, the confocal and the SIM approaches are indicating, that the achievable resolution, which is reflected by the effective PSF, is dependent on the emission wavelength. On the other hand the later mentioned method stimulated emission depletion (STED) depends on the laser intensity in the STED doughnut. A higher intensity leads to a smaller theoretical PSF by depletion of the fluorescence outside the doughnut. For SMLM methods, it depends on the localization accuracy (see chapter 2.3.1) and on the labeling density, which is important to restoring the underlying structural information.

Since the experimentally discovered resolution limit by Ernst Abbe [6] (see equation 2.7) today, there are a number of different methods available to exceed the resolution limit. A first distinction can be made between wide-field and scanning

approaches. Prominent scanning approaches are reversible saturable optical fluorescence transitions (RESOLFT) [79], stimulated emission depletion (STED) [29, 41], airyscan [292] and instant structured illumination microscopy (iSIM) [192]. On the other, hand several wide-field microscopy methods are available to circumvent the diffraction limit, while pursuing different basic approaches with varying benefits and drawbacks (see figure 2.6 **B**). In SMLM the aim is to detect single non overlapping emitter in each acquired frame, where the emitter positions are estimated by e.g. a two dimensional Gaussian fit. The final image, breaking the diffraction limit, consists of all localized molecules represented by their Cartesian coordinates. It is possible to transfer the fluorescent molecules to non-fluorescent "off"-states via resonance energy transfer or fitting chemical condition. The first mechanism can be related to the early approach by Rust et al. [96] and is called stochastical optical reconstruction microscopy (STORM). Later a more universal and *direct* method for conventional fluorescent probes was presented by Heilemann et al. [115] and named *d*STORM, where special chemical buffer conditions are exploited, which is mentioned in section 2.1.5. A different approach is based on the subsequent activation or photoconversion of single fluorescent organic molecules or fluorescent proteins. Therefore, this method is called photoactivated localization microscopy (PALM) [86, 88]. These techniques require a large number of images to localize a sufficient amount of fluorescent molecules to reconstruct the underlying structure. The stochastical optical fluctuation imaging (SOFI) [129] deals with the autocorrelation function of each detector pixel. A comparable method utilizes radial fluctuations to achieve super-resolution images (SRRF) [235].

In addition to the various imaging modalities, the type of fluorescence labeling also plays an important role. Therefore, beside the technical, optical and computational developments there has to be an ongoing improvement of fluorescent probes. Depending on the imaging method different properties of the label can be favorable. The fluctuating emission scheme on different time scales of Qdots is favorable for methods like SOFI. But the application to SMLM methods is more challenging because the fluctuating emission is difficult to control [233, 247] and exhibits a spectral blue shift with time [153, 228]. As long as the labeling density is high enough and the blinking occurs on time scales shorter than the exposure time of the detector, they are a useful label for wide-field structured illumination microscopy (SIM) [46, 78, 113]. Regardless the brightness, photostability and for certain extend controllability of Qdots blinking behaviour, one of the mayor disadvantages is the size and the complex surface chemistry complicates the usability [124]. The label has to be functionalized and later transported to its final destination.

Recently, attempts have been made to set a benchmark for super-resolution microscopy by developing a cell line with modified nuclear pore complexes (nucleoporin Nup96). This protein in the nuclear pore complex is altered in such a way that different specific tags [68, 121] can bind to it or fluorescent proteins are fused

to it. Therefore, it is possible to use these samples as a versatile reference for quantitative super-resolution microscopy [322], since the label efficiency and microscope calibrations can be checked due to the characteristic eightfold symmetry and the height of 49.3 nm [206] between the two rings.

Due to the high relevance in the field of super-resolution microscopy STED and the more advanced MINFLUX [257] method will be described briefly. The later methods for the investigation of polymer particles and biological samples are mainly SMLM methods. To support the results of core-shell microgels, a second super-resolution method is used with structured illumination microscopy (SIM).

2.2.1. Stimulated Emission Depletion

In STED microscopy, the sample is scanned with two laser beams that differ in shape or intensity distribution and wavelength. The first beam excites the fluorophores in a diffraction-limited volume, which in combination with a pinhole would be a standard confocal microscope. For the stimulated emission depletion, a phase mask is introduced into the second laser beam to create an optical vortex. Consecutively after the excitation, the second beam will deplete the fluorescence with the formed vortex. This second beam is therefore termed as STED-beam. In total, fluorescence remains from an area well below the diffraction limit. The same mechanism can also be used with photoswitchable or photoconvertable fluorophores. With respect to the diffraction limited found by Abbe the resolution for STED the reachable resolution d can be termed in a similar manner.

$$d \approx \frac{\lambda}{2\mathrm{NA}\sqrt{1 + \frac{I}{I_{\mathrm{sat}}}}} \tag{2.15}$$

The known formula is extended by the factor $\frac{1}{\sqrt{1+\frac{I}{I_{\mathrm{sat}}}}}$, where I is the maximal focal intensity applied in the STED beam and I_{sat} the intensity, which is necessary to achieve a halved fluorescence emission probability [114]. From equation 2.15 it is possible to see, that the achievable resolution is in theory unlimited because the STED-beam can be narrowed down with increasing laser intensity I. The investigation of living cells is of particular interest for the life sciences. So it is necessary to find the trade-off between resolution and life cell compatibility. Recent studies showed an increased cell mortality after 24 h following STED microscopy [284].

The next evolution step was to combine properties from localization methods with the doughnut shaped beam. To extract the fluorophores position the doughnut beam has to be placed at four equally spaced locations. From the ideal model with the fluorescent molecule in the middle of the STED beam no fluorescence should occur at this middle position. Therefore, the absence of fluorescence signal leads to a high resolution. By narrowing the STED doughnut in theory unlimited

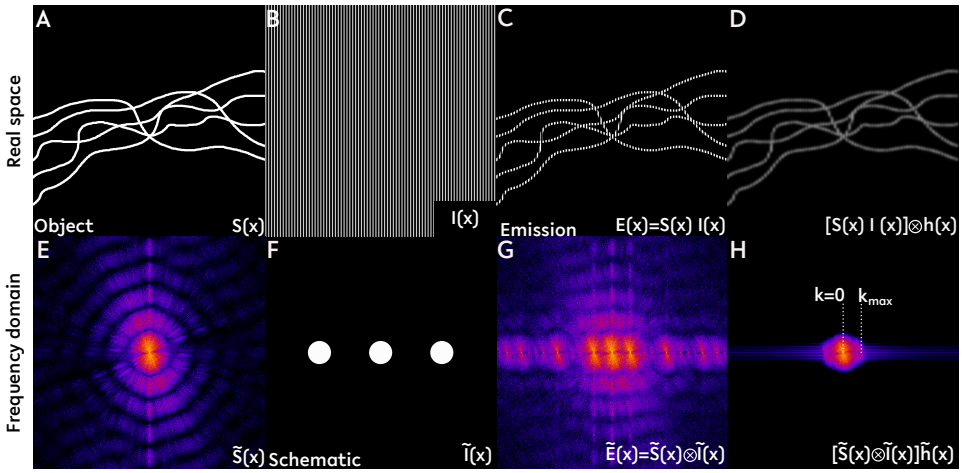

Figure 2.7.: The upper row shows the real space representation of filament-like structures (**A**) under a structured illumination with a sinusoidal intensity distribution (**B**). The resulting image is the product of observed structure and the structured illumination (**C**). An image taken by a microscope has to be convolved with the microscopes specific PSF resulting in **D**. The corresponding Fourier transformations are displayed in the bottom row. The sinusoidal intensity pattern is schematically shown with the three dots representing the delta peaks (**E**) in the frequency domain. In Fourier space, the emission is a convolution with the three delta peaks which can be seen in **G**. Due to the limited passband only a fraction of all frequencies can pass the optical system (**H**). Adapted from [265].

resolution is achievable, due to the fact that there is no fluorescence emission from the fluorescent molecule. Therefore, this technique is named MINFLUX [257] after the minimal photon flux, which is used for a precise localization. In the latest development a dual color 3D MINFLUX setup was presented where nuclear pore complexes (NUP96) and synaptic protein organization was investigated [307].

2.2.2. Structured Illumination Microscopy

There are several methods that can be called structured illumination microscopy (SIM). The brief description covers the proposed SIM method by Mats Gustafsson [46] and Rainer Heintzmann [39]. This method exploits an excitation of the underlying structure with a fine spaced pattern near the diffraction limit. It can be visualized similar to the Moiré-effect that can be seen in daily life, e.g. striped shirts or a micromesh. The interference pattern inside the sample can be gener-

ated with different devices, like optical gratings, spatial light modulators or digital mirror devices. Each device is capable of generating different diffraction orders and introduce the phase shift, which is necessary for SIM. For 2-beam SIM only the beams of the first diffraction order interfere at the objective lens focal plane and generate a sinusoidal intensity pattern. To get a super-resolved image out of this effect, it is necessary to capture images with at least three different angles and three phases. In total only nine images are required for a super-resolved 2D image which enables a resolution improvement up to a factor of approximately two. To generate a 3D-SIM image with axial resolution improvement, the interference pattern creation is more difficult and involves the zero diffraction order, which is blocked in the 2D case. In comparison to the sinusoidal stripe pattern for 2D, the 3D pattern looks like a lattice. The sample has to be moved through the illumination pattern and in comparison to the 2D case three different angles with each five phases have to be acquired. With knowledge of the illumination pattern and the captured image it is possible to compute the underlying image by solving a linear system of equations corresponding to a beat frequency [113, 242]. This procedure can improve the resolution by about two in both the lateral and axial direction. In the following, a more qualitative description of the resolution in 2D linear SIM is given.

For a better understanding of the image formation in SIM it is beneficial to consider the image formation in the Fourier space. By Fourier analysis an image can be decomposed into its sum of waves, which includes a measure of feature size by the spatial frequency, intensity, phase and direction.The complete decomposition is known as image spectrum $\tilde{J}\left(\vec{k}\right)$.

In figure 2.7 the top row shows the real space image of some filament like structures. **A** represents the ground truth with a certain fluorescence density $S(x)$ of this structure. The product of the structure and the illumination pattern with sinusoidal intensity distribution $I(x)$ (figure 2.7 **B**) results in figure 2.7 **C** with the emission $E(x)$. In the last subfigure **D** the limitation of spatial frequencies in a microscope is realized with a Gaussian blur of the emission image to estimate the convolution of the microscopes PSF with the original image. The bottom row of figure 2.7 represents the frequency domain of the real space images, where the Fourier transform of the structure, the illumination pattern and the emission is denoted with $\sim$. Image **F** is displayed in a schematic way, because the stripe pattern will result in three delta speaks at the frequencies $k = \{-k_{max}, 0, k_{max}\}$. In Fourier space the multiplication is a convolution operation, therefore, the calculated frequency spectrum is convolved with the delta peaks resulting in two additional shifted copies of the original spectrum (see figure 2.7 **G**). The shifted copies in the Fourier space are leading to the resolution improvement in SIM. Frequency components outside of the optical transfer function (OTF) support are shifted into the microscopes passband. The trick is, that due to the multiplication with OTF, not

transferred frequencies are accessible for the microscope. This has to be done via SIM reconstruction.

The main aim is therefore to recalculate the overlapping components and put them in the right position in Fourier space. To achieve the correct recalculation it is necessary to gain more information. With this extra information the overdetermined linear system can be solved. For this reason it is necessary to change the phase of illumination pattern at least three times. With shifting the phase in a single direction, the resolution is only enhanced in this specific direction. For an isotropic resolution enhancement at least three different angles are needed. In total nine images are necessary to, solve the linear system and gain an isotropic resolution enhancement.

In comparison to STED microscopy this method is considered as a good choice for live cell applications due to the lower light dose needed for this kind of microscopy method. In other words an efficient use of the photon budget [265] enables a more gentle and longer observation time of e.g. movements of specific compartments within the cell. The possibilities to acquire images beyond the diffraction limit makes this method a promising candidate for investigations in structural analysis of chromatin in mammalian cells [125] or to visualize the structure of human centrosomes in mitosis or interphase [174]. But the main advantage of this method is the combination of imaging beyond the diffraction limit paired with a decent time resolution. In comparison to the mentioned early applications, where the studies were done on fixed samples, Chagin and co-workes used the temporal resolution to visualize the replication foci in mammalian cells [231] or dynamics between the endoplasmatic reticulum (ER) and mitochondrion or the growth and shrinkage of microtubules [280] were investigated.

2.3. Single Molecule Localization Microscopy

In single molecule localization microscopy (SMLM) the capability of detecting single fluorescent emitters is used to bypass the optical diffraction limit. Therefore, this method utilizes photochemistry and photophysics (compare chapter 2.1.5) to keep most of the fluorescent emitter in the so-called "off-state" where no fluorescent emission occurs. Thus, only a small fraction of molecules are subsequently in the fluorescent "on-state" and can be recorded and afterwards localized. Typically, the localization process is done by a software package which uses knowledge of the PSFs shape and size. Often, the position of a single emitter can be determined by a single 2D Gaussian of the form

$$G = A \exp\left(-\left(\frac{(x-x_c)^2}{2\sigma_x^2} + \frac{(y-y_c)^2}{2\sigma_y^2}\right)\right) + B \tag{2.16}$$

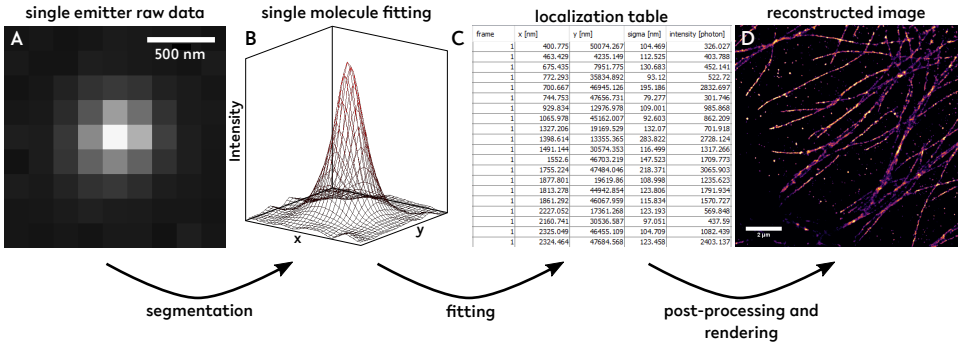

Figure 2.8.: **A** to **D** demonstrates the principle of single molecule localization microscopy. It is important to have distinguishable emitters captured in a single frame (**A**) for a subsequent fitting of the position via e.g. a two-dimensional Gaussian distribution. A typical intensity distribution is shown in **B**. All molecules are afterwards listed in a table **C**, from where a post-processing and the final rendering (**D**) is performed. In **D** (scale bar 2μm) a standard sample of a fixed U2OS cell with a primary-secondary antibody labeled with Alexa Fluor 647 as fluorescent molecule is presented. The target structure of the primary antibody was in this case microtubules,which is than fluorescent labeled by the secondary antibody. To achieve a super-resolved image such as the one in **D**, up to one hundred thousand images and even more single emitters have to be identified and fitted.

with A the amplitude, x_c and y_c the estimated molecule center coordinates, σ_x and σ_y the standard deviation of the Gaussian in lateral directions and the offset B.

A variety of software packages are freely available for SMLM and recently an update of the SMLM software challenge was published in Nature Methods [223, 318]. In this publication the software packages are compared under different image conditions like two-dimensional and three-dimensional reconstruction based on different image modalities. In general the quality of an super-resolved image depends on different factors [309], which are listed in the following as a typical process for generating a super-resolved image based on SMLM:

- Use of correct coverslips. High precision coverslips with a smaller tolerance allow a more reliable and reproducible reconstruction, especially for 3D SMLM. The most objective lenses are optimized for # 1.5 coverslips.
- Choosing the right sample for the application. Scattering media is a major problem in image degradation. Therefore, it is advantageous to have flat and large cells with the structure of interest close to the coverslip surface.
- Proper sample preparation plays an important role in maintaining the nanos-

tructure and can introduce imaging artifacts [226, 237, 289].

- The labeling is of great importance for a good SMLM image. Therefore, the Nyquist-sampling criterion has to be applied to the structure to resolve the underlying structure. Thus, a sufficient dense labeled structure is necessary (compare chapter 2.1.4).

- State-of-the-art hardware is an important tool for achieving the best possible results. Different laser sources allow multi-color measurements, but must provide sufficient output power to push most of the fluorescent labels in a long lived off-state. A laser source with 405 nm or smaller wavelength is useful for returning molecules back to the fluorescent state or photoactive or -convert fluorescent proteins. To collect most of the fluorescent light a high NA objective lens should be used which also allows TIRF imaging. For splitting the excitation light from the fluorescence signal dichroic mirrors with a very flat surface are useful to introduce low wavefront distortions, resulting in low image aberrations. The detector should have a high quantum efficiency over a broad spectrum and low noise to get a high localization precision. Therefore, the projected pixel size should be in the range or smaller than one standard deviation of the PSF [57]

- Creation of a working buffer environment to keep a sufficient number of fluorophores in the off-state. Preferred conditions may vary on the used organic dye. Therefore, it is necessary to find a compromise in multi-color imaging that fulfills the conditions for multiple fluorescent dyes (see chapter 2.1.5).

- Different software packages are available for the localization step. The most suitable software can be chosen based on the imaging condition. The conditions to distinguish are the low density and the high density case. Additionally the method for gaining the three dimensional information might lead to differences. Therefore, depending on the imaging conditions the right software package has to be chosen.

- After receiving the localization table, many options are available for post-processing. The first step usually done is drift correction, which can be carried out by cross-correlation of binned super-resolved images or tracking of fiducial marker. The subsequent filter steps are normally dependent on the total number of detected photons and according to equation 2.18 the localization precision. In addition, filter options regarding the fitting parameters are available like the PSFs standard deviation denoted by σ.

- Image analysis can be done in several ways. For some applications, such as the representation of protein cluster or for visualization of receptors, a

spatial clusters analysis is of main interest, but there are different implementations and approaches [239, 245] to implement the commonly used algorithm DBSCAN [32]. Beside the cluster size the achievable resolution is also of interest. A widely used approach to measure resolution ,based on a more reliable method in SMLM, is Fourier Ring Correlation (FRC) [181, 187]. An other widely used method to estimate the resolution is based on the full width at half maximum of filament-like structures or looking for a drop in localization number between two structures. The last point could be related to the resolution definition by Sparrow [7].

A general workflow, with less details, for creating a super-resolved image is depicted in figure 2.8. The aim of creating a frame with a sparse emitter density can be achieved through different mechanisms. Depending on the application, fluorescent proteins or organic dyes are the choice to get a transition between the different fluorescent states.

2.3.1. Precise and accurate localization of single emitters in SMLM

First, it is necessary to define the differences between precision and accuracy of a localization. For SMLM, accuracy describes the deviation of the mean value of the measured coordinates from the actual position of the localized emitter. Since the actual position of the emitter is usually unknown, it is difficult to measure the localization accuracy. Therefore, it is more convenient to use the localization precision that describes the distribution of localizations around the estimated mean position $\overline{x_p}$ calculated from the contributing localizations $x_{p,i}$. As an example for the one-dimensional case, the localization precision can be calculated from the standard deviation Δx of the mean position $\overline{x_p}$. The localization for the other lateral dimension can be calculated in the same way.

$$\Delta x = \sqrt{\frac{1}{n-1}\sum_{i=1}^{n}(x_{p,i} - \overline{x_p})^2} \tag{2.17}$$

An estimation based on the photon statistics, which follows a Poisson distribution, was first done by Thompson et al. [57] in 2002. With an unlimited photon budget it is possible to achieve an arbitrary precise localization of a single emitter. But with fluorescent proteins and organic fluorescent dyes only a limited number of photons (N) is available. Additionally, the emitter signal is altered by noise originating from the fluorescent emitters themselves and the detector. For the photon shot noise limited case the localization precision, in one dimension, can be given by

$$\Delta x \geq \frac{\sigma}{\sqrt{N}}, \tag{2.18}$$

where σ is the standard deviation of the PSF, approximated by a Gaussian distribution, and N the number of collected photons. It is necessary to take the background noise b also into account, generated by read out noise and dark current noise of the detector, as well as the out-of-focus fluorescence. In addition, the pixel size of the detector and the back-projected pixel size a of the camera also contributes to the achievable precision. Overall, the precision is given by

$$\Delta x = \sqrt{\frac{\sigma + \frac{a^2}{12}}{N} + \frac{8\pi\sigma^4 b^2}{a^2 N^2}}. \tag{2.19}$$

Later in 2010, this equation was redefined by Mortensen et al. [145] to add the specific excess noise of electron multiplying CCD (EMCCD) cameras ($k = 2$) to the model. For other cameras the factor k equals one.

$$\Delta x = \sqrt{k\frac{\sigma^2 + \frac{a^2}{12}}{N}\left(\frac{16}{9} + \frac{8\pi\left(\sigma^2 + \frac{a^2}{12}\right)b^2}{Na^2}\right)} \tag{2.20}$$

The localization precision estimation based on the photon statistics is implemented in the here mainly used ThunderSTORM [197] plugin and will give the localization precision in the final localization table for rendering the reconstructed super-resolved image. In addition to filter purposes, localization precision can be used to render single localizations with a normalized Gaussian distribution, to account for the uncertainty. The localization precision and accuracy can be altered by additional effects like optical aberrations [291], detector inhomogenities [185, 270] and the dipole characteristics of a fluorescent emitter [151, 193]. A general review about precisely and accurate localization is given by Deschout et al. [194].

In SMLM it is common for a single emitter to be fluorescent for more than a single frame. This events can be used to estimate the localization precision by using a nearest neighbor analysis of adjacent frames of the same molecule [196]. In case of no occurring aberrations the true distance between multiple localizations of the same emitter should be equal to zero. Due to the previously mentioned aberrations and noise sources the single molecule distribution with repeated localization can be expressed by

$$\mathrm{PWDD}(|\mathbf{x}_k - \mathbf{x}_l|) = \frac{|\mathbf{x}_k - \mathbf{x}_l|}{2(\Delta x)^2} e^{\frac{-|\mathbf{x}_k - \mathbf{x}_l|^2}{4(\Delta x)^2}}, \tag{2.21}$$

where $|\mathbf{x}_k - \mathbf{x}_l|$ is the distance of two following localizations k and l of the same molecule with $\mathbf{x}$ the lateral coordinate of the pair-wise displacement distribution (PWDD). With this approach an improved statistics is achieved by evaluating the distances between all possible distances coming up with a statistic containing

$n = \sum_k^{n_{loc}-1}$ data points, where n_{loc} is the total number of localizations. By fitting the PWDD with Δx as an optimization parameter, it is possible to achieve the localization precision. In contrast to the localization precision calculation based on the standard deviation for a single molecule (see equation 2.17), the localization precision can be estimated from the base of many molecules. The distribution is altered by the fact that each individual localization will have a different nearest neighbor for the first and the last frame, which makes it necessary to correct for this fact.

$$\begin{aligned}\mathrm{PWDD}(|\mathbf{x}_k - \mathbf{x}_l|)_{corr} =& A_1 \frac{|\mathbf{x}_k - \mathbf{x}_l|}{2(\Delta x)^2} e^{\frac{-|\mathbf{x}_k - \mathbf{x}_l|^2}{4(\Delta x)^2}} \\ &+ A_2 \frac{1}{\sqrt{2\pi\omega^2}} e^{\frac{-(|\mathbf{x}_k - \mathbf{x}_l| - x_c)^2}{2\omega^2}} \\ &+ A_3 |\mathbf{x}_k - \mathbf{x}_l| \end{aligned} \tag{2.22}$$

The first correction term considers localizations from a different fluorescent molecule within a diffraction limited area, following a Gaussian distribution, and the second term for false nearest neighbor calculation on longer spatial distances. For fitting the right distribution the additional free fitting parameters of the amplitudes A_1 to A_3 and the Gaussian standard deviation ω centered over x_c are introduced.

2.3.2. Methods for resolution estimation in SMLM

The limited Rayleigh resolution shown in chapter 2.1.4 is not applicable for super-resolution techniques. Therefore, it is necessary to find other more suitable approaches to define the resolution in super-resolution fluorescence microscopy, in particular in SMLM. A very easy and frequently used method is the Sparrow resolution definition [7], which states that two lines with equal intensities can be resolved in the case that the center between the lines shows a local minimum. If this is the case, the resolution is equal to the distance of the two lines. But only a few samples are showing line-like structures. Another easy-to-use approach is to use a line profile orthogonal to the structure of interest used by Helge Ewers and co-workers in the investigation of DNA intercalating dyes [159], amyloid fibrils [189] and nuclear pore proteins [204]. Due to the possibility to account for the localization precision Δx via a Gaussian rendering, the resolution can also be acquired and estimated by the FWHM of the structure. Thus, the resolution can be calculated directly from the localization precision.

$$\mathrm{FWHM} = 2\sqrt{2\ln 2}\Delta x \tag{2.23}$$

A major disadvantage of this method is that the localization density is not considered and the estimated resolution is only valid for this small region of interest. In

order to take into account the labeling density and thus, the Nyquist criterion, more sophisticated calculations have to be done. The research group of Eric Betzig [236] expressed the overall resolution (OR), which can approximated by the FWHM of a structure, as shown before, and the necessary density of molecules to sample the underlying structure. The resulting expression for the OR is

$$\mathrm{OR} = \sqrt{(\mathrm{FWHM})^2 + \left(\left(\frac{2}{T_{min}}\right)^D\right)^2}, \tag{2.24}$$

in which the last part accounts for the molecular density of the fluorescent label ρ. Here it is assumed that each molecule is localized once. Depending on the dimension of the data D takes the value one to three and T_{min} is the shortest spatial distance to resolve. Even more sophisticated and qualitative methods to estimate the resolution in fluorescence microscopy are the Fourier ring correlation (FRC)[181, 187] and a recently published method for decorrelation analysis, that has the advantage to work without additional parameter [304]. The idea of FRC is to compare two independent images of the same structure. Therefore, the independent images are compared based on consistent spatial frequencies between the two images. In SMLM it is possible to generate two independent images from the same data set for example by dividing the localizations in acquired at even and odd frames with rendering the two data sets subsequently to achieve the images $f_1(\vec{r})$ and $f_2(\vec{r})$ for the FRC. With other super-resolution fluorescence microscopy methods it is necessary to collect the same image twice, with the disadvantage that photobleaching or movement of the sample, e.g. imaging of living cells, occurs. Consequence would be a reduced resolution calculated by the FRC. With the subsequent Fourier transform of the images $\widehat{f}_1(\vec{q})$ and $\widehat{f}_2(\vec{q})$ and the correlation of pixels corresponding to rings in the Fourier domain with identical spatial frequencies the FRC is calculated. $q = |\vec{q}|$ corresponds to the magnitude of the wave vector $\vec{q}$ and the FRC results in

$$\mathrm{FRC}(q) = \frac{\sum_{\vec{q}\in\mathrm{circle}} \widehat{f}_1(\vec{q})\widehat{f}_2(\vec{q})^\star}{\sqrt{\sum_{\vec{q}\in\mathrm{circle}} |\widehat{f}_1(\vec{q})|^2}\sqrt{\sum_{\vec{q}\in\mathrm{circle}} |\widehat{f}_2(\vec{q})|^2}}. \tag{2.25}$$

For low spatial frequencies the correlation gives a value close to unity and decreases to zero at high spatial frequencies where the noise dominates the image and does not show a correlation. A fixed correlation threshold of $\frac{1}{7}$ for the resolution limit can be taken from cryo-scanning electron microscopy. A different approach by Banterle et al. [181] is the calculation of a 2σ curve defined as

$$\mathrm{F}_{2\sigma}(R) = \frac{2\sqrt{2}}{\sqrt{N_p(R)}}, \tag{2.26}$$

where the resolution limit is defined as the point where the calculated FRC crosses the 2σ curve. Here is N_p the number of pixel within a given ring with constant spatial frequencies. A recent method for resolution estimation is published by Descloux et al. [304]. The advantage over FRC is the dependence on a single image, which makes it suitable for methods which rely on correlation of subsequent image to form a super-resolved image, e.g. (SOFI) or estimation of resolution with living samples, where temporal resolution is important. But both methods have in common that they operate in Fourier space. The first step is to suppress high frequency artifacts by an edge apodization. Afterwards a normalized Fourier transform $\widehat{f}_n(\vec{q})$ of the image is calculated by

$$\widehat{f}_n(\vec{q}) = \frac{\widehat{f}(\vec{q})}{|\widehat{f}(\vec{q})|}. \tag{2.27}$$

The input image $\widehat{f}(\vec{q})$ and the normalized version $\widehat{f}_n(\vec{q})$ are cross-correlated in Fourier space by a Pearson correlation. The Pearson correlation is a measure for a linear correlation between two variables and has a value between -1 and 1, where -1 is a total negative linear correlation and 1 a total positive correlation, wheres no linear correlation is observed for 0. However, this does not mean that there is no correlation. In a second step the Pearson correlation is repeated, but in addition to the normalization, the image is low pass filtered by a circular Fourier mask $M(k;r)$ with a radius $r \in [0,1]$. By repeating the correlation calculation between the input image and the normalized and low pass filtered image, the cross-correlation coefficients $d(r)$ are computed.

$$d(r) = \frac{\int \mathrm{Re}\{\widehat{f}(\vec{q})\widehat{f}_n^{\star}(\vec{q})M(\vec{q};r)\}dq_x dq_y}{\sqrt{\int |\widehat{f}(\vec{q})|^2 dq_x dq_y \int |\widehat{f}_n(\vec{q})M(\vec{q};r)|^2 dq_x dq_y}} \tag{2.28}$$

The idea behind this method is that high frequencies are dominated by white noise and by cutting off those high frequencies with a mask with $r < 1$, the noise is gradually removed and the signal preserved. Under the assumption of an image containing only noise, the correlation decreases linearly as a function of the radius r. For an image with a signal, the cross-correlation coefficients will have a local maximum with an amplitude A_0. This can be interpreted as the spatial frequency at which the best noise suppression and best signal preservation are obtained. Beyond the local maximum with further reduction of the mask radius signal is rejected until it drops to zero for $r = 0$. The cut-off frequency q_c of the image can be calculated from a family of curves after high pass filtering (from weak to strong filtering via a Gaussian filter) of the input image $\widehat{f}$. Each filtering step, in total N_G steps, will give a pair $([r_i, A_i])$ of the peak position r_i and the corresponding amplitude A_i. The estimate for the cut-off frequency q_c is than

$$q_c = \max[r_0, ..., r_{N_G}]. \tag{2.29}$$

The resolution is afterwards calculated over

$$\text{Resolution} = \frac{2 \cdot \text{Pixel size}}{q_c}. \tag{2.30}$$

Compared to FRC, in which the resolution is estimated by a threshold value, the decorrelation method thus estimates the highest frequency transmitted by the system via the local maximum of the decorrelation function.

2.3.3. 3D single molecule localization microscopy

In addition to the possibility to precisely localize molecules in lateral dimensions, there are ways to extend SMLM to the axial dimension. This can be achieved with different methods. First, two methods are briefly mentioned, which are working without modifications on the recorded PSF. In a publication by Franke et al. [263] the axial position is estimated based on a photometric method, more precisely a temporal and radial-aperture-based intensity estimation (TRABI). They claim that with this approach it is possible to recalculate a precise axial position based on the counted photons in different positions of the emission pattern of a single molecule. This method allows to convert existing two-dimensional single molecule localization data into a three-dimensional data set. Another approach is the use of two cameras [123, 275] or dividing of a camera chip [119] in two parts acquiring the signal of the same emitter from two different focal planes. This approach can be easily extended to multi-color imaging by spectral demixing [227].

The other group of methods uses optical elements to engineer a PSF where the axial position is encoded in the shape and the position. In SMLM an encoding can be achieved by inserting a cylindrical lens to introduce astigmatism to the PSF [117] or create a so called double helix PSF by inserting a phase mask, which can also be realized with a reflective phase-only spatial light modulator(SLM) placed in the Fourier plane [136]. The double helix PSF has the axial position encoded in the angle between the horizontal and connection line between the two lobes created by a phase mask. Therefore, the molecule is localized between the two lobes.

Recently, adaptive optics has become more and more important for super-resolution fluorescence microscopy. The whole topic deals with the possibility to correct a deformed wavefront [12, 208, 266] described by Zernike polynomials of different order. This can be achieved e.g. with a deformable mirror [59]. In addition to wavefront correction, it is also possible to use Zernike polynomials to engineer a PSF for 3D SMLM [274]. The main advantage over PSF shaping with a cylindrical lens is the higher axial range [224] in which the generated pattern can be detected due to the higher intensity at certain points of the PSF compared to an astigmatically shaped PSF. However, the astigmatism introduced through a cylindrical lens has the advantage of simplicity of implementation in a 2D SMLM microscope. This

method is used to generate three-dimensional localizations of individual molecules in this thesis.

An example for a calibration with an astigmatic PSF is shown in figure 2.9 **A** and **B**. This calibration is integrated into the fitting procedure, where tubulin is reconstructed and the generated height information is color coded (see figure 2.9 **C**). For 3D data the so called Fourier shell correlation can be applied to calculate an estimate for the achieved resolution in 3D. Unfortunately, there is currently no easy-to-use software implementation, e.g. for ImageJ, available. Therefore, the FRC is used to get an estimate for the lateral resolution, in this case 32.4 nm (figure 2.9 **D**). The 2D Gaussian fit described above (see equation 2.16) must be slightly modified to take into account the introduced astigmatism while defocusing. The standard deviations of the two Gaussians in lateral direction (σ_x and σ_y) are replaced by the width w of the PSF in the two lateral directions indicated by the indices x and y. To readout the axial information from the width of the PSF, a previous calibration step is required (see figure 2.9 **A**). This step is typically performed with fluorescent beads with a size below the diffraction limit, whilst the focus is mechanically moved through the sample by a piezo stage. Knowing the step width between the individual images, the width w of the PSF can be expressed by a function depending on the axial position z [117].

$$w_{x,y}(z) = w_0 \sqrt{1 + \left(\frac{z-c}{d}\right)^2 + A\left(\frac{z-c}{d}\right)^3 + B\left(\frac{z-c}{d}\right)^4} \tag{2.31}$$

Here, w_0 is the PSF width at the focal plane, c is an offset for the width in the lateral directions, d is the focal depth of the microscope and A and B are coefficients to correct for aberrations of the optical system. To determine the focal plane, the width of the PSF in both directions is plotted against the axial position. In focus of the objective lens the PSF will appear symmetric, which is indicated by the intersection. To determine the z-position of a single emitter during the localization process, the distance D between the calibration curves PSF width and the measured one is minimized.

$$D = \sqrt{\left(w_x^{1/2} - w_{x,calib}^{1/2}\right)^2 + \left(w_y^{1/2} - w_{y,calib}^{1/2}\right)^2} \tag{2.32}$$

An example for a calibration is shown in figure 2.9 **B**. The generated calibration curve according to equation 2.31, where black is the width of the PSF along the x-direction and orange along the y-direction, shows the limitation of this method. It can be seen that the calibration becomes inaccurate at distances further away from the focal plane due to the lower signal-to-background ratio and possible aberrations in the optical detection path.

Therefore, more sophisticated algorithms are necessary to account, in a better way, for aberrations in the optical system. In addition to the widely used Im-

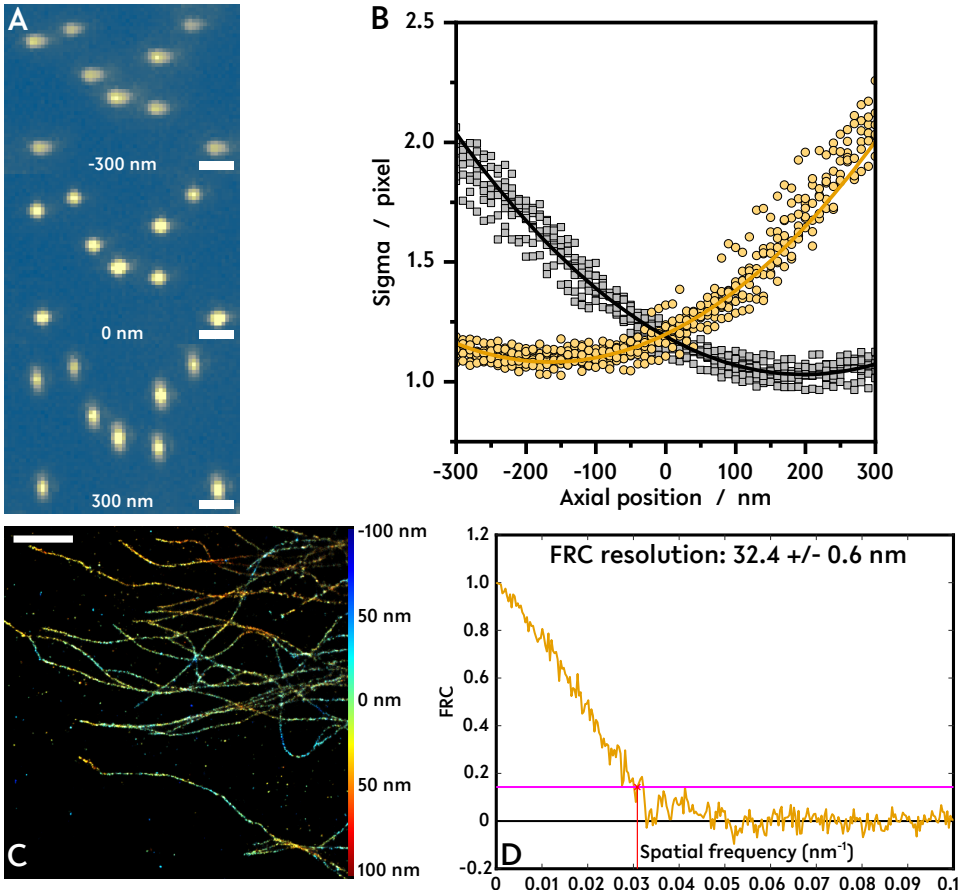

Figure 2.9.: From **A** to **D** the additional steps typical for a 3D SMLM image are shown. Adding a cylindrical lens introduces astigmatism in the detection path. The height information is therefore encoded in the PSFs shape during defocusing (**A**, scale bar 500 nm). The image stack must be evaluated based on a defocusing algorithm in which the two parabolic curves intersect at the height of 0 nm (**B**). In addition to the lateral localization the molecule can be localized with respect to the focus of the objective lens. A reconstructed 3D SMLM image of tubulin is shown in **C** (scale bar 2 μm). The lateral resolution via FRC gives an estimation of 32.4 nm (**D**.)

ageJ[173] plugin ThunderSTORM [197] and a modified version [286], a different approach by Jonas Ries is available. This method works without an underlying model, like the defocus algorithm. Instead an integrated cspline 3D fit algorithm [285] is used. Spline functions are piecewise polynomials with the property to be continuous at the connection points. Here the "c" in cspline stands for cubic and determines the degree of the polynomial. The number of calculated coefficients N_{coef} for the spline depends on the degree d, and the dimension dim, where the number of coefficients is defined as $N_{\text{coef}} = (d+1)^{dim}$. Therefore, the cspline requires 64 coefficients for each voxel of the acquired data set. According to Babock et al. [256] a voxel i, j, k is described as

$$f_{i,j,k}(x,y,z) = \sum_{m=0}^{3}\sum_{n=0}^{3}\sum_{p=0}^{3} a_{i,j,k,m,n,p}\left(\frac{x-x_i}{\Delta x}\right)^m\left(\frac{y-y_j}{\Delta y}\right)^n\left(\frac{z-z_k}{\Delta z}\right)^p. \quad (2.33)$$

Here, Δx and Δy are the projected pixel size of the microscope and Δz is step size of the focal shift during the calibration. As mentioned, the calibration is done with fluorescent beads. The parameters x_i, y_j and z_k are the start positions of the voxel respectively the lateral and axial directions. Afterwards the cspline calculation is performed with the averaged image stack of fluorescent beads. This method can also handle the above described axial position estimation via the Gaussian fit along both lateral directions (see equation 2.31), but the model is estimated by a polynomial approximation.

2.4. Microgels: polymer based colloids with smart properties

A special and widespread topic in natural science is the family of condensed soft matter. The common property of soft matter is the presence of a large response function [83]. Surprisingly also a brick can be described as soft matter and beyond that as smart material. Due to its properties, it breaks into pieces when falling from a certain height, which would be the response to the applied force. In this work different stimulable polymers are examined, which are called microgels, when nanoscopic or microscopic particles are formed. It is possible to achieve macroscopic polymers, which are calles macrogels. A classification, which requirements particles, which are called microgels, must fulfill, is done afterwards. Microgels are special because they can show different characteristics from macromolecules (DNA or proteins), colloids, especially in the collapsed state, and micellar aggregates based on surfactants, showing an amphiphile behavior[271]. The variety of properties allows a few applications and makes them promising candidates for drug delivery [122, 306, 325], smart surface coatings [147, 251] or nanocatalysis [298]. The

following subsection gives a brief and general introduction to the characterization and structure of microgels.

2.4.1. What are microgels?

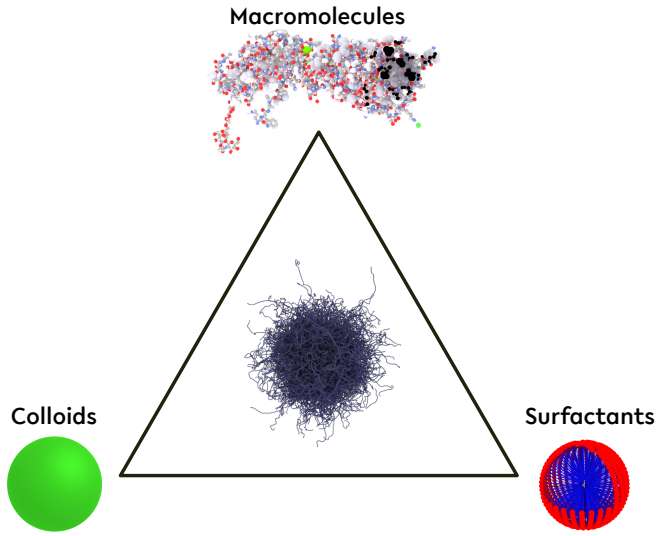

Figure 2.10.: There is a large variety in the world of colloids. In the middle of the triangle is the microgel, which combines the basic properties of colloids, macromolecules and surfacants. Collapsed microgels mainly show properties of colloids, although they still contain solvents. In contrast, microgels in the swollen state have a soft and "fuzzy" surface with dangling hair-like polymer chains. The colloid and macromolecule characteristics can be tuned by the amount of cross-linker used during the synthesis. In addition, they can have surface-active properties, which is here termed surfactants.

The following definition of microgels is based on the book "Microgel Suspensions" edited by Alberto Fernandez-Nieves, Hans Wyss, Johann Mattson and David A. Weitz [158]. In their view, microgels are a colloidal suspension of gel particles associated with four implicit criteria:

- particle size, typically colloidal particles, between 10 nm and 1000 nm, therefore the name "nanogels" would also work
- dispersed in a solvent
- swollen by the solvent

- stable structure / network based on covalent or physical forces with the ability to form cluster

The nature is often a good blue print for new bioinspired artificial systems [264] or even for new algorithms [148]. So why not mimic properties from naturally occurring systems of different sizes in which microgels of different size can be found? For a full understanding of the microgels' behavior, response and how to tune them for specific applications, the interplay between different disciplines such as biology, chemistry and physics is necessary. In this thesis, the morphology of stimuli responsive microgels is investigated with super-resolution fluorescence microscopy, more precise with SMLM. The established methods from colloid science to characterize microgels, such as photon correlation spectroscopy, scattering approaches with neutrons [55, 73] or x-ray radiation [202], or scanning electron microscopy [269], are in their applications limited or time consuming in preparation. As a system that can be classified as soft matter, it reacts at least to a stimulus such as mechanical stress, changes in the chemical environment or temperature change. This is due to the large surface to volume fraction, microgels responding quickly to these stimuli. Another useful property is the reversible response of the microgel for some systems [246] and the possibility to switch them to the desired conformation via the specific stimulus.

Microgel synthesis

In the following the three typically used methods to create microgels are briefly presented. The methods will have their advantages and disadvantages. The most common approach is the formation of microgels via homogeneous nucleation, starting with an initially homogeneous solution of vinyl monomers followed by cross-linking the chain-like monomers. In another process, the starting point is a polymer solution, which is then emulsified in small droplets and then chemically cross-linked. The last method uses macrogels as basis, whereby the microgel is the result of a grinding step. Drawback here is an irregular shape and size. In this thesis, the homogeneous nucleation method is used to produce various microgel systems. Therefore, it is necessary to distinguish between the later investigated microgels. At first microgels synthesized from a single monomer with varying cross-linker content are investigated and a new method to estimate the microgels morphology is introduced. This method can be extended to core-shell microgels, where the seed particle is made of an different monomer compared to the shell, which is synthesized around the seed particle in a second synthesis step.

In the scope of this thesis, surfactant-free precipitation polymerization is used. For this type of synthesis, the monomer of interest and the initiator are both soluble and form a homogeneous system at the beginning of the synthesis. During the synthesis, the polymerized particle becomes insoluble and precipitates. The result

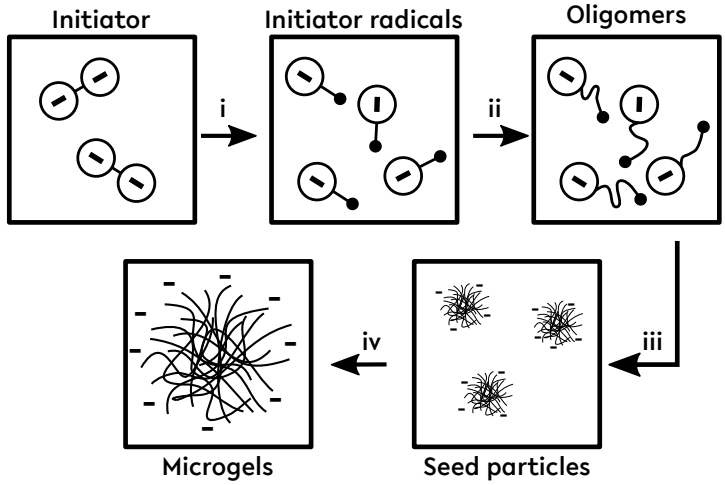

Figure 2.11.: The schematic drawing shows the formation of seed particles, relevant for growing the final microgel. In addition, the total number of seed particles can be tuned and therefore, the final microgel size. In step **i**, the initiator decays into its radical ionic form. These molecules are accessible for the monomer and the cross-linker in solution. Oligomers are formed by crosslinking up to a certain critical polymer length (**ii**). Approaching this length the oligomer collapses and forms seed particles with increasing surface charge density. A stabilization of the former unstable particle is obtained by the electrostatic retraction (**iii**). In the last step the seed particles can grow further by continuous polymerization or adsorption of seed particles. Therefore, the number of seed particles is a parameter to tune the final particle size. At the final size the microgel is fully collapsed and precipitates.

of the synthesis depends on the synthesis temperature. While the temperature is below the lower critical solution temperature (LCST), a macroscopic polymer gel is formed. In case that the temperature is higher than the LCST small particles are formed by the formation of seed particles and precipitation.

Variation of the synthesis components and conditions lead to a different stimuli response and other properties of the microgel or macrogel. Some parameters that can be used for tuning are: the chosen solvent, the concentration of monomers, the ratio between monomer and cross-linker agent, the temperature, the initiator concentration or pH.

Here, the investigated microgels are made in a precipitation polymerization. The brief description is based on the review article by Thickett et al. [108] and the thesis by Bastian Wedel [225]. At the starting point of the synthesis the cross-linker and the monomer are mixed together with the solvent. To initiate the reaction to

the initiator has to be added the solution and oxygen has to be removed because otherwise the formed radicals would react with the contained oxygen and are not accessible to form oligomers. The required reaction temperature depends on the initiator and the monomer because the temperature has to be higher than the LCST of the monomer. Due to the high temperature the initiator decays into radicals (figure 2.11 **i**). The radicals reacting with the monomer to oligomers (figure 2.11 **ii**). After reaching a certain chain length the oligomers become insoluble, collapse and form aggregates, because the temperature is above the LCST (figure 2.11 **iii**). Simultaneously to the growth of seed particles, the surface charge of the particle increases up to an amount where the particle is stabilized and no further aggregation takes place. The particle size grows further by ad- and absorption of oligomers, seed particles and polymerization. In between the cross-linking occurs continuously and seed particles and oligomers can be connected to each other. The end of the polymerization is reached when all monomers are used for the microgel synthesis or no radicals are available for a further reaction.

In general the synthesis can be divided into four phases:

Stage 1 The initiator molecule decays into radicals (figure 2.11 **i**). Subsequent oligomers (figure 2.11 **ii**) and seed particles (figure 2.11 **iii**) are formed .

Stage 2 Aggregation of primary particles from seed particles.

Stage 3 Primary particles growing further by adsorption of more seed particles. Additionally the radical polymer reaction continuous and ad- and adsorb oligomers are cross-linked to the primary particle (figure 2.11 **iv**).

Stage 4 End of the growing phase.

Thermoresponsive polymers

The properties of a microgel can be described hardly if one only considers the properties of a three-dimensional polymer network or a two-dimensional polymer chain. A single polymer chain carries out a coil-to-globule transition for the polymer length-specific critical temperature. For a single polymer chain, the lower critical solution (LCST) temperature describes the solubility in the solvent. For a microgel, the term volume phase transition temperature is more conventional (VPTT), but in general the result of local LCST behaviour. To achieve a microgel in precipitation polymerization the synthesis is done above the LCST and the final microgel appears in the collapsed state. The final collapse is restricted by the cross-linking points in the network. At temperatures above the LCST water is a poor solvent and upon decreasing temperature under the LCST the polymer gets hydrophilic and wants to interact advantageously with the solvent. For this purpose, water is incorporated and the polymer network swells. Due to the high length dispersion of single polymer

chains in a microgel different parts experience a collapse and therefore a continuous volume phase transition can be observed for microgels with a higher cross-linking density in comparison to low cross-linked microgels with a discontinuous volume phase transition.

2.4.2. Characterization methods for spherical polymer particles

Atomic force microscopy

This section is based on the review paper by Jalili et al. [67] and will give a brief introduction to the method of atomic force microscopy (AFM). The principle of AFM is the measurement of attraction and repulsion forces between a very thin tip down to 5 nm in size mounted on a flat spring. This combination of flat spring and tip is called cantilever. By using the flat spring as a mirror for a laser, the displacement of the laser spot, due to the deformation of the spring, according to Hooke's law by the forces between the tip and individual atoms, can be measured very precisely with a position-sensitive photodiode. Different operating modes are available, namely the contact mode, the tapping mode and the non-contact mode.

In contact mode the tip is moved over the sample and the change of the surface height or the force between tip and surface is measured directly by the movement of the laser spot. This mode is called the constant height mode, where the cantilevers flat spring is deformed directly by a change in surface height. A limiting factor for this mode is the roughness of the sample. The flat spring has only a certain working range, which can be exceeded by too rough surfaces. The opposite way to operate an AFM in contact mode is to set the measured force to a specific value which has to be maintained by moving the cantilever with a piezoelement. The height change by the piezoelement can be directly taken as a measure of the sample height. The other extreme is to operate an AFM in non contact mode. Here, the tip is placed very close to the surface, typically 5 to 15 nm above, to detect the weak van der Waals forces, which can be detected in this range. To measure these forces, in the range of about 10 to 12 pN, the cantilever oscillates with its resonance frequency or slightly off-resonance. It is possible to measure the forces by either the amplitude, phase or frequency of the oscillating cantilever. The advantage of the non contact mode is the flexibility to image soft and elastic samples. Typically, these kind of samples are deformed by the tip in contact mode.

A combination of contact and non contact mode is the tapping mode. In this mode, the cantilever oscillates like for the non contact mode at or close to its resonance frequency. Amplitude and frequency are kept constant as long as no interaction with the sample or the surface occurs. During the scanning of the surface regularly the tip touches the surface, which leads to a loss of energy and a decrease in amplitude. When a bump approaches the tip, the space between tip and surface becomes smaller and the ability to oscillate decreases. On the other

hand in the case of a dip in the structure, the space to oscillate increases and approaches the amplitude for a free oscillation. The whole system is driven by a feedback loop of the acquired optical signal, which feeds a piezoelement to maintain the oscillation amplitude, comparable to the constant force method in the contact mode. So the change of the signal in the feedback loop is a function of the tip's lateral position.

Both the optical microscopy and the atomic force microscopy have to deal with the problem that the generated image is convoluted. Where in optical microscopy the convolution of a point emitter is set by the optical system in AFM the measured topography is a convolution of the tip geometry and the sample surface.

Photon correlation spectroscopy

The following description for photon correlation spectroscopy (PCS) is based on the chapter 10.10 Characterization of Products from the book Monodispersed particles [53] released by Elsevier. One method to measure the size of microgels in a solvent is PCS. The scattering and diffracting microgels are moving randomly according to Brownian motion in a solvent. Therefore, the laser beam will have a certain frequency distribution due to the Doppler shift on the microgels in the solvent. The frequency distribution is typically described by the half width at half maximum (HWHM) of the peak amplitude A_0. A different representation of the frequency distribution is the power spectrum of the scattered beam. In a power spectrum, the amplitude is transformed into a function depending on $2|f - f_0|$, where f_0 is the initial laser frequency. The shape of the power spectrum can be described by a Lorentz distribution. If the amplitude of the signal is measured over a longer period of time, a fluctuating signal appears. From this time trace an average amplitude and the relative amplitudes at time points t and $t + \tau$ can be calculated. The auto-correlation function $C(t)$ is defined as

$$C(\tau) = \langle A(0)A(\tau)\rangle = \lim_{T\to\infty}\frac{1}{T}\int_0^T A(t)A(t+\tau)dt. \tag{2.34}$$

Under the assumption that microgels are monodisperse, the auto-correlation $C(\tau)$ can be simplified by

$$C(\tau) = C(0)\exp(-2\,\mathrm{HWHM}\,\tau). \tag{2.35}$$

Furthermore, the HWHM contains information about the hydrodynamic radius R_H by the product of transverse diffusivity also known as the translational diffusion coefficient

$$D_T = \frac{k_B T}{6\pi\eta R_H} \tag{2.36}$$

expressed by the Stokes-Einstein relation and the magnitude of the scattering vector $p = \frac{4\pi n_0}{\lambda_0} \sin \frac{\theta}{2}$.

$$\text{HWHM} = D_T p^2 \tag{2.37}$$

The Stokes-Einstein relation depends on the Boltzmann constant k_B, the temperature T, the solvents viscosity η and the hydrodynamic radius R_H. On the other hand, the scattering vector depends only on the setup parameters, initial laser wavelength λ_0, the solvents refractive index n_0 and the scattering angle θ.

Fluorescence correlation spectroscopy

Compared to PCS the fluorescence correlation spectroscopy (FCS) uses the fluctuation of fluorescent signals in a diffraction-limited confocal volume to determine the translational diffusion coefficient D_T in equation 2.36. In the perspective of this thesis, this method is used to estimate and verify the interaction of the "free" diffusing dye molecules and the network formed by polymer in combination with a cross-linker. To achieve a measure for the diffusion coefficient certain circumstances have to be fulfilled. The detection and excitation volume has to be sufficient small, the confocal volume typically is in the range of 0.1 femtoliter, and the number of molecules within the detection volume has to be sufficient small (a single molecule up to very few molecules) at every time point during the measurement. Due to the limited number of molecules in the small volume an intensity fluctuation based on the diffusion in or out of the detection volume occurs. Therefore, this fluctuating signal can be correlated with a time-shifted replica of itself to calculate an auto-correlation function G of the intensity $I(t)$ or its deviation $\delta I(t) = I(t) - \langle I(t) \rangle$.

$$G(\tau) = \frac{\langle \delta I(t) \cdot \delta I(t+\tau) \rangle}{\langle I(t) \rangle^2} = \frac{\langle I(t) \cdot I(t+\tau) \rangle}{\langle I(t) \rangle^2} - 1 \tag{2.38}$$

Here τ is the lag time and $I(t)$ is the fluorescence intensity at any time t. The triangular brackets are standing for averaging over all time values of t. To calculate the auto-correlation, setup parameters have to be taken in account like the confocal volume, specified by the the radial and axial diameter of the confocal spot (w_x, w_y and w_z). In addition to the diffusion time τ_D, the auto-correlation provides information about the number of fluorescent molecules with in the confocal spot.

$$G(\tau) = \frac{1}{N} \left(1 + \frac{\tau}{\tau_D}\right)^{-1} \left(1 + \left(\frac{w_{xy}}{w_z}\right)^2 \frac{\tau}{\tau_D}\right)^{-\frac{1}{2}} \tag{2.39}$$

The correlation consists basically of two terms, where the square root term accounts for the ellipsoid shape of the confocal volume. Taking the microscopes

parameters into account, the diffusion coefficient D can be calculated based on the radial dimension of the confocal volume and the diffusion time τ_D.

$$D = \frac{w_{xy}^2}{4\tau_D} \tag{2.40}$$

If one considers that two photons are detected at the time $t = 0$ and the other one after a lag time τ, it is likely that these photons have been emitted by two different fluorescent molecules or are only background contribution. Therefore, they have no physical correlation and together they form a background contributing to the auto-correlation $G(\tau)$ as a constant offset. The other possibility is that a single fluorescent molecule is localized in the middle of the detection volume and emits photons at subsequent time points. Consequently, the signal will be highly correlated because the emitter is the same molecule. When this emitting molecule starts to diffuse out of the volume, the correlation will decrease due to the decreased measured intensity with time, until the molecule completely diffuses out of the detection volume and the correlation will be zero. The decrease in correlation is directly proportional to the diffusion speed of the molecule through the detection volume.

3. Super-Resolution Optical Microscopy resolves Network Morphology of Smart Colloidal Microgels

Major parts of this chapter are published as a peer reviewed article.
Stephan Bergmann[†], Oliver Wrede[†], Thomas Huser and Thomas Hellweg. Super-resolution optical microscopy resolves network morphology of smart colloidal microgels. Physical Chemistry Chemical Physics 20, 5074-5083 (2018) ([†]equal contribution)

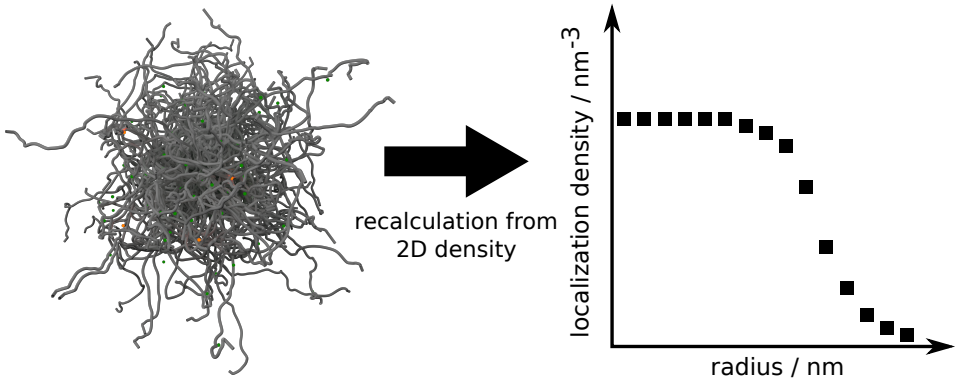

Schematically represented microgel with dye molecules within the polymer network. A small part is fluorescent (orange) and a larger part is in the "off" state (green). By assuming a sphere, a 3D localization density can be recalculated from the projected 2D localization density.

Summary

A new method to resolve the network morphology of colloidal particles in an aqueous environment via super-resolution microscopy is presented in this chapter. By localization of freely diffusing fluorophores inside the particle network it is possible to resolve the three dimensional structure of one species of colloidal particles (thermoresponsive microgels) without altering their chemical composition through copolymerization with fluorescent monomers. The approach utilizes the interaction of the fluorescent dye rhodamine 6G with the polymer network to achieve an indirect labeling. A 3D structure can be calculated from the 2D images and it is possible to compare the structure to previously published models for the microgel morphology, e.g. the fuzzy sphere model. To describe the differences in the data an extension of this model is suggested. The method enables the tailor-made fabrication of colloidal particles which are used in various applications, such as paints or cosmetics, and are promising candidates for drug delivery, smart surface coatings, and nanocatalysis. The precise knowledge of the particle morphology allows an understanding of the underlying structure-property relationships for various colloidal systems.

3.1. Introduction

Smart microgels are able to respond to external stimuli like pH [69, 107, 146, 163], ionic strength [120, 141], temperature[171] or external magnetic [171, 207] and electric fields [211] with a change in e. g. size or orientation. Therefore, these colloidal materials are interesting for a wide variety of applications, i. e. as smart surface coatings [251], carriers for catalysts [75, 143], or as sensors [70, 209, 219, 267, 273]. Microgels are colloidal particles with diameters in the range from 100 nm up to several microns. Internally, they are gels and up to 1 μm in diameter they are made by precipitation polymerization of a (thermo-)responsive monomer and a cross-linker [49, 81, 199, 271]. The most widely studied system is based on the monomer *N*-isopropylacrylamide (NIPAM), often cross-linked with *N,N'*-methylenbisacrylamide (BIS), which shows a reversible volume phase transition at a specific temperature (volume phase transition temperature, VPTT, 32 °C). From an experimental point of view, mainly scattering techniques were used to study the network structure inside the microgels [37, 38, 51, 55, 64, 71].

These experiments indicate a complex morphology for the internal structure, which is due to the higher polymerization kinetics of BIS versus NIPAM. In a free radical precipitation polymerization the resulting particles exhibit a rather dense, highly cross-linked core and a less cross-linked soft shell decorated with dangling polymer chains [55, 99, 133]. Several groups have, therefore, worked on the determination and description of the cross-linker distribution. The so-called fuzzy-

sphere model by Richtering and co-workers is a widely used empirical model [73]. Another description is based on a Matryoshka approach [141]. Recently, Boon and Schurtenberger have published an alternative approach [259], which is based on the Flory-Rehner theory for swelling of cross-linked polymer networks [15].

Better control of the network structure can be achieved by slowly feeding the cross-linker to the monomer solution [80, 253]. Some of the fascinating properties of responsive microgels, however, might arise just from this network heterogeneity. Recently, first studies on microgels by super-resolution optical microscopy techniques were published [232, 234]. In these publications, dyes which were chemically bound to the network were employed. Here, we use an alternative approach which is based on the use of freely diffusing dye molecules penetrating the microgel network. The network density distribution of the microgel network can then be probed by the localization distribution of the fluorescent probe, which we assume to be proportional to the network density because the interaction between the cross-linker and NIPAM with the dye should be similar inside the microgel network due to the similarity in their chemical structures.

The resulting distribution of the dye molecules inside the microgels is imaged using *direct* Stochastic Optical Reconstruction Microscopy (*d*STORM). The models for the network cross-linker distribution mentioned earlier are compared and a modified fuzzy-sphere model is proposed to describe the network morphology.

3.1.1. dSTORM

Experimental setup

*d*STORM measurements were performed on an inverted microscope (IX 71, Olympus, Japan) using a high numerical aperture (NA) oil-immersion objective (60x ApoN NA 1.49, Olympus, Japan, immersion oil n=1.506 Applied Precision, a GE Healthcare Company). The rhodamine 6G (R6G) soaked microgels were excited with the 514.5 nm laser line emitted by an argon-krypton ion laser (70C-Spectrum, Coherent Inc., USA) running on all laser lines simultaneously and the 514.5 nm line was selected by an acousto-optic tunable filter (AOTFnC-VIS-TN, A-A Opto Electronic, France) and additionally filtered by a bandpass filter (ZET514/10 X, Chroma, USA). To generate a uniform illumination of the sample, the excitation light is focused on the back focal plane of the objective. A mirror mounted on a translation stage is used to move the beam entering the objective lens to change the illumination mode between widefield illumination, highly inclined and laminated optical sheet (HILO) illumination [128], and total internal reflection (TIR) [21]. The experiments were conducted in HILO mode to reduce background fluorescence from free diffusing dye molecules with 2.1 kW/cm^2 laser intensity at the sample. The fluorescence signal collected by the same objective lens was transmitted by the dichroic mirror (540DCXR, Chroma, USA) and focused by a single lens onto an EMCCD

(Electron-Multiplying Charge Coupled Devices) camera (iXON+ DU-888E-C00-BV, Andor Technology, Ireland) with a scale of 124 nm per pixel. Further, to suppress the excitation wavelength and other scattered light a long pass filter (BLP01-532R-25, Idex Corp. (Semrock), USA) and a bandpass filter (FF01-580/60-25-D, Idex Corp. (Semrock), USA) were mounted directly in front of the camera. A white light source was used to focus the microgels deposited on the coverslips. For data acquisition the manufacturer provided software (Andor Solis, Version 4.19) was used.

Image acquisition

For the super-resolved reconstructions of the microgels by *d*STORM, 50000 frames were recorded with an exposure time of 20 ms and an EMCCD camera gain of 300, where the camera was operated at -80°C . Through photobleaching and dye diffusion from the microgels into the medium, each observation area on the sample can only be imaged once. In total $\approx$ 17 min are necessary to collect the data for quantitative density distribution measurements.

Image reconstruction

To reconstruct the captured images to a super-resolved image, the ImageJ [173] plugin ThunderSTORM [197] was used. To reduce or suppress the localization from freely diffusing R6G molecules the reconstructed images are post processed with the included filters. In the first step the autocorrelation based drift correction was applied to the data to correct for sample drift over the acquisition time. In the second step, localizations with a higher localization uncertainty than 20 nm were discarded.

Localization density calculation

A custom written MatLab 2016a (MathWorks, USA) script was used to calculate the localization density within the microgels. The centers of the colloids are detected by the integrated Matlab function `imfindcircles` where only circularly shaped objects with a radius between 248 and 372 nm are recognized. The distance for each localization to each microgel center is calculated and the localization is allocated to a defined circular ring with a width of 10 nm. For the final localization density all localizations within a ring are summed up and divided by the circular ring area. The localization density is calculated up to a maximum radius of 400 nm with respect to center of a single microgel. This was done with all reconstructed microgels in the field of view. Mean value and standard error of the mean were calculated and shown in the final figure 3.8 **A**.

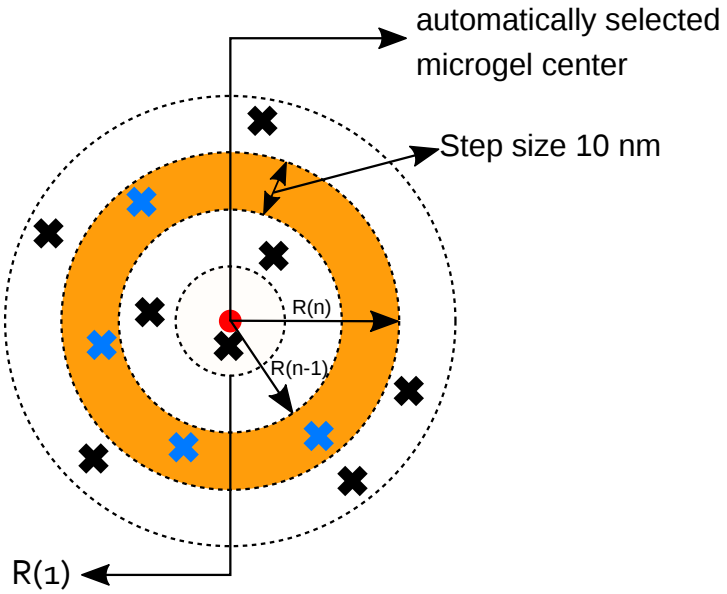

Figure 3.1.: Schematic illustration of the localization density calculation. Via the imaging tool box the microgels are recognized and the center is determined. From the center consecutive rings with a width of 10 nm are drawn and the localizations within these rings are counted. For the final 2D density calculation the total number of localizations in each ring is divided by the ring area.

3.1.2. Photon correlation spectroscopy

PCS experiments were carried out with a fixed angle setup (60 °) using a Helium-Neon-Laser ($\lambda = 632.8$ nm, Thorlabs, Newton, USA). The scattered light was detected via two photomultipliers in a pseudo-cross-correlation setup and correlated by an ALV-6010 multiple-*tau* correlator (ALV-GmbH, Langen, Germany). The temperature inside the decaline matching bath was adjusted using a computer-controlled thermostat with an equilibration time of 25 minutes per temperature. To avoid multiple scattering, the sample concentration was kept below 0.01 wt% for every sample. The measurements were analyzed using the CONTIN algorithm [20], which utilizes an inverse Laplace transformation to calculate the mean relaxation rate and therefore the diffusion coefficient.

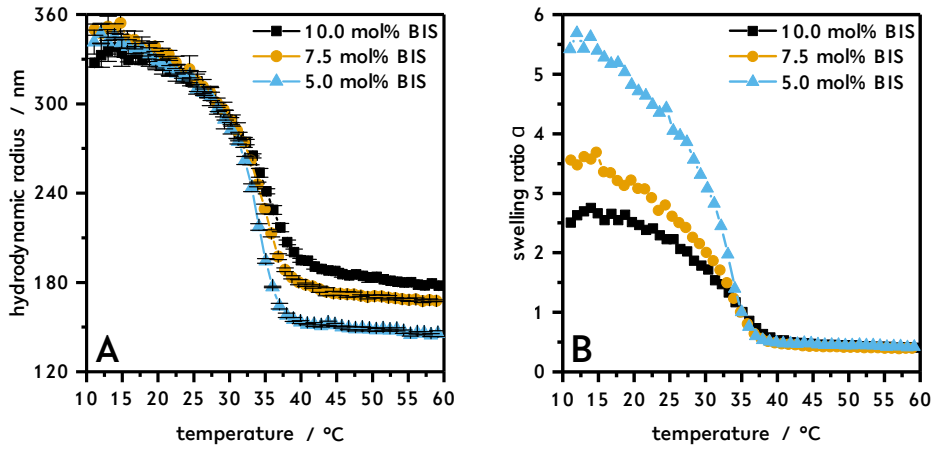

Figure 3.2.: Photon Correlation Spectroscopy experiments for microgels with different cross-linker content (5.0 (blue triangles), 7.5 (yellow circles) and 10 mol% (black squares)). In **A** the hydrodynamic radius is shown in dependence of the temperature and in **B** the swelling ratio. The figures show the normal thermoresponsive behavior of NIPAM based microgels, which exhibit a reversible phase transition from a swollen state below the volume phase transition temperature (VPTT) to a collapsed state above. The volume phase transition temperature is slightly shifted towards higher temperatures for higher cross-linker contents.

3.1.3. Fluorescence correlation spectroscopy

FCS measurements were performed on a MicroTime 200 time-resolved confocal fluorescence microscope (PicoQuant, Germany), equipped with a 510 nm pulsed diode laser (PicoQuant, Berlin, Germany) and a 60x water objective lens (Olympus, Tokyo, Japan). Temperature control is realized with an objective lens heater (Bioptechs, Butler, USA) in combination with a custom-built sample holder using #1.5H precision coverslips (Paul Marienfeld GmbH & co. KG, Lauda-Königshofen, Germany). The sample compartment has a size of approximately 0.5 mL with a cylindrical shape (5.4 mm height, 10 mm diameter). The dye concentration was kept around 1 nM. The macrogel was immersed in the dye solution for 24 hours to ensure an exchange of the network water with the dye solution.

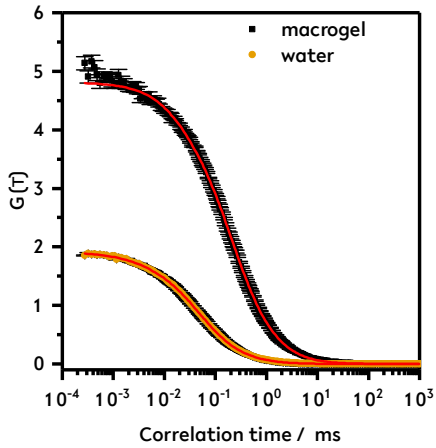

Figure 3.3.: FCS measurements of R6G in water (yellow circles) and in a macrogel (black squares) containing 5.0 mol% cross-linker. The diffusion in the macrogel is slowed down ($\sim$95 $\mu m^2/s$) in contrast to the motion in pure water (414 $\mu m^2/s$). The diffusion coefficient of the dyes in the macrogel is of the same order of magnitude as the polymer network itself. Hence, a strong interaction of the dye with the network can be assumed. However, this interaction does not lead to subdiffusive behaviour.

3.1.4. Atomic force microscopy

AFM experiments were performed on a FlexAFM (Nanosurf, Liestal, Switzerland). All images were recorded in tapping mode with Tap300Al-G cantilevers (Budget Sensors, Sofia, Bulgaria). The samples were prepared in the same way as those for fluorescence microscopy, but without the dye and with a lower concentration of the microgels (0.01 % (m/m)).

3.2. Results and discussion

The swelling characteristics of NIPAM based microgels can be tuned during synthesis by using different amounts of cross-linker. Microgel particles with 5.0, 7.5 and 10.0 mol% cross-linker were synthesized and characterized via atomic force microscopy (AFM) (figure 3.4) and photon correlation spectroscopy (PCS) (figure 3.2). PCS measurements permit to analyze the influence of the cross-linker on the swelling behavior: while the size of the swollen microgels is very similar for the different cross-linker contents, the collapsed state differs strongly in size (figure 3.2 **A**). This can be seen better, when displayed as the swelling ratio $\alpha = \frac{R_h(T)}{R_h(60\,^\circ\mathrm{C})}$ (fig-

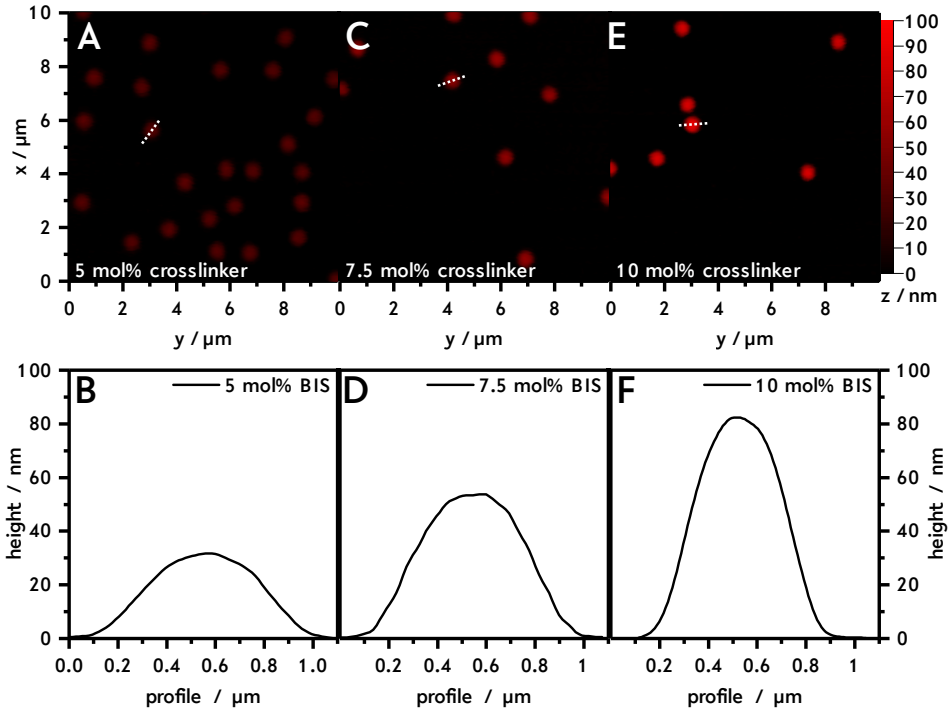

Figure 3.4.: AFM measurements of microgels with different cross-linker content (5.0 (**A** and **B**), 7.5 (**C** and **D**) and 10 mol% (**E** and **F**)). The particles were deposited as round objects with low polydispersity, which indicates the spherical nature of the microgels in solution (**B**,**D** and **F**). Cross sections of the microgels are corresponding to the white dotted lines in the upper row. The microgels on the glass substrate were in the fully collapsed state, therefore information about the density distribution cannot be gained.

ure 3.2 **B**). Additionally a shift in the volume phase transition temperature (VPTT) and a broadening of the phase transition can be seen. These observations are consistent with the previous results.

While the PCS experiments were performed in an aqueous suspension with low polymer concentration, the AFM measurements were conducted in the dry state on a glass surface. Microgels deposited onto a glass surface will not retain their lateral size, but rather spread out due to the favorable interaction between polymer and surface in contrast to polymer and air[308]. This leads to very flat particles with less than one hundred nanometers in height (see figure 3.4 **B**,**D** and **F**). Besides the

disadvantage of the inaccessible swollen state, it should also be noted that AFM is a surface sensitive technique and cannot provide insight into the very complex network morphology of a microgel particle.

In order to analyze the network morphology of microgels in a liquid environment, free-diffusing fluorescent probes were used capable of penetrating and interacting with the polymer network to gain information about the polymer network structure. Due to the good solubility in water the dye rhodamine 6G (R6G) is a suitable nanoprobe. This is demonstrated by fluorescence correlation spectroscopy (FCS) [18] measurements in a macroscopic polymer gel (macrogel) with similar cross-linker densities (5.0 mol%), but without the complex network properties due to different synthetic conditions. The diffusion coefficient is reduced by 75% inside the macrogel (figure 3.3) when compared to water. Therefore, a strong interaction between the NIPAM based polymer network and the fluorescent dye can be assumed. The result of measuring the diffusion coefficient for R6G in a macrogel $D_{\mathrm{R6G}} = 95\mu\mathrm{m}^2/\mathrm{s}$ is of the same order of magnitude as the network diffusion coefficient of macrogels[33] and microgels[56].

Hence, it is straight forward to carry out experiments where the microgels are immersed in a concentrated R6G solution and then scrutinized in single molecule localization measurements to determine the microgel network structure after initial preparation and washing steps (see A.1.3 Fluorescent labeling and microgel deposition). In single molecule localization microscopy (SMLM) a large number of images (typically several thousands) is taken in rapid succession. The addition of a specific "imaging buffer" (containing an oxygen scavenging system and thiolated molecules) [160] causes R6G to undergo rapid intensity fluctuations known as "blinking" [61]. Analysis of image sequences, where a fluorophore is initially emitting from its excited (fluorescent) state in the first image and then absent in the next image following the first one, allows one to localize the position of fluorophores with nanometer precision [57, 96, 115].

The main advantage of using freely diffusing dyes, instead of dyes directly bound to the polymer network, is the preservation of the original structure of the microgel under investigation. In figure 3.5 white light transmission microscope images of NIPAM based microgels with 5.0 **A**), 7.5 **D**) and 10.0 **G**) mol% BIS are shown. In figure 3.5 **B**,**E**,**H**) diffraction limited fluorescence images were generated by summing up all 50000 frames, which were acquired to perform localization measurements for figure 3.5 (**C**,**F**,**I**). The information which can be gained from these diffraction limited fluorescence images is restricted to the signal intensity which corresponds to a sample area of 124 nm per pixel. By applying SMLM to the microgels it is possible to extract information on the subpixel level and from single emitters (figure 3.6), which enables to determine the local dye density with high precision. Figure 3.5 **C**,**F**,**I**) shows that it is possible to perform *d*STORM reconstructions of microgels without the direct chemical binding of dyes to the polymer network. Without any

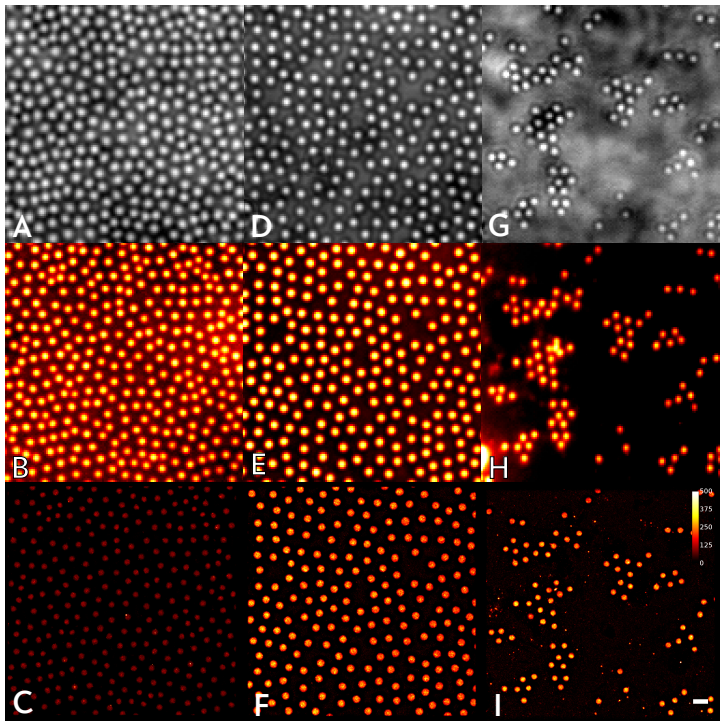

Figure 3.5.: Images **A**,**D** and **G**, are transmission light micrographs of NIPAM based microgels synthesized with 5.0 mol% , 7.5 mol%, 10.0 mol% BIS (from left to right). The middle row shows diffraction limited fluorescence images summed up from the 50000 single frames acquired for the *d*STORM reconstruction (**B**,**E**,**H**). Comparison between the white light and the fluorescence images shows that the main part of the fluorescence signal has its origin located on the inside of the microgels. The number of localizations is encoded in the color coded gray values of the reconstructed images (**C**,**F**,**I**) by applying the red hot look up table. The number of localizations is found to increase with growing cross-linker content during the synthesis. Image size is 15.87μm $\times$ 15.87μm. Scale bar 1 μm.

further data analysis it can be seen by the color scale, which is corresponding to the number of localizations, that the highest number of localizations is found in the microgels with 10.0 mol% BIS cross-linker content. Due to the identical preparation of the microgels, it can be assumed that the higher cross-linker content during synthesis leads to a denser polymer network which traps the R6G molecules more efficiently on its inside, close to the very center of the microgels. By analyzing the

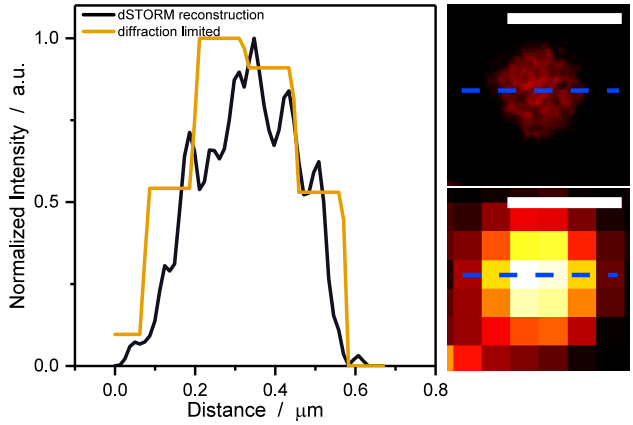

Figure 3.6.: An example to demonstrate that localization microscopy is capable of gaining a deeper insight into the microgel. Here, the diffraction limited fluorescence image and the reconstructed image of a microgel with 5.0 mol% is shown. A line plot (blue dashed line) through the same microgel indicates the higher information content which can be seen in the graph. The information gain for the diffraction limited image is limited by the number of photons collected per camera pixel. In the setup 1 pixel matches 124 nm of the sample. Scale bar 500 nm.

data with SMLM methods (figure 3.1) it is possible to quantify the network density of the microgels via the localization density projection (2D density).

From the localization density projection, calculated from rings with equal width Δr, the radial localization density profiles consisting of spherical shells of the same width can be calculated. For the calculation a matrix of volumes $V_{\mathrm{i,j}}^{\mathrm{sr}}$ is needed:

$$V_{i,j}^{\mathrm{sr}} = \frac{8}{6} \cdot \pi \cdot \left(r^2 - (r-w)^2 \right)^{\frac{3}{2}} , \tag{3.1}$$

where each volume element represents a spherical shell with the outer radius $r = R_{\max} - \Delta r \cdot i$ and a width $w = \Delta r \cdot (j + 1 + i)$, from which a cylinder with a radius of $r - w$ and a length of r is cut. $R_{\max}$ defines the maximum radius in the experiment. The size of the matrix is defined by the number of rings/shells ($n = \frac{R_{\max}}{\Delta r}$), with i and j running from 0 to $n-1$. The localization density of each shell can be calculated by dividing the localizations of the ring of the projection belonging to this shell by the respective matrix volume element. The schematic figure 3.7 shows the conversion of the collected 2D localization density into a 3D

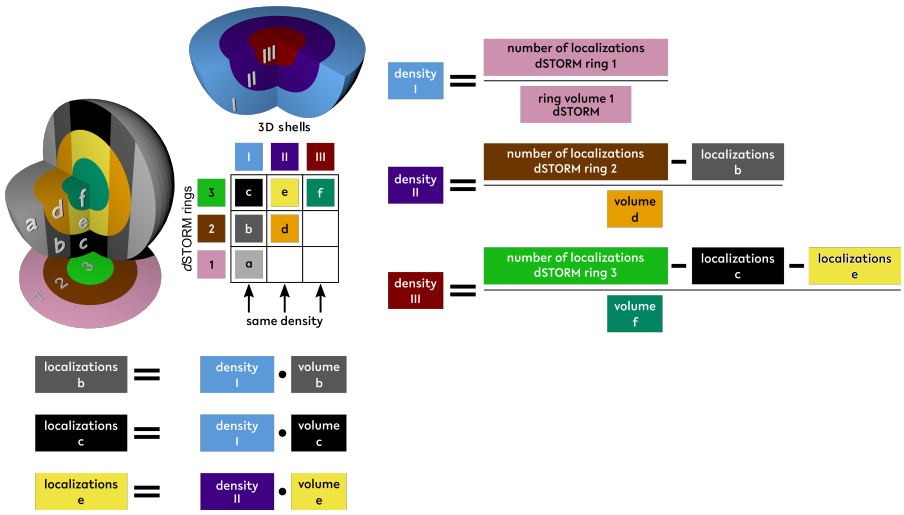

Figure 3.7.: Schematic illustration of the conversion of 2D *d*STORM data to 3D density profiles. The matrix (under the 3D shells) explains the elements needed for the calculation and their respective density. The exemplary equations show the calculation for a microgel with 3 equally spaced *d*STORM ring/shells.

localization density exemplary for 3 rings respectively 3 shells.

$$\rho_i^{\mathrm{loc,shell}}(r) = \frac{N_i^{\mathrm{loc,shell}}(r)}{V_{i,i}^{\mathrm{sr}}(r)} \tag{3.2}$$

$$N_i^{\mathrm{loc,shell}}(r) = N_i^{\mathrm{loc,proj}}(r) - \sum_{j=0}^{i-1} \rho_j^{\mathrm{loc,shell}}(r) \cdot \left(V_{j,i}^{\mathrm{sr}}(r) - V_{j,i-1}^{\mathrm{sr}}(r) - V_{j+1,i}^{\mathrm{sr}}(r) + V_{j+1,i-1}^{\mathrm{sr}}(r)\right) \tag{3.3}$$

For $i = 0$ the equation simplifies to

$$N_i^{\mathrm{loc,shell}}(r) = N_i^{\mathrm{loc,proj}}(r). \tag{3.4}$$

The results of this analysis are shown in figure 3.8 where the mean localization density projection (nm^{-2}) (see 3.1.1 Localization Density Calculation) is plotted in figure 3.8 **A**) and the localization profile density is plotted in figure 3.8 **B**). The results can be interpreted with different models: the homogeneous sphere (equation 3.5), the fuzzy sphere (equation 3.6), a Flory-Rehner inspired (equation 3.7)

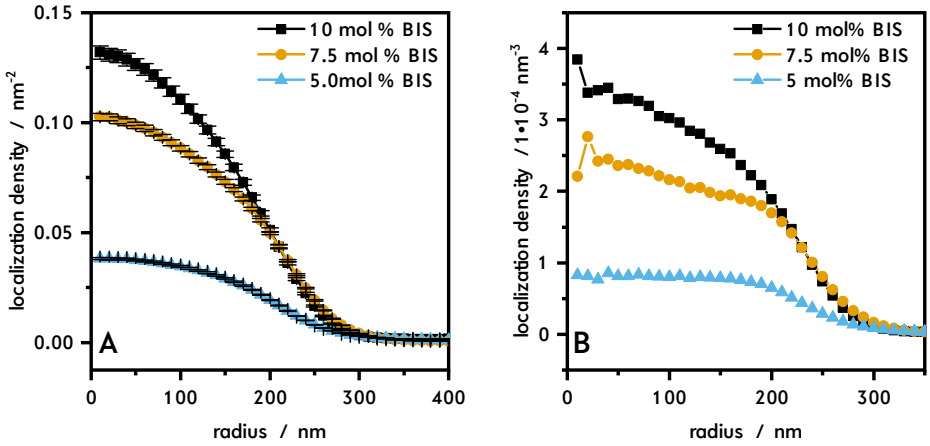

Figure 3.8.: Rhodamine 6G filled NIPAM based microgels made of different cross-linker content (5.0 (blue triangle) N=4873, 7.5 (yellow circle) N=2142, 10.0 mol% BIS (black square) N=1142) during the synthesis are investigated by *d*STORM. The mean localization density with its standard error of the mean is calculated by assigning single localizations to rings spreading out from the center of the microgel. In **A** the 2D localization density is directly taken from the reconstructed images. The calculation extending to a 3D localization density is shown in **B**.

and a modified fuzzy sphere model (equation 3.8).

$$y = \begin{cases} y_{\max} & \text{for } x \leq R \\ 0 & \text{for } x > R \end{cases} \tag{3.5}$$

$$y = \operatorname{erfc}(a \cdot (x - R_{\frac{1}{2}})) \cdot c + d \tag{3.6}$$

$$y = A \cdot \left(1 - \frac{x^3}{R^3}\right)^{\frac{3}{5}} \tag{3.7}$$

$$y = \operatorname{erfc}(a \cdot (x - R_{\frac{1}{2}})) \cdot (x \cdot c + d) + e \tag{3.8}$$

For both, the fuzzy-sphere and the modified fuzzy-sphere model the radius of the

microgel's core R_{Box} and the fuzziness of the microgel surface can be calculated by equation 3.10 and 3.9. As an estimate for the maximum size of the microgels, the hydrodynamic radius R_h calculated by photon correlation spectroscopy (PCS) measurements was used. Based on the model by Stieger [73] the error function allows determining the radius $R_{\frac{1}{2}}$, where the localization density has decreased to half of the maximum value, which is equal to the fit parameter b. With the knowledge of the hydrodynamic radius and R it is possible to calculate the decreasing cross-linking density which is described by the factor σ_{surf}.

$$\sigma_{surf} = \frac{R_h - R_{\frac{1}{2}}}{2}\,, \tag{3.9}$$

$$R_{Box} = R_{\frac{1}{2}} - 2\sigma_{surf}\,. \tag{3.10}$$

Equation 3.5 is a real space representation of the form factor for a homogeneous sphere, which has its origin in small angle neutron scattering (SANS) and is calculated in reciprocal space by

$$P_{hom}(q) = \left(\frac{3[\sin(qR) - qR\cos(qR)]}{(qR)^3}\right)^2 \tag{3.11}$$

where R is again the particle radius. The complementary error function (erfc) (equation 3.6) approximates the form factor in the real space of the fuzzy sphere model, which is an extension of the homogeneous model with a smeared particle surface with a width of σ_{surf}:

$$P_{inho}(q) = \left[\frac{3[\sin(qR) - qR\cos(qR)]}{(qR)^3}\exp\left(-\frac{(\sigma_{surf}q)^2}{2}\right)\right]^2 \tag{3.12}$$

The Flory-Rehner inspired model (equation 3.7) corresponds to the following form factor:

$$P_{\mathrm{FRI}}(q) = \left[\frac{4\pi}{V}\int_0^R r^2\frac{8}{5}\left(1 - \frac{r^3}{R^3}\right)^{\frac{3}{5}}\frac{\sin(qr)}{qr}\,\mathrm{d}r\right]^2 \tag{3.13}$$

The total network density can be tuned by the cross-linker content used for the synthesis. This is shown by the overall localization density, which is directly linked to the number of R6G molecules embedded within the network. Microgels synthesized with 10.0 mol% BIS form a denser network than microgels with 5.0 mol% BIS. This can be explained based on the chemical reaction kinetics during the microgel synthesis. The cross-linker has a higher reaction rate than the monomer.

Table 3.1.: Characterization of the microgels via fitting the density profiles with models representing the homogeneous sphere, the fuzzy sphere and the Flory-Rehner-Inspired (FRI) to the 3D localization density data of the microgels with 5.0, 7.5 and 10.0 mol% BIS. Homogeneous Sphere: R_{hom} stands for the particle radius (equation 3.5). Fuzzy-sphere: With the knowledge of the hydrodynamic radius R_{h} and the fuzziness $\sigma_{\mathsf{surface}}$, the core radius R_{Box} can be calculated with equation 3.9 and equation 3.10. FRI: The radius of the particle R_{FRI} calculated with equation 3.7.

[**BIS**] mol%	$R_{\mathbf{h}}$ nm	$R_{\mathbf{hom}}$ nm	$R_{\mathbf{Box}}$ nm	$\sigma_{\mathbf{surface}}$ nm	$R_{\mathbf{FRI}}$ nm
5.0	326	224	139	46.75	281
7.5	331	237	131.8	49.8	273
10.0	327	236	82.6	61.1	253

Therefore, more BIS is incorporated into the particle at the beginning of the microgel formation. Over time during particle growth, more and more NIPAM reacts with the newly forming particle and the reacting cross-linker content decreases. This leads to a so called fuzzy-sphere form factor, which can be reproduced for low cross-linker contents. By applying the functions mentioned above, the 3D density data results in values shown in table 3.1. From the fit results based on these models, it is possible to assume that the fuzzy sphere model is only valid for microgels with a low cross-linker content up to 5.0 mol%. If the fuzzy-sphere model is valid for highly cross-linked microgels, it would be expect that the core radius, here depicted as R_{Box}, would increase and the smeared region σ_{surf} should decrease for microgels with nearly the same size. This behavior is not observed in the data leading to the conclusion that for microgels with higher cross-linker content different models have to be applied. For higher cross-linker contents during the microgel synthesis the density of the core further increases which leads to a deviation from the fuzzy-sphere model. This deviation can be incorporated into the real-space description by expanding the error function with a linear term (equation 3.8). The linear dependence of the core density on the radius is only present for cross-linker contents above 5.0 mol%. An explanation for this might be the higher concentration ratio (cross-linker to thermoresponsive monomer) during the synthesis. For the particles containing 5.0 mol% cross-linker the low amount of BIS compensates its higher reaction rate. By increasing the BIS concentration, the higher reaction rate dominates the particle architecture again. Through the modification of the real space fuzzy sphere model with a linear contribution a description of the data for all cross-linker contents is possible. The model proposed by Schurtenberger et al. and the homogeneous sphere model do not fit the data in any case. Attempts to fit the 2D localization data with the recently published SoMaCoFit[234] stan-

Table 3.2.: Characterization of the microgels via fitting of a modified fuzzy-sphere model (equation 3.8) to the 3D localization density data of the microgels with 5.0, 7.5 and 10.0 mol% BIS. Besides the radius of the microgel's core R_{box} and the fuzziness $\sigma_{\mathsf{surface}}$, which are similar to the normal fuzzy-sphere model. The slope of the linear decreasing core density m_{core} can be fitted as well.

[**BIS**] mol%	R_{h} nm	R_{box} nm	$\sigma_{\mathrm{surface}}$ nm	m_{core} nm^{-4}
5.0	326	140	47	$1.1 \cdot 10^{-8}$
7.5	331	169	41	$3.7 \cdot 10^{-7}$
10.0	327	147	45	$7.1 \cdot 10^{-7}$

dalone software failed. With the available fuzzy sphere model it is not possible to fit the measured data to achieve a 3D density plot of the microgels without a strong regularization of the data (figure A1.3). The regularization strongly influences the calculated 3D densities in SoMaCoFit (figures A1.1 - A1.3).

3.3. Conclusion

It was shown that in contrast to previously published results the internal particle structure can be probed by determining the number and localization of dye molecules freely diffusing into the polymer network. Due to the interaction between the fluorescent probe and the dense polymer network, and the resulting extended diffusion time, an indirect labeling of the particle is achieved. This allows the investigation of chemically unaltered microgels with their specific properties (stimuli response, swelling behavior and morphology). Knowledge of the specific polymer distribution inside the colloidal particle is crucial to tune its properties towards, in this case, the coexistence of desired stimuli-response and morphology. Furthermore, this technique can be readily adapted to other solvent swollen particles, not only microgels. If the properties of the fluorophore are compatible with *d*STORM localization methods and it exhibits attractive interactions towards the network, the density distribution inside the particle can be resolved. It should also be noted that this method is fully compatible with previous measurements where the polymer network was labeled directly and should allow for a better understanding and correlation of network structure, its influence on swelling behavior, and the diffusion of external molecules into the network, which could be investigated by multi-color *d*STORM measurements.

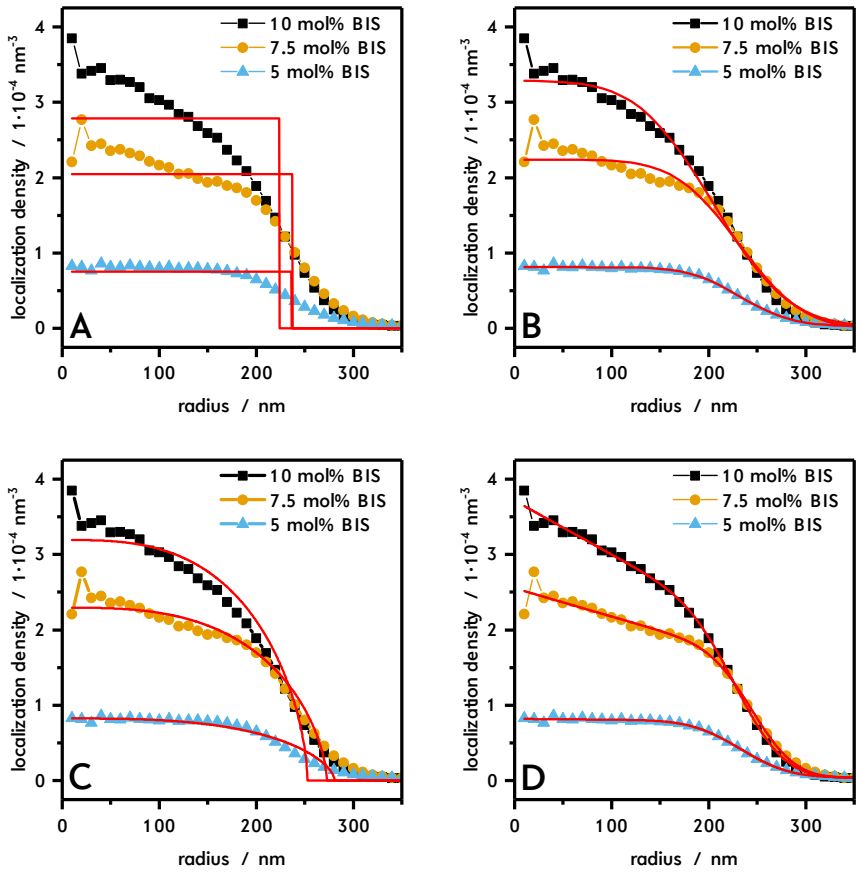

Figure 3.9.: Different models, such as the model of a homogeneous sphere (**A**), the fuzzy sphere approach in **B** and the Flory-Rehner inspired approach by Boon and Schurtenberger were applied to the data (**C**). The fit for a homogeneous sphere is only able to describe the inner box profile part of the localization density of the 5.0 mol% BIS containing microgels. Further, it can be seen that the fuzzy sphere model describes the localization distribution for 5.0 mol% BIS content accurately, but cannot describe the linear increasing localization density towards the microgels center. With the Flory-Rehner approach the microgels appear to be up to 80 nm too small, due to the hard cut off in this model. In the here developed new model the fuzzy sphere model is expanded by a linear term to include the linear increasing contribution towards the microgels' centers (**D**.)

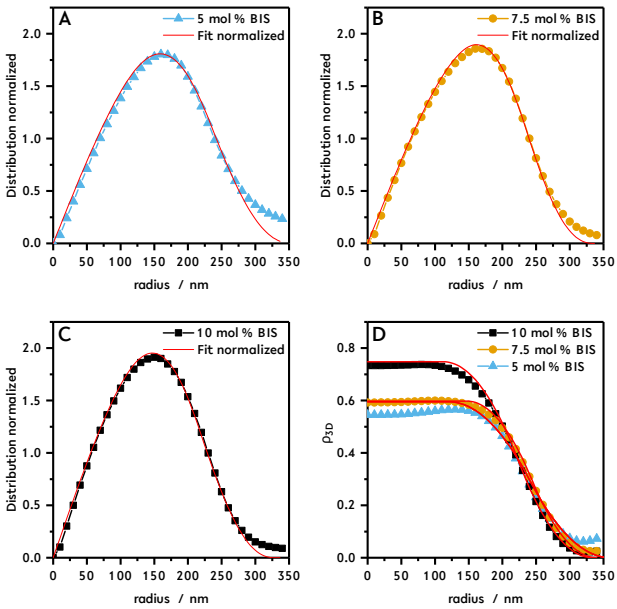

Figure 3.10.: 2D density of microgels with 5.0 **A**, 7.5 **B** and 10.0 **C** mol% BIS after regularization with $\lambda = 3.8614$. In **D** the calculated 3D density distribution after the regularization is shown for 5.0 (blue triangles), 7.5 (orange circles) and 10.0 (black squares) mol% BIS. The solid red lines are showing the fuzzy sphere model fitted to this data.

4. Smart microgels investigated by super-resolution fluorescence microscopy: Influence of the monomer structure on the particle morphology

Major parts of this chapter are based on the prepared manuscript.
Oliver Wrede[†], Stephan Bergmann[†], Yvonne Hannappel, Thomas Hellweg and Thomas Huser. Smart microgels investigated by super-resolution fluorescence microscopy: Influence of the monomer structure on the particle morphology. ([†]equal contribution)

Summary

In the previous chapter 3. "Super-Resolution Optical Microscopy resolves Network Morphology of Smart Colloidal Microgels" a simple SMLM based method is introduced to enable the investigation of microgels morphology with free diffusing dyes within the network. The fluorescent molecules remain inside the microgel network due to the favourable dye-polymer interaction. In the last preceding chapter the most used and best investigated polymer *N*-Isopropylacrylamide (NIPAM) cross-linked with *N*,*N*'-methylenbisacrylamide (BIS) was used. It is possible to extend the presented method to other microgles here, three different polymers (*N*-isopropylmethacrylamide (NIPMAM), *N*-*n*-propylacrylamide (NNPAM) and *N*-*n*-Propylmethacrylamide (NNPMAM)) with 5, 7.5 and 10 mol% BIS are studied with respect to the monomers influence on the microgels morphology.

4.1. Introduction

Microgels are spherical colloids in the size range between 100 nm and 1 μm, which internally comprise a gel network structure. The most studied microgels are based on *N*-isopropylacrylamide (NIPAM) cross-linked with *N*,*N*'-methylenbisacrylamide(BIS), which are synthesized in a precipitation polymerization [23]. The achieved particles

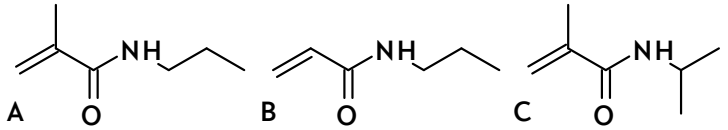

Figure 4.1.: The monomers used in the syntheses of the presented particles. *N*-*n*-propylmethacrylamide (NNPMAM, **A**), *N*-*n*-propylacrylamide (NNPAM, **B**) and *N*-isopropylmethacrylamide (NIPMAM, **C**). The main difference between polymers synthesized from these monomers are the different lower critical solution temperatures (LCST) or volume phase transition temperatures (VPTT). These are 30 °C for NNPMAM, 22 °C for NNPAM and 45 °C for NIPMAM.

are unique in their properties. More insights are available in a recently published review article [310]. Depending on the synthesis conditions, they behave more like colloids or macromolecules and can respond on external stimuli. To fine tune the properties, different polymers are investigated and used to synthesize microgels with unique response functions on temperature [171, 210], pH [69, 72, 107, 146, 163], electrochemical potentials [221] or ionic strength [50]. These features are useful as a trigger for environment depending (temperature, pH) drug delivery [81], sensors [134, 175, 205, 254], nanocatalysis [90, 91], smart surface coatings [251] or insulators [321]. Therefore, different methods can be used to investigate the response in dependence of different polymers and cross-linker densities. To gain an insight into the microgels morphology small angle neutron or x-ray scattering is often used [37, 38, 51, 55], but sample preparation is extensive and beam time is limited. In recent studies super-resolution microscopy was utilized to investigate the morphology of microgels and the comonomer distribution inside these particles [234, 259, 276]. With a simple fluorescence single molecule localization microscopy (SMLM) method it was shown in the previous chapter, that the established NIPAM morphology could be verified and new findings about the morphology of high cross-linked microgels could be gathered [276]. In addition to NIPAM microgels other polymers are available to synthesize thermoresponsive microgels [178, 252, 297].

4.2. Experimental section

4.2.1. Microscope setup

dSTORM setup

The single molecule localization microscopy experiments were performed using an argon krypton ion laser source (70C-Spectrum, Coherent Inc., USA) with the

514 nm laser line selected through an acousto-optic tunable filter (AOTF) (OTFnC-VIS-TN, A-AOpto Electronic, France). In addition, a narrow bandpass filter (Z514/10 X, Chroma, USA) was used to suppress transmitted light through the AOTF. The laser light was focused on the back focal plane of a 60x TIRF objective lens (60x NA 1.49 ApoN, Olympus, Japan) mounted on a nosepiece stage (IX2-NPS, Olympus, Japan) to minimize axial drift between sample and objective lens and to generate an almost homogeneous illumination (Gaussian intensity distribution) across the field of view. With a mirror in front of the microscope body's (IX 71, Olympus, Japan) upper rear port, the illumination scheme can be changed between total internal reflection (TIR) [21], highly inclined and laminated optical sheet (HILO) [128] and epi-fluorescence illumination (EPI), depending on the position of the laser in the back focal plane. The first separation of the excitation light from the fluorescence and reflection of the excitation light was achieved by a dichroic mirror (DCXR540, Chroma, USA). Single molecule fluorescence was detected by uncooled industry-grade CMOS cameras [262, 275]. In order to adapt the cameras' (IDS UI-3270CP Rev.2, IDS, Germany) physical pixel size of 3.45 μm to a desired image value according to the point spread functions (PSF) standard deviation, which is in practice a pixel size between 100 nm/pixel and 160 nm/pixel, a telescope (f=300 mm and f=160 mm) in the 4f configuration was included in the detection path. The fluorescence signal was filtered by a combination of a long pass filter (532 nm LP Edge Basic, BLP01-532R-25, Semrock, USA) and a bandpass filter (FF01-580/60-25-D Bandpass, Semrock, USA).

4.2.2. 3D calibration for dSTORM imaging

3D-imaging capability was achieved by adding a cylindrical lens [117]
(Thorlabs f=1000 mm, Ø1", N-BK7 mounted planoconvex round cylinder lens, ARC 350-700) in the detection arm to introduce astigmatism to gain height information from the shape of the PSF. A calibration step is required prior to 3D imaging. Therefore, 18 mm $\times$18 mm # 1.5 high precision coverslips (0107032, Paul Marienfeld GmbH & Co.KG, Germany) were used to support 200 nm TetraSpeck beads (T7280, ThermoFisher, USA) embedded in glycerol. The TetraSpeck microspheres were diluted 1:50 in double distilled water and 5 μl were pipetted to the center of the glass coverslips. Using a pipette tip, the drop was carefully distributed throughout the coverslip to create a mixture of sparse and dense regions of TetraSpeck beads. The coverslip was set aside for drying. A small drop of glycerol was then placed in the center of the coverslip with the dried TetraSpecks and a coverglass is carefully lowered at an angle from above onto the coverslip. The glycerol spreads automatically across the coverglass. The last step is to seal the slide with nail polish. For the 3D calibration a PIFOC (PIFOC P-721.10, PI, Germany) piezoelectric translation stage is mounted on top of the nosepiece stage. By removing

the connection between the objective plate and the nosepiece stage (removing the magnetic connector between objective plate and nosepiece stage) it is possible to move the objective lens independently, using the PIFOC or the coarse and fine focus knobs.

Image acquisition in 10 nm steps was achieved by a custom written Beanshell script for Micro-Manager. The function signal for the closed loop driven piezo controller (E-662.LR LVPZT Amplifier/ Position Controller, PI, Germany) was provided by a National Instruments PCIe card (NI PCIe-6259, National Instruments, USA). After acquisition of the calibration data the images were analyzed with the 3D calibration feature (see figure 5.1) implemented in the ThunderSTORM plugin [197], where the improved version by Martens et al. [286] was used.

dSTORM imaging buffer

A sparse density of molecules in the fluorescent "on-state" was achieved by usage of an a imaging buffer containing an enzymatic oxygen scavenger system combined with a thiol, in this case 1 M cysteamine hydrochloride (M6500, Sigma Aldrich) (MEA) adjusted to pH 7.4 with 25% hydrochloric acid or 1 M potassium hydroxide. The concentration in the final buffer were 60 U/ml catalase (Sigma Aldrich) and 5 U/ml glucose oxidase (Sigma Aldrich) and 100 mM MEA. A small drop, typically 20 μl imaging buffer, was added to the prepared coverslip.

Image acquisition

Due to the size of the microgels around 600 to 800 nm TIR is insufficient for imaging of the whole microgel. Therefore, HILO was used as the illumination scheme. This has the benefit of a high laser power density between 4 $kWcm^{-2}$ and 5 $kWcm^{-2}$ in the highly inclined and laminated optical sheet and the capability of suppressing the signal from free diffusing R6G molecules within the imaging buffer. For microgels with a transition temperature below room temperature (21 °C) the sample temperature was cooled down with an ice-pack on the metal objective plate. The temperature was measured with a thermometer (HH506RA, OMEGA, Germany) during the whole experiment with the thermoelement placed inside the imaging buffer. Camera control and data acquisition was realized via Micro-Manager and a modified device adapter by Marcel Müller [i]. In total 50000 images with a frequency of 50 Hz were recorded for every data set.

Image reconstruction with ThunderSTORM

For the reconstruction in ThunderSTORM a wavelet filter with the scale of two and the order of three was selected to find local maxima with the threshold of

[i] `https://github.com/biophotonics-bielefeld/ids-device-adapter/releases/tag/v0.11`

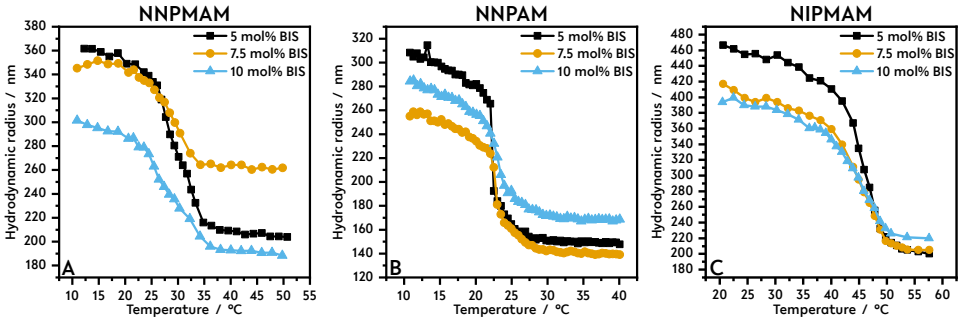

Figure 4.2.: Temperature depended hydrodynamic radius R_H measured with PCS for NNPMAM (**A**), NNPAM (**B**) and NIPMAM (**C**).

the 1st wavelet level of the input image. The localization of single emitter was then executed by elliptical Gaussian fits, with a fitting radius of 5 pixel and the method of weighted least squares. Afterwards the generated localization table is post processed by a drift correction with the in-build cross-correlation method. Therefore, the reconstruction with a final magnification of 5 times was chosen. The acquired 50000 images were divided into bins of 2500 frames and the resulting drift correction was smoothed with a factor of 0.25. In order to find single microgels an image with adjusted contrast and brightness was used to make it easier to localize separated microgels with the imfindcircle function in Matlab. For later evaluation the generated localization table was used.

4.2.3. Localization density calculation for morphology estimations

The calculation method of a 2D localization density and the proximate 3D recalculation based on the assumption to have a spherical particle are introduced and explained in chapter 3.1.1.

4.3. Results and discussion

Here, the morphology of NIPMAM, NNPAM and NNPMAM was investigated with 3D *d*STORM, where an indirect labeling strategy was used. In this approach R6G diffuses in the network and remains there due to the dye-polymer network interaction. The most obvious difference besides the chemical structure of the monomers (figure 4.1) is the volume phase transition temperature (VPTT) of the microgels, presented in figure 4.2, which shows the hydrodynamic radii R_H of the 9 different

synthesized microgels as a function of temperature. The data was calculated from PCS experiments. For microgels based on NNPMAM a VPTT of around 30 °C, for those based on NNPAM a VPTT of around 22 °C and for those based on NIPMAM a VPTT of around 45 °C was observed. The different amounts of cross-linker have only a minor influence on the position of the VPTT and the shape of the phase transition. From the projected *d*STORM images shown in figure 4.3 its possible to see first differences in the shown intensities, which indicate the number of localizations within the microgels until the microgels are not dense enough to retain the dye molecules inside the microgels. The microgels made of NNPMAN, NNPAM and NIPMAM have in common that the microgels with 5 mol% BIS appear with a bigger diameter in comparison to the higher cross-linked microgels with 7.5 and 10 mol% BIS. With the 3D capability it is possible to take a look on the xz-projections of single microgel particles and display the microgels shape as they lie on the coverslip. Figure 4.5 shows here clearly that the microgels with 5 mol% BIS (compare figure 4.5 **A** NNPMAM, **E** NNPAM and **I** NIPMAM) tend to spread over the coverslip, which is also described by Hoppe Alvarez et al. [308]. The intensity distribution of a single microgel made of NNPMAM, NNPAM and NIPMAM along the axial position can be seen in figure 4.5). The tendency to retain a spherical shape at an interface is a result of the higher cross-linked network, which does not have the same degree of freedom to distort its shape in response to an interaction with an interface. This was also observed in the previous chapter 3 by the AFM measurements on collapsed NIPAM microgels with different cross-linker densities.

A general approach to characterize the deformation is possible by fitting a spherical cap on the data. This gives the parameter R with the radius of the sphere, r the radius of the sphere segment and h the height of the sphere. The volume between the perfect sphere and the spherical cap can be used as a measure of the deformation [308]. In case for microgels with fluorophores covalently bound to the polymer network this approach might work, but in case of the indirect labeling it is only possible to image microgels regions with a sufficiently dense network structure. In addition localization with a wrong height information can occur, due to multi emitter events appearing as a single emitter with a certain PSF width and therefore a wrong height information is the result. This false positive information occurs especially in samples with a high emitter density.

From the calculated 3D localization distributions (figure 4.4) it is possible to see that some microgels deviate from the expected 'fuzzy-sphere' shape. The microgels based on NNPMAM and NIPMAM with a nominal cross-linker content of 5 mol% show the normal 'fuzzy-sphere' shape but with an increase in cross-linker deviations from this shape appear. For the NNPMAM based microgels with a cross-linker content of 7.5 mol% a shape similar to those based on NIPAM can be observed [276]. The localization density decreases linearly from the center of the particles towards the fuzzy outer layer which looks similar as those for microgels

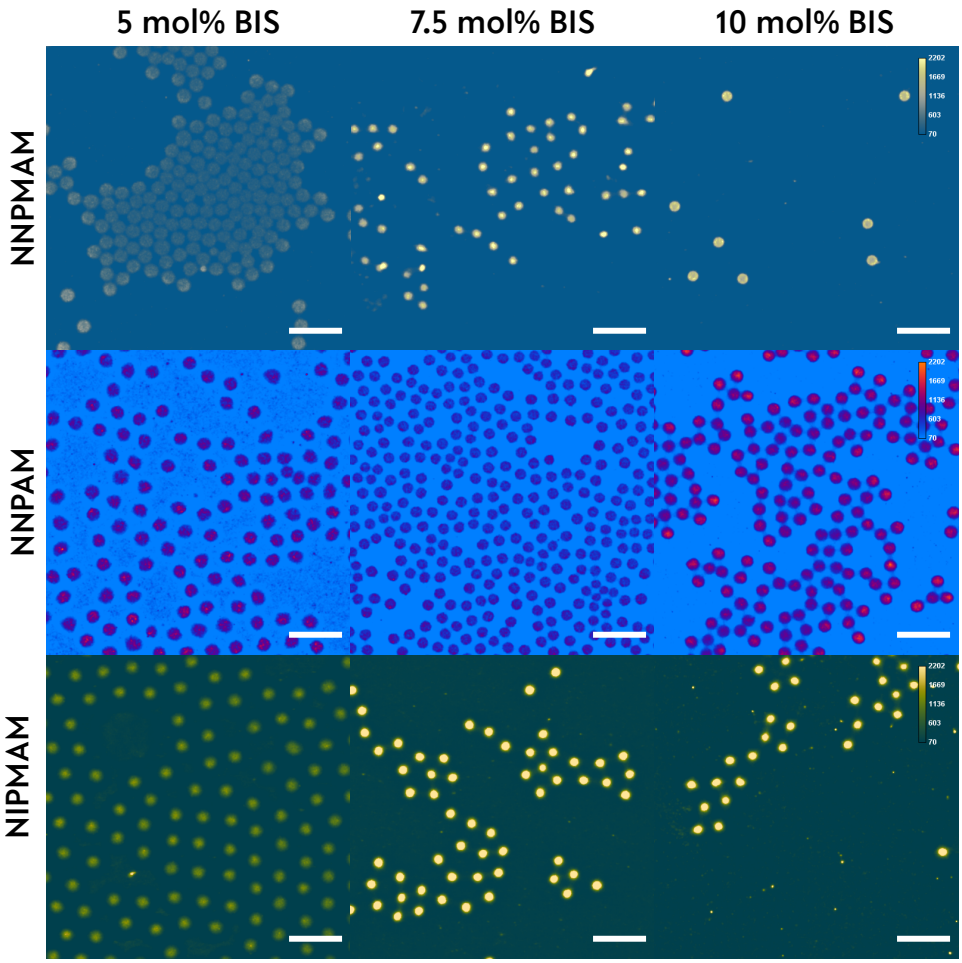

Figure 4.3.: 2D projections of 3D *d*STORM data of NNPMAM, NNPAM and NIPMAM cross-linked with 5, 7.5 or 10 mol% BIS. For better comparability the microgels made of the same polymer are visualized with the same look up table. For an overall comparison the brightness and the contrast is set to the same values (min.70 to max.2202). Based on the color coding a direct qualitative estimation of the localization density can directly be done from the reconstructed images. The microgels with 5 mol% BIS appear in the 2D projections larger, compared to microgels with higher cross-linker content. Scale bar 2μm.

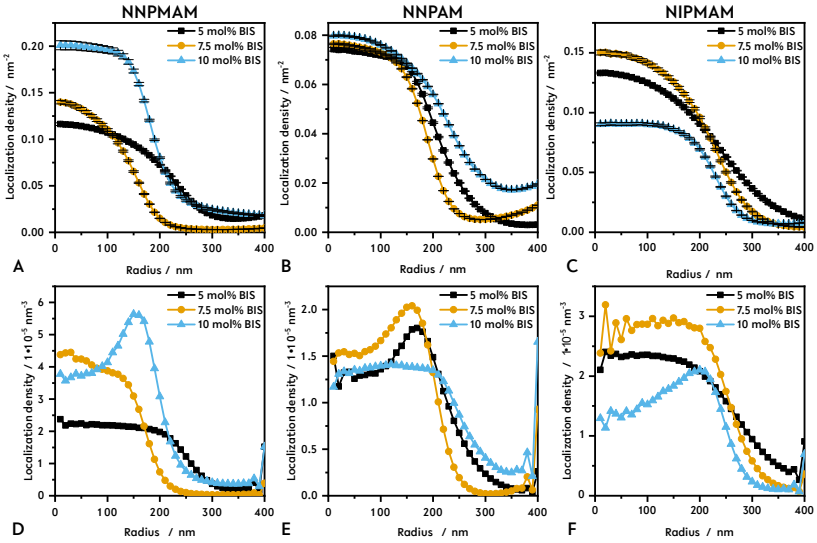

Figure 4.4.: The upper row represents the 2D localization density of the three different polymers (from left to right NNPMAM (**A**), NNPAM (**B**) and NIPMAM (**C**) with increasing cross-linker contents of 5 (black squares), 7.5 (yellow circles) and 10 mol% (blue triangles) BIS. From the localization densities it is possible to derive different properties about the interaction of the microgels with R6G. In addition the radius of the microgel can give a hint about the stability of the microgels. As previous studies have shown that the height of a collapsed microgel scales with the amount of cross-linker. Microgels with lower cross-linker amount tend to lay flatter on the substrate and therefore appear with a larger radius in the graphs. The bottom row (**D**) to (**F**) shows the corresponding 3D density recalculation assuming that microgels are spherical particles.

with the normal fuzzy-sphere shape. With an even higher cross-linker content (10 mol%) a localization density distribution similar to core-shell microgels [326] can be seen. The localization density increases from the particle center until it reaches a maximum. From there the localization density drops again similar to all other systems, indicating a fuzzy outer layer. This is caused by the dense network in the center of these particles, leading to less penetration of the freely diffusing dye in case of strongly cross-linked cores. For the NIPMAM based microgels the particles with 5 and 7.5 mol% cross-linker can still be described by the fuzzy-sphere model. For the microgels of the same material but with a nominal cross-linker content of 10 mol% again the core-shell like structure can be seen. For the NNPAM based microgels the localization density distribution for all cross-linker contents show a decline

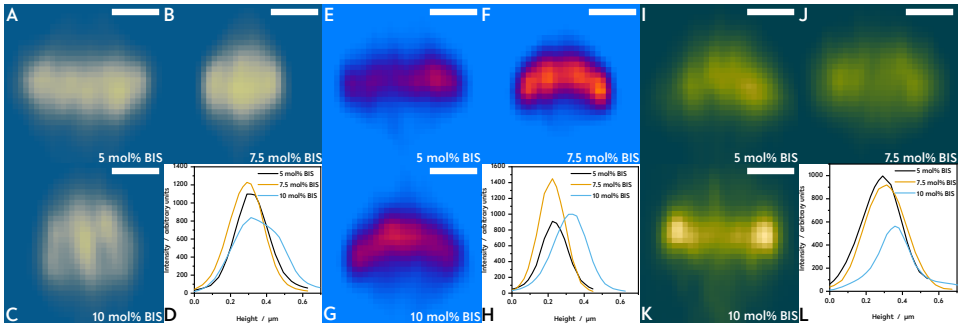

Figure 4.5.: For all microgels presented in figure 4.3 a xz-projection of a single microgel is shown. For each microgel a line plot with the width of the microgel is done. The corresponding intensity distribution against the axial position is shown in the plots **D**,**H** and **L**. Scale bar 200 nm.

towards the center of the particle. Even the particles with the lowest cross-linker density (5 mol%) show a prominent peak feature in the localization density. For the higher cross-linked NNPAM based microgels a similar shape but with a slightly higher maximum intensity and a steeper increase for the fuzzy outer layer. The particles with the highest cross-linker content (10 mol%) have a shape similar to the established fuzzy-sphere model but upon a closer look the core region is not as constant as expected. The localization density increases slightly from the particle center towards a maximum at around 33% and declines linearly towards the particle surface where a fuzzy layer is present as well. The peculiar lack of localizations in the central region of some microgels can be explained by a decreasing number of dye molecules in the particle center. This could be due to a reduction of polymer material in this region, which is counter intuitive as a higher degree of cross-linking should lead to more material. In a recent study [326], shown in then next chapter, it was found that for core-shell microgels the addition of the polymer shell leads to interpenetration of the shell material into the core network, leading to an increased polymer density in the core region [302]. Furthermore, this interpenetration leads to a reduction of the localization density in the same region. This decrease is attributed to a reduced accessibility of the core region for the dye molecules. If one now look at the microgels based on the different monomers it is possible see a similar picture. For the lower cross-linked microgels the whole particle can be accessed by the dye molecules. If the cross-linker amount is increased, the core-region becomes partially impenetrable for or saturated with R6G. With a closer look on the NNPAM based microgels the localization density distribution shows for all cross-linker contents a decline towards the center of the particle. With this new picture of a more heterogeneous density distribution inside the swelling curve

for NNPAM based microgels becomes more understandable. The much sharper volume phase transition present for NNPAM based microgels might be due to a core-corona like density distribution inside the particles. The denser region on the inside does not contribute much to the overall size transition and only collapses at slightly higher temperatures as the much lower cross-linked outer regions. This is in good agreement with recent results from measurements of the phase transition kinetics for NNPAM based microgels which showed a two stage collapse [297].

It should be noted that the localization density for NIPMAM was only calculated up to a radius of 400 nm. The figure A2.4 shows an example of the localization density up to 550 nm. This exceeds the hydrodynamic radius measured with PCS and shows that the covered radius of 400 nm is sufficient to capture the microgel regions with a sufficient dense polymer network to trap the molecules within the microgel. The increasing localization density is therefore attributed to the background of freely diffusing R6G molecules.

4.4. Conclusion

In this chapter the application of the introduced method (chapter 3.1.1) to estimate the morphology of microgels allows new insights into microgel particles based on different materials, e.g. *N*-isopropylmethacrylamide (NIPMAM), *N*-*n*-propylacrylamide (NNPAM) and *N*-*n*-propylmethacrylamid (NNPMAM), and with different cross-linker contents. By using super-resolution microscopy with a non-covalently bound fluorescent dye it is possible gain insights into the particle morphology of these thermoresponsive colloids in an state unaltered by copolymerisation of a suitable dye-anchor. A deviation from the established fuzzy-sphere model for higher cross-linked microgels is found, which indicates a highly cross-linked inner region which is no longer accessible for small molecules such as R6G. This core-region is surrounded by a lower cross-linked outer shell which gives rise to an apparent core-shell or core-corona like shape. Hence, the highly cross-linked interior of such microgels can only be probed by scattering experiments. Nevertheless, SMLM reveals interesting features of the strutcure and complements e.g. small angle neutron scattering.

5. Resolving the internal morphology of core-shell microgels with super-resolution fluorescence microscopy

Major parts of this chapter are published as a peer reviewed article.
Pia Otto[†], Stephan Bergmann[†], Alice Sandmeyer, Maxim Dirksen, Oliver Wrede, Thomas Hellweg and Thomas Huser. Resolving the internal morphology of core-shell microgels with super-resolution fluorescence microscopy. Nanoscale Advances, Advance Article (2020)
([†]equal contribution)

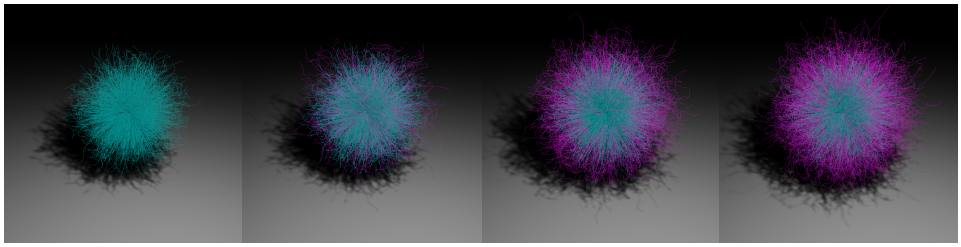

Rendered images of core-shell like microgels. The cyan color indicats the PNIPMAM core material and magenta the shell material NNPAM. With synthesis of a thin shell an interpenetration of the core material can be seen. With increasing thickness of the shell a lower number of molecules is able to diffuse to the core material.

Summary

The internal morphology of smart core-shell microgels is investigated by super-resolution fluorescence microscopy exploiting a combination of 3D single molecule localization and structured illumination microscopy utilizing freely diffusing fluorescent dyes. This approach does not require any direct chemical labeling and does not distort the network structure of these colloidal gels. Therefore, it allows the

study of particle morphology with very high precision. The structure of the core-forming seed particles is drastically changed by the second synthesis step necessary for making the shell, resulting in a core region with highly increased dye localization density. The present work shows that super-resolution microscopy has great potential with respect to the study of colloidal systems.

5.1. Introduction

Smart micro- and nanogels respond to an external stimulus, such as temperature or pH, with a change in size and therefore network morphology [49, 81, 199, 310]. For the most widely studied system based on *N*-isopropylacrylamide (NIPAM) cross-linked with *N,N'*-methylene-biscarylamide the polymer changes from a swollen network at temperatures below the so-called volume phase transition temperature (VPTT) to a collapsed particle above the VPTT ($\sim 33\,^{\circ}\mathrm{C}$ for NIPAM based microgels in water). This property grants such microgels the label "smart" and is the reason for the steadily growing interest in these systems[310]. Microgels can be used for drug delivery [122, 137], in sensors [175, 205] or as surface coatings, e.g. for vertebrate cell culture applications[203, 295]. At low temperatures the solution structure of microgel particles can be described by the "fuzzy-sphere" model, which exhibits a core-region with a constant density and a fuzzy shell where the density follows a sigmoidal decay[73]. Here, a more complex nanoscale architecture of the microgel particles is investigated: microgel particles based on *N*-isopropylmethacrylamide (NIPMAM) (VPTT in water $\sim 42\,^{\circ}\mathrm{C}$) [252] are used as seed particles for a second synthesis step, where *N*-*n*-proylacrylamide (NNPAM, VPTT of cross-linked homopolymer microgels in water: $\sim 22\,^{\circ}\mathrm{C}$) [252, 297] is polymerized in the presence of the collapsed seed particles leading to a core-shell structure [179, 261]. A peculiar feature of these particles is the linear dependence of the particle size on the temperature. This, especially with the use of the extremely fast responding NNPAM, makes them interesting candidates for sensors or nanoactuators. Recent studies using infrared spectroscopy and small angle neutron scattering (SANS) showed that during this synthesis no classical core-shell structure is generated. Instead both materials interpenetrate to a large degree[302, 323].

Recently, advances are achieved in the visualization of microgel morphology by using super-resolution fluorescence microscopy, which circumvents the optical diffraction limit [234, 276]. Single molecule localization based microscopy methods such as photoactivation localization microscopy (PALM) [88], direct stochastical optical reconstruction microscopy (*d*STORM) [115] or point accumulation for imaging in nanoscale topography (PAINT) [97, 230, 317] were used for this purpose. The difficulty with these techniques is the fluorescent labeling of the molecules of interest and the control of emitter density in the fluorescent on-state. Promising tools for the visualization of the cross-linking density are diarylethene photoswitches [288,

290] or functionalized organic fluorescent molecules [282] integrated in the polymer network. A different approach for the visualization of the microgel morphology is an indirect approach, where freely diffusing rhodamine 6G (R6G) molecules interact strongly with the network and their diffusion is effectively slowed down to allow *d*STORM measurements [276]. This approach allows to study the network by *d*STORM without major perturbation of its structure [276]. The aim of the present work is to show the rather broad applicability of this approach also to more complex colloidal structures. Therefore, the method introduced in chapter 3 is applied to the investigation of core-shell particles (NIPMAM-NNPAM). The influence of different shell thicknesses on the microgels' properties is scrutinized with respect to finding promising candidates for drug delivery [122, 306, 325] or nanocatalysis [298]. The results are then benchmarked against SANS results for similar particles [302].

5.2. Experimental Section

5.2.1. Microscope setup

dSTORM setup

The used fluorescence microscope for the performed experiments with core-shell microgels is described in the previous chapter 4.2.1. Due to the derivation from the defocus model in addition to ThunderSTORM [197, 286] a more sophisticated tool box is used to deal with these problems. The settings are explained in section 5.2.2.

DMD-SIM setup

For 2D-SIM measurements it is required to generate a sinusoidal pattern in the sample which is typically done with spatial light modulators. Additionally, the pattern needs to be rotated and shifted three times, resulting in nine recorded raw frames. Here, a digital mirror device (DMD, DLP6500FYE, Texas Instruments, Dallas, TX, USA) was used as a spatial light modulator to create the SIM pattern and to perform the experiments [319]. At the setup, a 532 nm diode laser (532MD-100-FB-12V-2, Q-BAIHE, Wuhan, China) was used for the excitation which first illuminates the DMD. Afterwards, polarization optics were implemented in the optical path to generate the best possible SIM illumination. Note, that two dichroic mirrors (Di03-R532-t3-25x36, Semrock, USA) were needed to maintain the polarization settings. With additional lenses the laser was focused to the back-focal plane of the objective lens (UPLSAPO60XO, 1.35 NA, Olympus, Japan). With the same objective lens the fluorescence signal is collected, filtered (FF01-575/59-25, Semrock, USA), and detected with a camera (IDSμEye UI-3060CP-M-GL Rev.2,

Germany). The nine raw frames were then reconstructed to a super-resolved image [242].

5.2.2. 3D calibration for dSTORM imaging

To overcome problems with aberrations due to misaligned lenses and the characteristic PSF of the objective lens a different approach for 3D *d*STORM reconstruction is pursued. Specifically, the superresolution microscopy analysis platform (SMAP) developed by Jonas Ries (Superresolution microscopy for structural cell biology, EMBL, Heidelberg, Germany) was applied in this case. The performance of the toolbox was evaluated in a recent comparison between different 2D and 3D single molecule localization microscopy software packages [318]. An additional toolbox, the published cspline algorithm by Li et al. [285] was used, which allows a model free 3D calibration (figure 5.1 **E** to **J**). The previous evaluation of the acquired calibration step was performed with the given default settings in the SMAP tool box. As general parameters the arbitrary 3D modality was chosen and the distance between the images was set to 10 nm according to the step size of the PIFOC during data acquisition. The axial position of the bead was corrected via a cross-correlation of 50 frames. For peak finding the filter size was set to two with a relative cutoff of one. Due to the high signal to background ratio the cutoff does not have to be increased. To exclude overlapping PSFs from different beads, the minimum distance between two peaks has to be at least 25 pixels. For the final cspline fitting a region of interest of 27 in x- and y-direction was chosen. A parameter value of one for smoothing in axial direction was also applied.

5.2.3. dSTORM imaging

A sparse local density distribution of molecules in the fluorescent "on-state" is achieved by the application of a *d*STORM imaging buffer containing an enzymatic oxygen scavenger system combined with a thiol, in this case 1 M cysteamine hydrochloride (M6500, Sigma Aldrich) (MEA) adjusted to pH 7.4 with 25 % hydrochloric acid or 1 M potassium hydroxide. The concentrations in the final buffer are 60 U/mL catalase (C100-50MG, Sigma Aldrich, USA), 5 U/mL glucose oxidase (G2133-10KU, Sigma Aldrich, USA) and 100 mM MEA. A small drop, typically 20 μl of the imaging buffer was added to the sample slide. The advantage of adding only a small drop to the slide is, that the remaining sample is not altered during the acquisition process by the imaging buffer (diffusing dye molecules). With the HILO illumination scheme the best results are achieved because the free floating R6G molecules above the microgels were not excited. In order to translate most of the fluorescent molecules into the long lived dark state via the triplet state in combination with thiols, a laser power density between 4 kW cm^{-2} and 5 kW cm^{-2} was

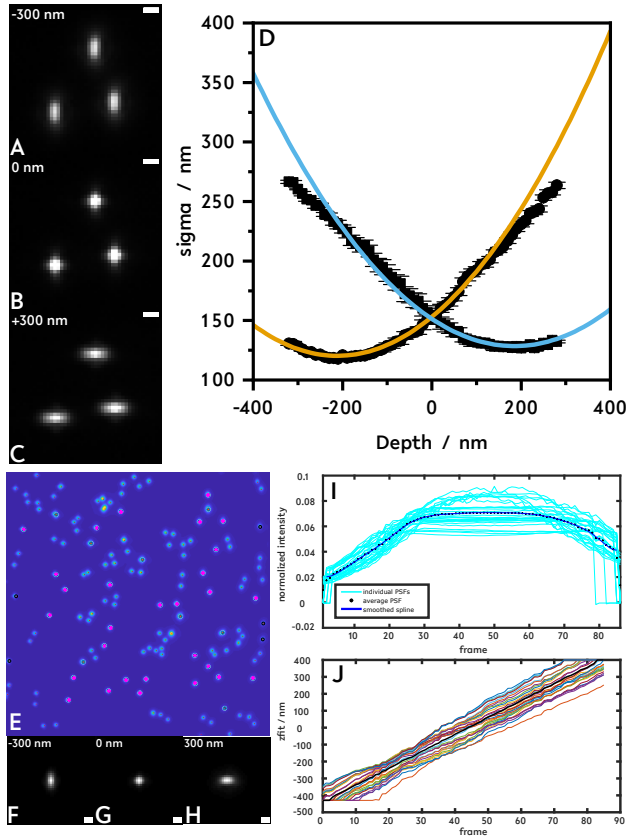

Figure 5.1.: 3D calibration based on 200 nm Tetraspeck beads embedded in glycerol and analyzed with ThunderSTORM. The objective lens was moved by the PIFOC stage in 10 nm steps through the sample to measure a height dependent PSF of the beads. The applied model (orange and blue curve) deviates from the ThunderSTORM calibration. Therefore, a more sophisticated method was used for the 3D reconstruction **E** to **J**. To account for the deviation from the standard model for 3D imaging, the superresolution microscopy analysis platform (SMAP), a more advanced reconstruction software by Jonas Ries (EMBL), was used. The same data set was analyzed with this toolbox in combination with the fit3Dcspline algorithm [285]. In **E** the maximum z-projection of the single fluorescent beads is shown. Beads with a distance of 27 pixels to each other were selected from this image for 3D-cspline calibration. From all matching fluorescent beads an averaged point spread function (PSF) was calculated (**F** to **H**) and a 3D calibration is generated by a cspline fit. Therefore, different views are generated. **I** visualizes the PSFs profile along the z-axis in the middle of the PSF at x=0 and y=0. The resulting height calibration from 37 single fluorescent beads is shown in **J**. Scale bar 500 nm.

applied to the sample. In total 20000 frames were acquired, where the imaging frequency for the core-only microgels was set to 50 Hz and for the core-shell microgels to 30 Hz. For imaging of the swollen state of the microgel at 17 °C (see figure 5.3 **A** and figure 5.2 **A**, **D**, **G**) the objective plate is cooled down with an ice-pack, and the temperature is measured with a thermoelement (HH506RA, OMEGA, Germany) within the imaging buffer solution.

2D-SIM imaging

As in the *d*STORM measurements, the microgels were embedded in water at 17 °C, and therefore were in the swollen state. However, for optimal 2D-SIM it is crucial to match the refractive index of the used immersion oil because otherwise spherical aberration will result in a poor resolution enhancement. Due to the lowered temperature it becomes necessary to lower the refractive index of the immersion oil in order to achieve the same SIM results compared to imaging at room temperature. Therefore, an immersion oil of 1.51 NA instead of 1.518 NA was chosen. For the imaging process the laser power was set to approximately 250 μW at the sample and the exposure time was 50 ms for a single raw frame. In contrast to *d*STORM, only nine frames were needed for a 2D-SIM reconstructed image, and therefore the recording only lasts half a second. Latest software development allowed real-time reconstruction, so that the super-resolved SIM image could be observed immediately [312].

5.2.4. Image reconstruction

ThunderSTORM

For the reconstruction in ThunderSTORM [197, 286] a wavelet filter with the scale of two and the order of three is selected to find local maxima with the threshold of the 1st wavelet level of the input image. The localization of single emitters is then executed by elliptical Gaussian fits, with a fitting radius of 5 pixels and the method of weighted least squares. The generated localization table is afterwards post processed by only a drift correction with the built-in cross correlation method. Therefore, a reconstruction with a final magnification of 5 x was chosen. The acquired 20000 images were divided into bins of 1000 frames and the resulting drift correction is smoothed with a factor of 0.25. For finding the single microgels an image with adjusted contrast and brightness is used to make it easier for the imfindcircle function to localize the single microgels. For the later evaluation the resulting localization table is used.

fairSIM

For the SIM reconstruction the Fiji plugin fairSIM [242] was used. The image processing was started by subtracting background signal, namely 75 counts, and corrected for the different illumination intensities in phase and angle. Further, an estimated optical transfer function (OTF) was utilized with an estimated emission wavelength of $\lambda = 575\,\text{nm}$, an attenuation of a=0.3 and an oil immersion objective lens (NA=1.35). For the SIM reconstruction itself, a Richardson-Lucy deconvolution algorithm (one iteration) was applied to the input and output data.

Superresolution Microscopy Analysis Platform (SMAP)

As previously described, the calibration data set was used for the 3D reconstruction of the core-shell microgels. As a first step a wavelet based background estimation was done and the images were corrected for this background. Between the background correction and the peak finding step differences of Gaussians with a σ of 1.2 in camera pixels were applied. The signal cutoff is calculated dynamically via the distribution of pixel intensities were the sensitivity was set to 1.5. For a more precise localization in depth the model free cspline algorithm by Li et al. [285] was used with the standard setting and with a refractive index mismatch correction, where the value was set to 0.85. In contrast to the standard settings of SMAP, all localizations were saved and later during the post processing, localizations were filtered by their localization precision in lateral and axial directions. The built-in drift correction serves to correct the lateral drift. Therefore, the image stack is divided into 10 bins containing 2000 frames each. For the final 3D reconstructed images a Gaussian renderer was used, where the color coding (LUT jet) shows the microgels within a depth of 100 nm (dark blue) to 400 nm (dark red). Localizations with its origin under -100 nm and over 400 nm are artifacts from freely diffusing R6G molecules above the microgels and under -100 nm is the cover glass where no localizations should occur. Only localizations with a lateral precision $< 30\,\text{nm}$ and an axial precision $< 45\,\text{nm}$ were taken into account. The xz-projections were generated by 300 nm thick sections, shown with white dashed lines through center of the microgel.

5.3. Computational Methods

5.3.1. 3D quantification of 2D projected single molecule localization microscopy data

For the quantification of the super-resolved single molecule localization data that resulted from the experiments a drift corrected localization table was used as well as the resulting reconstructed image to identify the center of the microgel by the

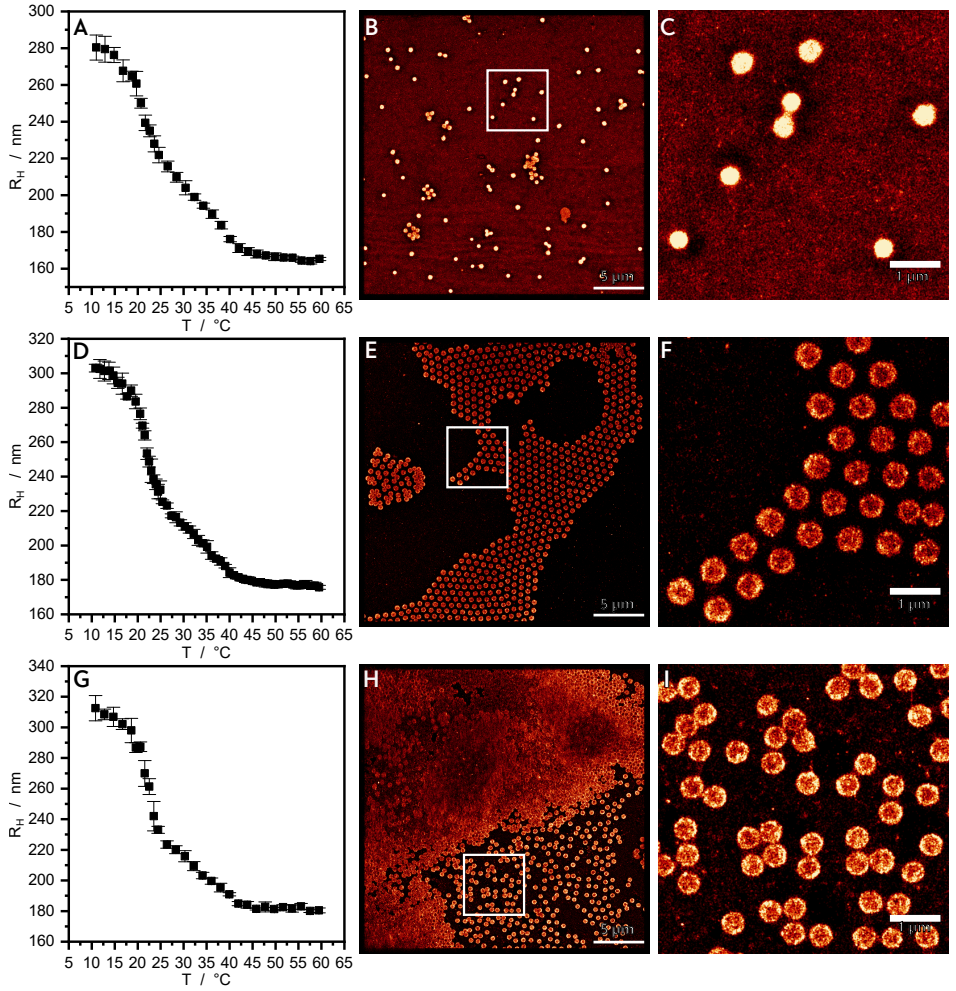

Figure 5.2.: A, **D** and **G** show the swelling curves of the three core-shell microgels with nominally increasing shell thickness from thin, over intermediate to thick. The shell thickness is varied according to the synthesis described in the appendix A.3.1. The reconstructed *d*STORM images (**B**, **E** and **H**) for the microgels with different thick thicknesses are displayed with increasing shell thickness from the top to the bottom. Images on the right hand side (**C**, **F** and **I**) are the zoomed in versions of the white highlighted regions of interest.

built-in function imfindcircle, which provides the coordinates of the center and the radius of the microgel based on the image. This function was also used to filter for spherical objects with a radius between 67.2 nm and 336 nm for the core microgels and between 224 nm and 448 nm for the core-shell microgels. From each localized center the number of localizations in rings of 10 nm thickness is counted until a radius of 400 nm is reached (see figure 3.1). The final localization density of each ring was calculated by the total number of localizations in the ring divided by the ring area. The final localization density for the core-only and the core-shell microgels is shown in figure 5.6 **A**, where the mean value is displayed with the standard error of the mean. From the 2D projection it is possible to recalculate a 3D density under the assumption that a spherical object is considered. The math necessary for this recalculation is introduced in chapter 3.2 with the equations 3.1 to 3.4. The contributions of single rings to the shells is schematically shown in figure 3.7.

5.3.2. Normalized integrated intensity profile for 3D recalculation of 2D SIM data

To achieve a similar 3D recalculation based on the SIM reconstructed images an additional step was needed to generate a normalized integrated intensity profile over the microgels. In ImageJ are two plugins[ii] ,[iii] available which are capable to generate this information. In contrast to the SMLM measurements the microgels center was set manually in ImageJ. The calculated normalized integrated intensity in dependence of the distance from the center for each microgel was averaged and the standard error of the mean was calculated. All microgels taken into account are highlighted with a white circle (see figure 5.9 **C** to **E**). In comparison to the 3D recalculation the normalized integrated intensities are pixel dependent and therefore the width of a single ring area is restricted to the pixel size of the super-resolved SIM image. For the SIM reconstructed images the pixel size is 35 nm. A consequence due to this limitation might be a deviation of the normalized signal from the findings with SMLM, in particular in the core region.

5.4. Results and Discussion

5.4.1. Measurements on PNIPMAM core particles

The PNIPMAM core microgel particles were characterized as synthesized in aqueous suspension by photon correlation spectroscopy (PCS) (figure 5.3 **A**) to deter-

[ii] Baggethun, Radial Profile Plot, `https://imagej.nih.gov/ij/plugins/radial-profile.html`
[iii] Carl, Radial Profile Extended, `http://questpharma.u-strasbg.fr/html/radial-profile-ext.html`

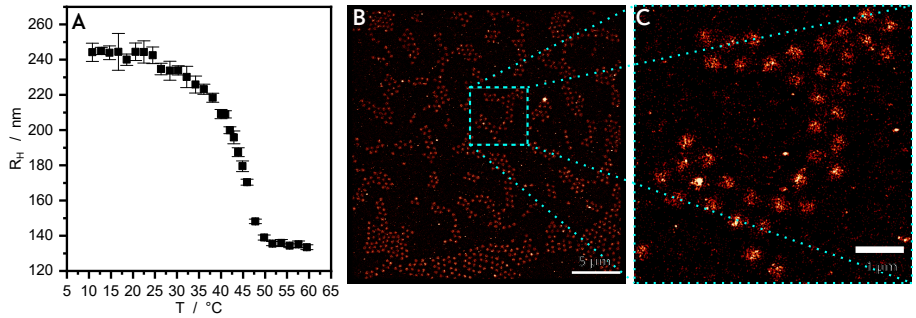

Figure 5.3.: The temperature dependent swelling behaviour of microgels made of PNIPMAM, which are subsequently used as cores, is here characterized by PCS shown in **A**. In **B** a *d*STORM reconstruction of the microgels is presented, where **C** is the zoom-in of the cyan highlighted area in **B**.

mine the temperature-dependent hydrodynamic radius R_H and the swelling behaviour. The PNIPMAM core particles contain a cross-linker content of 10 mol%. The PCS measurement was performed in a temperature range from 10 to 60° at a scattering angle of 45°. The data was analyzed by the CONTIN algorithm. At low temperatures the particles are swollen and they have a R_H of approximately 240 nm. At approximately 42 °C the core particles collapse and their hydrodynamic radius decreases to a plateau value of approximately 135 nm. This thermoresponsive behaviour is typical for an amide-based microgel and the collapse of PNIPAM in H_2O can be seen at 42 °C [85, 178]. The collapsed and dried core particles were characterized by atomic force microscopy (AFM, section A.3.3). In figure A3.5 **A** the AFM measurement of these particles are shown. The particles are identifiable as circular profiles with a low polydispersity. In addition to the localization densities it is also possible to probe the polydispersity based on SMLM. The in Matlab integrated function 'imfindcircle' transfers in addition to the center coordinate of the circle the circle radius. The calculated radii (see figure 5.5) are in good agreement with the measured hydrodynamic radius R_H for the different core-shell microgels. The deviation of the measured radius for the core-only microgels might be due to the low number of molecules localized within the core. This makes it more difficult to recognize the edge of the localizations in respect to the background. In addition to the small number of detected molecules, the core microgel morphology might promote the too small appearing core by a small highly cross-linked core and dangling chains without the capability to trap the R6G within the network.

For the super-resolution fluorescence microscopy measurement the fluorescent dye R6G was used. The PNIPMAM core microgel particles are mixed with an aqueous R6G solution. During this time the dye molecules diffuse into the swollen

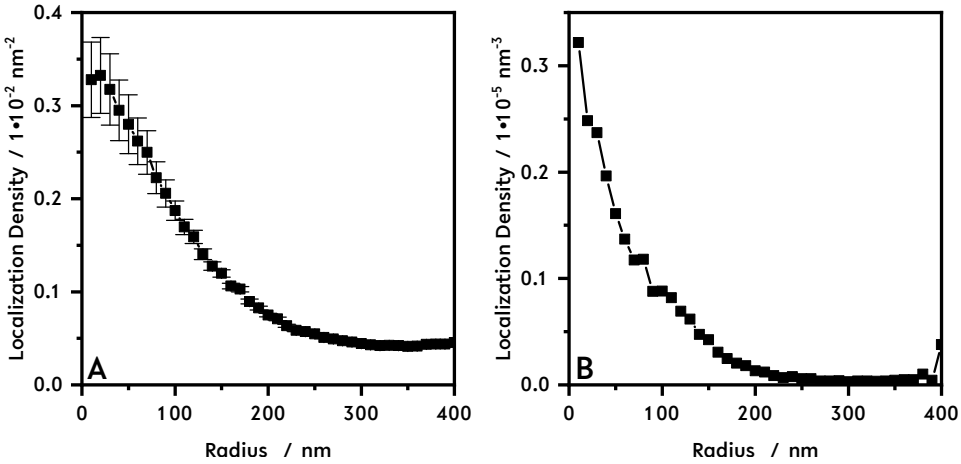

Figure 5.4.: In **A** the 2D localization density of the core-only microgel (N=1048) is plotted following the calculation model shown in figure 3.1. In **B** the recalculated 3D localization density is shown.

polymer network due to favorable interactions. The nature of this interactions is still unclear. Coulomb or hydrophobic interactions are possible but the latter have a higher probability to take place, which is shown with measurements by Zhou et al. that the initiator charges are localized in the area near the particle surface [180].

After a few days this solution was diluted again and was placed onto a coverslip coated with polyethylenimine by spin-coating. The *d*STORM measurements were performed in an buffer (see section 5.2.3). The R6G molecules freely diffuse into the microgel particles so that the "blinking" of single fluorophores can be recorded. The recorded localizations were summed up to generate the reconstructed images.

In figure 5.3 **B** the reconstructed *d*STORM images of the core microgel particles with the freely diffusing R6G are shown. Figure 5.3 **C**, shows an enlarged section of this image. In the background the localization density is almost zero. For the pure core particles the highest number of dye molecules is located in the middle of the particles. The 2D localization density of the pure core microgel particles (figure 5.4**A**) can be determined from the reconstructed images and the 3D localization density is recalculated (figure 5.4**B**). The localization density of the R6G fluorophores is highest in the middle of a core particle and decreases drastically with increasing particle radius. As already mentioned above, this is different compared to PNIPAM microgels which show a plateau or at least a large linear zone in the densities of the inner part of the particles. In a previous study using AFM it was also shown that PNIPMAM microgels seem to exhibit a different

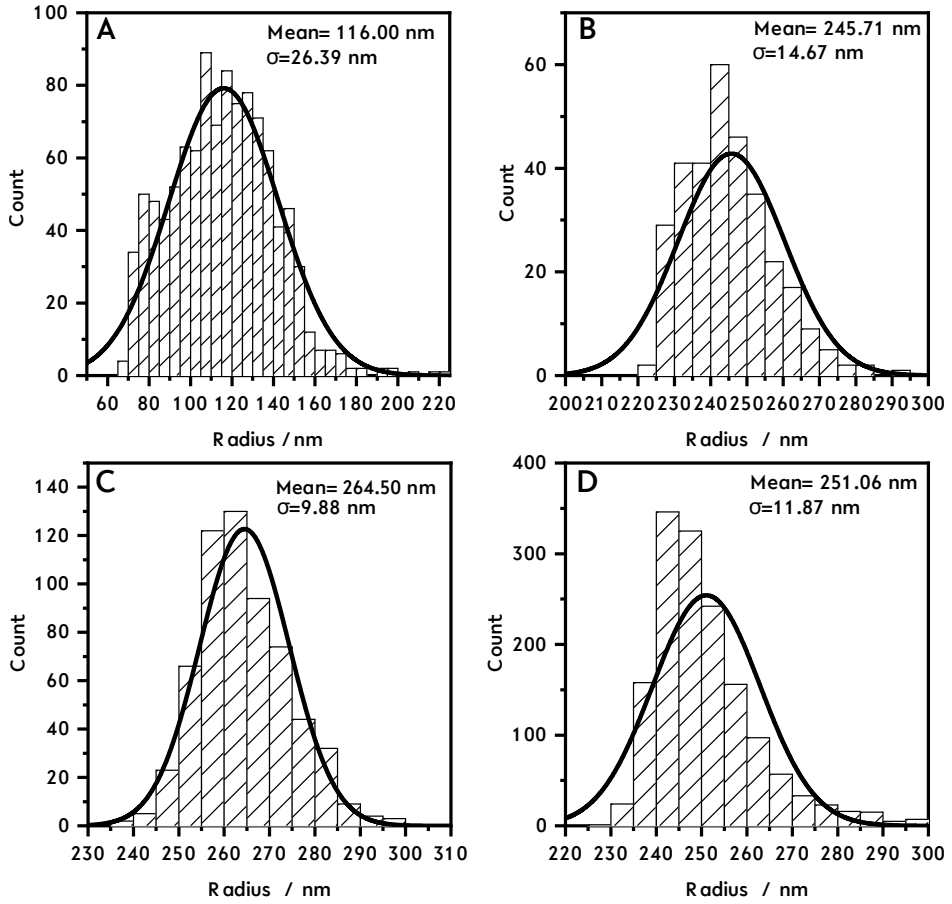

Figure 5.5.: The histogrammed microgel radii for core-only microgels (**A**) deviate strongly from the measured hydrodynamic radius measured via PCS at around 16°C (see figure 5.3 **A**) and show a radius half of the measured hydrodynamic radius $R_H \approx 240\,\mathrm{nm}$. The total number of localized dye molecules is lower in comparison to the core shell microgels and the reconstructed image is less well defined. The imfindcircle function has therefore problems to recognize the radius properly. By adding the shell to the core, the estimated radii of the different core-shell microgels is getting in the range of the hydrodynamic radii (see figure 5.2 **A**,**D** and **G**), but remains too small. Therefore, with the fluorescent dye molecules it is only possible to probe sufficiently dense microgel networks with the property to trap the dye inside the microgel during both, the washing steps and imaging within an aqueous buffer.

network structure compared to PNNPAM and PNIPAM microgels [252]. The size of a swollen core particle is found to be approximately 240 nm just as in the PCS measurement (see figure 5.3 **A**). This is similar to the previous chapter 3 and shows the approach is also useful to characterize the morphology of microgels based on different acrylamides [276].

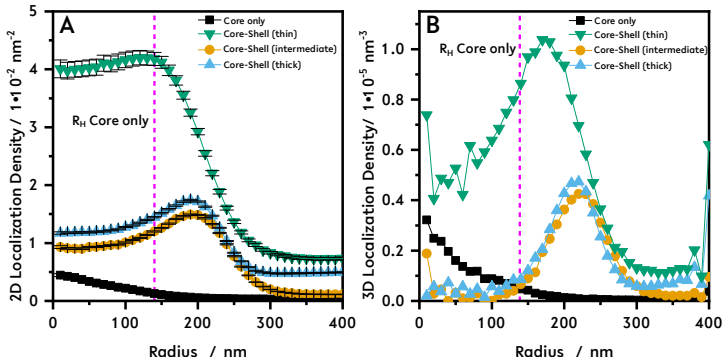

Figure 5.6.: The microgels are immersed in R6G solutions and spincast on PEI coated coverslips. To remove excess dye molecules the sample is washed with purified water while spincasting. The remaining dye molecules in the microgels were localized. The localization densities were acquired by *d*STORM imagign, of core-shell microgels with three different shell thicknesses termed as "thin" (green triangle, N=314), "intermediate" (yellow circle, N=608) and "thick" (blue triangle, N=1512) with a cross-linker content of 10 mol% for the core and 2 mol% for the shell during synthesis. Therefore, the presented scheme for data evaluation (see figure 3.1), after getting the localization table, was used. Localizations were counted and assigned to circular rings with a width of 10 nm. From this it is possible to calculate a localization density for each ring. This was done for the core-only and the three different core-shell microgels. The 2D localization density shown in **A** shows a higher localization density for all the core-shell microgels over the whole radius in comparison to the core-only microgel. In **B** the recalculated 3D density for all measured microgels is shown. The hydrodynamic radius R_H of the collapsed core-only microgels is indicated by the dashed line in magenta in both graphs.

5.4.2. Measurements on the core-shell system

The three different core-shell particles were analyzed analogously to the pure core particles. The PNNPAM shell contains a cross-linker content of 2 mol% for each of the three core-shell systems and different thicknesses (thin, intermediate and thick). In the swelling behaviour measured by PCS (figure 5.2 **A** ,**D** and **G**) of all

three systems it is possible to observe three regions [179]. In the first region at lower temperature all particles are in a swollen state with a size of the hydrodynamic radius of 280 - 315 nm. The collapse of the PNNPAM shell is observable at approximately 21 °C [40]. This transition becomes larger from microgels with a thin to those with a thick shell. The second region shows a linear relation between the hydrodynamic radius and the temperature, which is caused by an interpenetration of the NNPAM shell material into the PNIPMAM core [302]. The particle size decreases with increasing temperature. In the third region the particles are completely collapsed and the hydrodynamic radius reaches a plateau value of 170 - 180 nm. The structure of the shell region does not change. Core and shell show a thermoresponsive behaviour, which was also shown by Zeiser et al. [179] and Cors et al. [261] on comparable core-shell systems. The AFM measurements of the core-shell particles are shown in figure A3.5 **B**-**D**. Here, it is possible to see the circularity in shape and a low polydispersity of the particles. In figure 5.7 **A** to **C** reconstructed 3D *d*STORM images can be seen. A slight distortion from the spherical shape of the microgels at the solid liquid interface is observable. This was already reported by Hoppe Alvarez et al. [308] and is due to interactions between the particles and the interface.

In figure 5.2 **B**, **E** and **H** the *d*STORM reconstructed images of the core-shell microgel particles with freely diffusing R6G are shown. Figure 5.2 **C**, **F**, **I** and **H** show enlarged sections of these images. For the intermediate and thick shell (figure 5.2 **E**,**F** and **H**, **I**) the highest intensity is seen in the shell region. For the thin shell (figure 5.3 **A**, **B**) a much higher intensity is observed. In all of the images there is only a negligibly small intensity in the background.

In figure 5.6 the 2D (**A**) and 3D (**B**) localization densities of the core-shell particles with the three different shell thicknesses are shown. In the region of the theoretically collapsed core (up to ∼140 nm) the localization density differs strongly from the pure core particles. For the thin shell (figure 5.6 green triangle) a higher localization density can be seen which might be caused by a higher interaction of R6G with the core-shell system containing PNNPAM, as the sum of all localizations is higher for the collapsed-core region of the thin shell system as for the complete core-only particles. An alternative explanation to a compressed core is the interpenetration of the monomer NNPAM into the collapsed core during the synthesis. The higher localization number which might be due to the interpenetration of the NIPMAM based core can also be seen in the 3D *d*STORM reconstructions of the microgels with thin shell in figure 5.7 **A**. In particular, this can be seen in the xz projection across the core region 5.7 **A** 1-5, where clearly localizations within the core region are visible. This is in good agreement with recent small angle neutron scattering (SANS) results using contrast variation [302].

The NNPAM content increases from the inside to the outside, due to the inhomogeneous cross-linker density of the core, so that outside of the core region

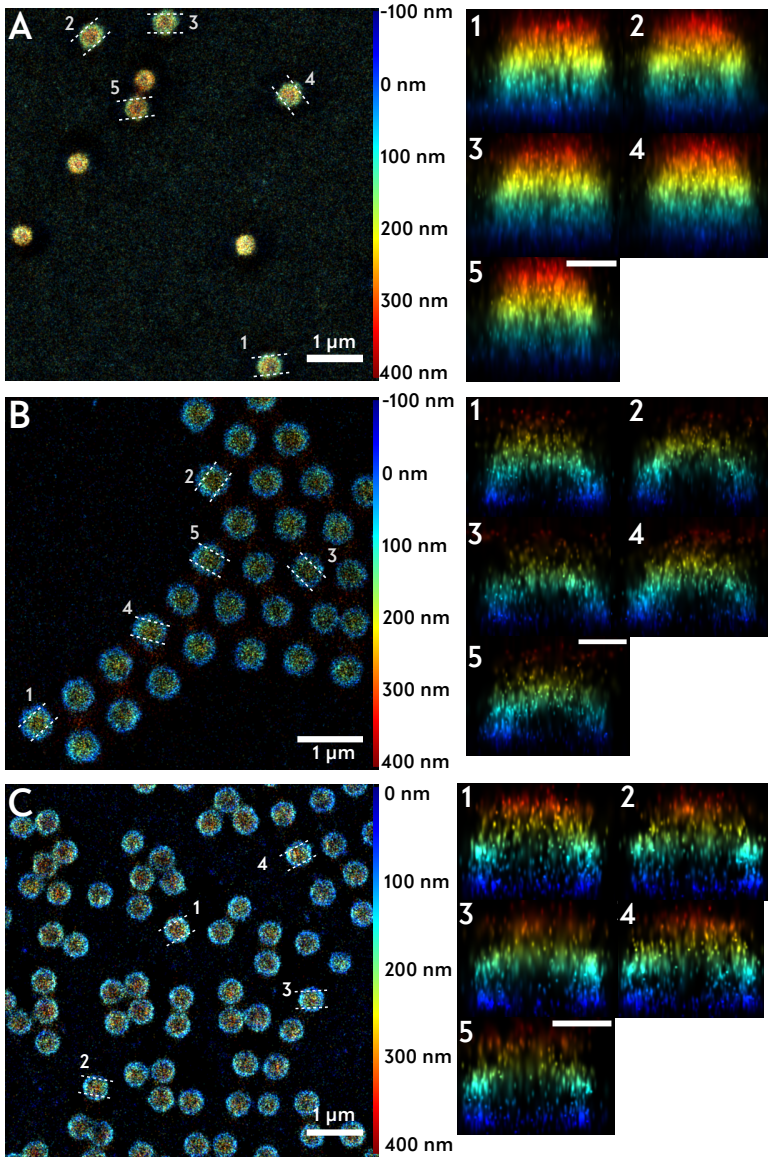

Figure 5.7.: In figure **A** to **C** the highlighted areas from figure 5.2 are represented with a height dependent color coding. The 3D reconstruction is based a on astigmatism shaped PSF of single fluorescent emitters. The subsequent single molecule fitting was done with SMAP. From each image five microgels were selected and a xz-projection of the area with the dashed lines is displayed. Scale bar 200 nm.

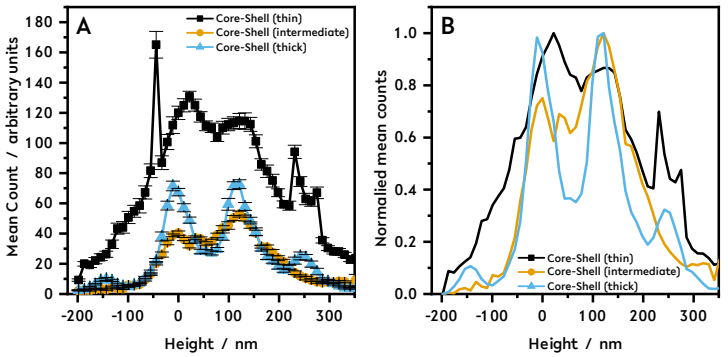

Figure 5.8.: Mean counts vs height of 20 microgels (black=thin shell, yellow=middle shell and blue=thick shell). A 300 nm thick line plot was used to get an averaged count through the whole microgel. The error bars represent the error of the mean. In **B** the graph is normalized to values between zero and one. The data point at -44 nm was excluded from the normalization.

only NNPAM is swollen. For higher shell densities (see figure 5.6, intermediate: yellow circle, thick: blue triangle) almost no dye localization in the core region is observed. This can also be resolved by 3D *d*STORM by the earlier mentioned xz-projections shown in figure 5.7 **B** 1 to 5 for the "intermediate" shell microgel and in figure 5.7 **C** 1 to 5 for the "thick" shell microgel. Interestingly the change from the intermediate to the thick shell around the core alters the localization density only slightly (compare figure 5.6 **A** and **B**). Therefore, the differences between the shown xz-projections through the core are hard to recognize. To make these slight differences visible a line plot through the xz-projections is done. This can be automatically achieved within SMAP. The resulting intensity distribution based on the localization across the axial direction is visualized in figure 5.8. In total 20 microgels for each shell-thickness were used to determine a mean count along the optical axis. For a better visualization the outliner at ~ 150 nm is removed for the normalization of the data. From the evaluated data a higher localization number for the microgel with the thin shell can be seen as well. A small decrease in the intensity can be observed around a height of 75 nm. This could be an indicator for the center of the core material. The source of the shoulder between 230 and 275 nm is unclear, but might be related to artifacts because for the microgel with the thick shell a similar bump at the same axial position and additional at -150 nm is observed. Around the axial position of 60 nm the microgel with a thick shell shows a clear decrease in the mean count along the axial position. This might be related to the increased density of the core by the interpenetrated network. The intensity in the core region is negligibly small due to the fact that the core can no

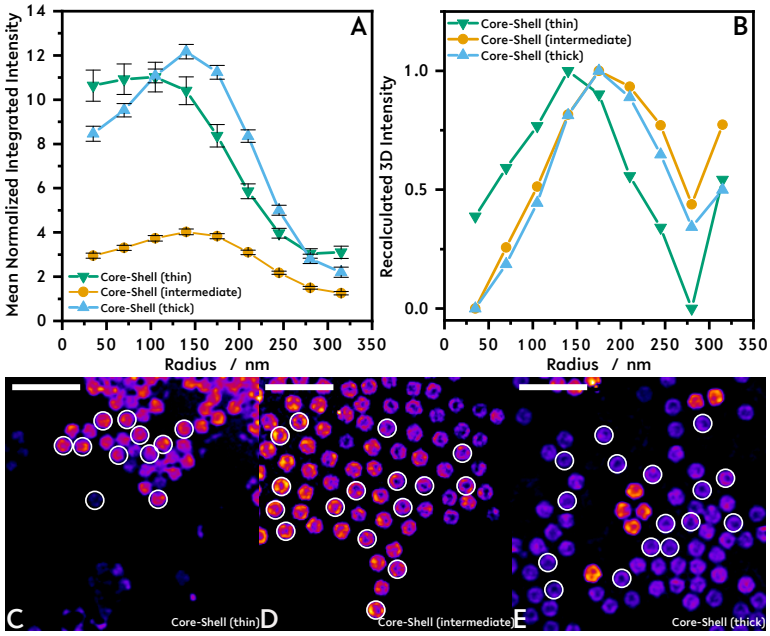

Figure 5.9.: To verify the results from single molecule localization experiments, as shown in figure 5.6, structured illumination microscopy images of the same core-shell microgels were taken at a temperature of 17°C and below, to preserve the swollen state of the microgels. In **A** the mean normalized integrated intensity is plotted against the microgel radius. For this, the white marked microgels in **C**, **D** and **E** were selected by hand. The results were recalculated with the presented 3D recalculation scheme and the results are shown in **B**. In comparison, the microgels with intermediate and thick shell are showing a slope with increasing signal intensity up to a radial distance of 150 nm. This can also be seen in the number of localizations in the SMLM experiments. Scale bar 2μm.

longer be reached for R6G fluorophores. Based on SANS results this observation leads to the conclusion that due to the strong interpenetration, the particles are rather dense inside and the dye only penetrates the shell in these microgels [302].

The various core-shell microgel systems are also imaged using the SIM process. The improvement of the resolution with SIM is sufficient to confirm the results of SMLM, where the "intermediate" and the "thick" shell have smaller localization densities in the microgel core (diameter circa 300 nm). The lower number of localizations should also lead to a lower intensity in this specific range. The 2D normalized integrated intensity of the white-marked microgels reconstructed with

SIM is shown in Figure 5.9 **A**. The recalculation for 3D intensities was performed using the same calculation methods as for the SMLM data. The only difference is that the ring size must be set to 35 nm. Compared to the localization densities, the SIM data show a stronger signal for the core-shell microgels with a thick shell. Referring to the 3D densities shown in the figure 5.6 **B**, the 3D intensities shown in the figure, 5.9 **B** show a similar shape, but with fewer details due to the limited resolution and different approach to generating normalized integrated intensities.

5.5. Conclusion

In chapter 3 "Super-Resolution Optical Microscopy resolves Network Morphology of Smart Colloidal Microgels" a quantitative method to characterize the network density of NIPAM based microgels (*N*-isopropylacrylamide) by means of localization of freely diffusing probes [276] is introduced. The method has reproduced the established density distribution of a fuzzy sphere [73] for well studied NIPAM microgels with 5 mol% *N*,*N'*-methylenebisacrylamide (BIS) as cross-linker. Furthermore, for highly crosslinked NIPAM microgels with 7.5 and 10 mol% BIS, respectively, a deviation from the fuzzy sphere model could be found and a correction with an additional linear term was proposed. In the present chapter it is shown, that this method can also be applied to core-shell microgel particles made of two different acrylamides.

In this chapter the internal morphology of PNIPMAM core-only microgels and PNIPMAM-PNNPAM core-shell microgels are studied by super-resolution fluorescence microscopy. Core-shell systems are investigated with three different PNNPAM shell thicknesses. As fluorescent dye for *d*STORM measurement freely diffusing Rhodamine 6G was used. Therefore, the localization density inside the particles can be determined. For initial core microgel particles the fluorescent dye diffuses into the particles and the fluorophores are located in the microgel particles. For core-shell particles the NNPAM shell material interpenetrates the PNIPMAM core. The interpenetration results in a higher localization density due to an increased interaction between the fluorophores and the polymer network. For thicker shells a higher degree of interpenetration can be observed as almost no localizations are found in the core of the core-shell particles. The reason could be either an increase of the network density by the penetration of the shell polymer into the core, which avoids the diffusion of the fluorophores into the polymer network, or the formation of a diffusion barrier. The thicker shell also inhibits the diffusion of the fluorophores into the core, such that just a small amount of fluorophores can be found in the core region. Furthermore, the interpenetration of the shell material into the core is high enough that dye molecules in a size range of R6G molecules are not able to reach the core. This work has potential implications for studies, where microgels are loaded with small molecules, e.g. in drug delivery. Moreover,

it shows that the use of freely diffusing probe molecules is promising for a broader range of soft colloidal systems.

6. Photoactivation localization microscopy of cardiomyopathy associated plakophilin-2 mutants

Summary

Arrhythmogenic right ventricular cardiomyopathy (ARVC) is a genetic heart disease characterized by ventricular arrhythmia, dilation of the right ventricle and fibro-fatty replacement of the myocardium. ARVC is mainly caused by mutations in genes encoding desmosomal proteins. Desmosomes are cell-cell connections which are linked to the intermediate filament system contributing to the mechanical stabilization of cardiomyocytes. One of the prominent ARVC genes is PKP2, encoding plakophilin-2. Most ARVC associated PKP2 mutations cause premature termination codons leading to a putative truncation of the protein. Plakophilin-2 is a linker protein of the Armadillo family and connects desmosomal cadherins with desmoplakin. However, the detailed cellular assembly of the desmosomal proteins is incompletely understood. Plakophilin-2 consists of a head, central Armadillo repeats and a short tail domain. Here, the generated series of truncation mutations was investigated in transfected human embryonic kidney cells (HEK293T) via localizing mEosFP thermo, when it is switched from its green fluorescent form to the orange fluorescenct form by irradiation with violet light (405 nm). The process of photoactivation or photoconvertion of individual fluorescent proteins with a subsequent localizations step is known as photoactivation localization microscopy (PALM). Wild-type plakophilin-2 is localized at the plasma membrane. Deletion of the tail domain has no obvious effect on membrane localization of plakophilin-2. However, different mutants without the Armadillo repeats lose their membrane localization. The study indicates that the desmosomal assembly is disturbed by truncation mutations of plakophilin-2, which might have relevance for the molecular and cellular understanding of ARVC.

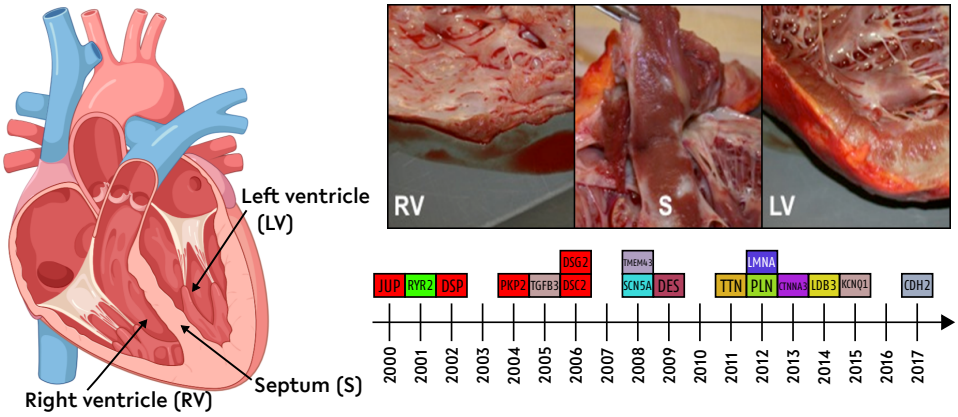

Figure 6.1.: The sketch on the left hand side shows a cross-section of the human heart. Areas of the heart affected by right ventricular arrythmogenic cardiomyopathy (ARVC) are highlighted with arrows(right ventricle (RV), septum (S) and left ventricle (LV)). In a healthy human heart the muscle appears dark red. In case of the here investigated genetic heart disease, ARVC, a fibro-fatty replacement of the heart muscle appears. This can be seen in the photographs on the right hand side. In rare cases of this disease the fibro-fatty replacement can also be found on the septum (S) and in the left ventricle (LV). The corresponding and potentially mutated genes are listed with year of the finding. The five genes found by 90% of all ARVC patients are highlighted in red, namely plakoglobin (JUP), desmoplakin (DSP), plakophilin-2 (PKP2), desmocollin-2 (DSC2) and desmoglein-2 (DSG2).

6.1. Introduction

First observation of an arrhythmogenic right ventricular cardiomyopathy (ARVC) were probably made by Giovanni Maria Lancisi in the 18th century. He studied a family for over four generations, where he found that members of the family suffered from dilatation, aneurysms, palpitations and arrhythmias leading to spontaneous death. Nowadays it is known that in case of an ARVC the heart muscle cells are losing the ability to adhere in a sufficient manner and the yielding space is filled by a repair mechanism with a fibro-fatty tissue replacement. This can be seen in figure 6.1 (RV) on the upper right side by the white tissue in the right ventricle. In rare cases additionally to the right ventricle the septum (S) and the left ventricle (LV) are affected. In the last 20 years more than 400 different mutations were found in 17 different genes (see timeline figure 6.1). Interestingly approximate 90% of all ARVC cases are caused in a mutation in the genes of plakophilin-2 (PKP2), desmoplakin (DSP), desmoglein-2 (DSG2), desmocollin-2 (DSC2) and

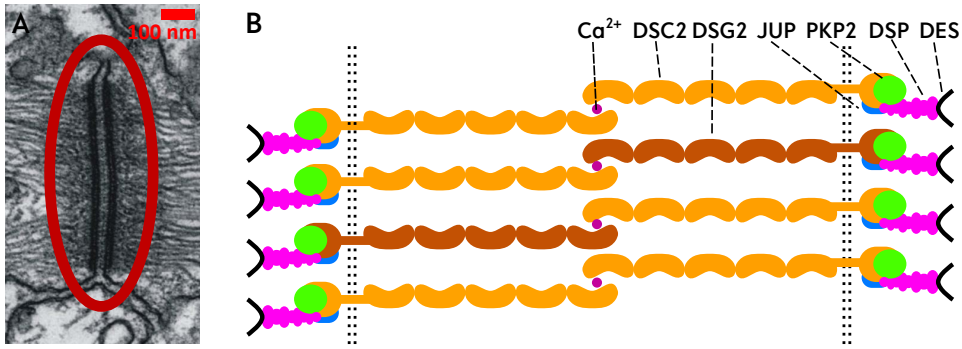

Figure 6.2.: A shows a scanning electron micrograph of an intercallated disk (ICD), which is formed between two heart muscle cells. **B** depicts a scheme of the localized proteins within the red highlighted area forming the desmosomes. The ICD fulfills important functions for the contraction of the heart muscle. It is possible to distinguish between an intercellular and an intracellular region. Within the cell the proteins desmin (DES), desmoplakin (DSP), plakoglobin (JUP) and plakophilin-2 (PKP2) are located. Desmin has the function as an anchoring point for the cytoskeleton. On the other hand, plakoglobin and plakophilin-2 have the function at the cell membrane to bind the extracellular cadherin domains (desmocollin-2 (DSC2) and desmoglein-2 (DSG2)). Scanning electron image of an ICD adapted from [111].

plakoglobin (JUP) [182, 186]. The pathomechanism of the mutations are unknown, which prohibits a molecular therapy of ARVC. For a normal heart function a synchronous mechanical and electrical communication between single cardiomyocytes is necessary to ensure coordinated contraction and excitation. The extracellular part of the desmosomes accommodates the DSG2 and DSC2, which can be seen in figure 6.2 on the right hand side. These cadherins are Ca^{2+}-dependent adhesion molecules and interact with adjacent cardiomyocytes over the specific proteins desmoglein-2 and desmocollin-2. These two proteins have in addition to the intercellular part an intracellular complex, which is necessary to anchor the armadillo repeat proteins JUP and PKP2. Within this anchor at the cell membrane desmoplakin and the desmin are located and have the role to anchor the actin as a part of cytoskeleton. Therefore, this protein complex plays a mayor role for the mechanical stability of cardiomyocytes. The significance of wild type and mutated types of the formed plakophilin-2 is of great interest in this thesis. The unaltered wild type of plakophilin-2 consists of a head, a tail domain and nine armadillo repeats in between. Among the fifth and sixth repeat the palmitaylation site is located. The function of the palmitoylation site is depending on the location of the protein. For peripheral membrane proteins this specific site can promote or specify membrane

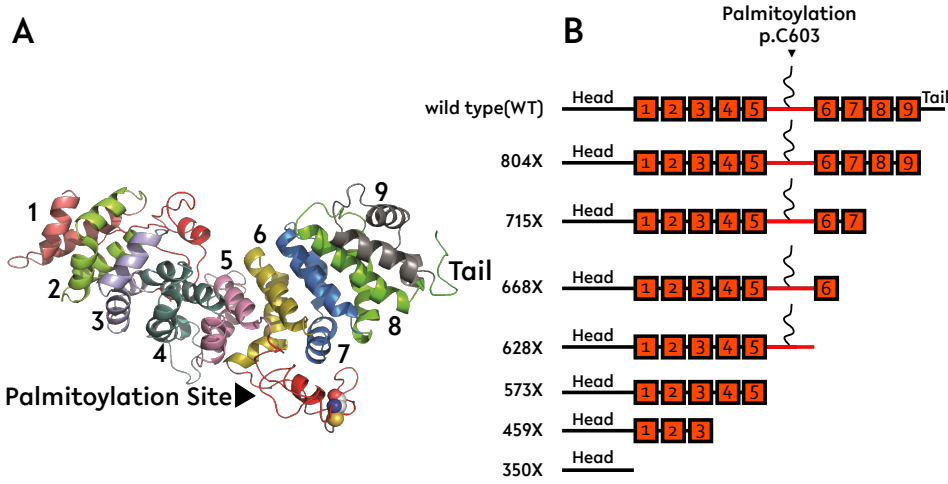

Figure 6.3.: **A** shows a model of the molecular structure of PKP2. The numbers indicate the different armadillo repeats of the protein. These repeats are surrounded by a head and a tail domain. A palmitoylation site can be found in between. The function of the palmitoylation site depends on the location, where the site is found. **B** schematically shows PKP2 and the different truncation mutations. Here the scheme on the top is the wild type with its nine armadillo repeats, the head and tail domain and the palimitoylation site.

interactions. For integral membrane proteins the functions of palmitoylation sites are unclear [58]. Due to the interaction between the two cadherin proteins with PKP2, it is likely that the underlying function for the vesicle transport is diminished. At first the focus is on the investigation of the PKP2 localization within the cell for different truncations (see figure 6.3). Referring to this, seven truncations were investigated and compared regarding to the wild type of the protein. For the study human embryonic kidney cells (HEK293T) were cultivated and transfected with a plasmid encoding PKP2 fused to mEosFP thermo (see table 2.1) for visualization purposes. With a laser source emitting light around a wavelength 400 nm, it is possible to convert the absorption and emission characteristics of mEosFP thermo. Via spectral filtering the proteins with a converted fluorescence can be distinguished from the unaltered proteins. This can be used to generate a sparse subset of fluorescent proteins emitting in the red shifted regime. The subsequent localization step generates an improved lateral and axial resolution in comparison to standard widefield fluorescence microscopy. Of particular interest for the investigation is the interplay between the cadherin proteins and PKP2 in cardiomyocytes. A main problem is the strong scattering of the signal through the cells. A possible

solution might be the excitation with TIR to restrict the fluorescence signal to a few hundred nanometers over the coverslip. The fluorescence distribution between the different truncations would not be distinguishable, since the cell membrane appears as a continuous area, such as for the ubiquitous distributions of the truncated PKP2 types (compare figure 6.5). Therefore, HILO illumination was chosen to create a thin "lightsheet" near the coverslip. Images were taken within the cell, where the cell membrane close to the coverslip was out of focus.

6.2. Experimental Section

6.2.1. Experimental setup

In comparison to standard *d*STORM imaging, the switching rates were controlled by the laser intensity of the 405 nm laser (Coherent OBIS 405 nm LX FP 50 mW, Coherent Inc., USA) and the frequency with a certain duty cycle. The laser was triggered with a frequency generator (Hameg HMF2550, Rhode & Schwarz, Germany) applying a rectangular voltage to the analog input of the laser control-box. To achieve a sufficient sparse fluorescent signal from the photoconverted fluorescent proteins 0.1 V pulses with a duration of 10 ms were generated with a frequency of 5 Hz. To decrease the laser intensity a neutral density filter was inserted into the illumination path. The final laser power in front of the objective lens was 90 to 95 μW resulting in $\approx 4.5 \frac{\mathrm{W}}{\mathrm{cm}^2}$ per pulse. The read out of the photoconverted mEos FP thermo was performed by an argon krypton laser (70C-Spectrum, Coherent Inc., USA). The 568 nm line was selected with an acousto-optic tunable filter (AOTF) (OTFnC-VIS-TN, A-AOpto Electronic, France) and the remaining residual laser light from other wavelengths was filtered out with a narrow excitation filter (568/10 X, AHF, Germany). A spatial overlap in the sample between the laser of the argon krypton laser and the laser diode was achieved by a dichroic mirror (Di01-R405, Semrock, USA). The used read out laser power density was approximately $5 \frac{\mathrm{kW}}{\mathrm{cm}^2}$, with a laser power of 110 mW in front of the objective lens. Both laser beams were reflected by a quadband diochroic mirror (Di03-R405/488/561/635, Semrock, USA) towards the objective lens, where both were focused on the back focal plane, to get a homogeneous illumination within the field of view. The typical decrease in intensity to the edges, according to the Gaussian intensity profile of the laser beam, could be observed. With this high power density the photoconverted proteins were photobleached after the read out. Therefore, it is important to keep the number of photoconverted fluorescent proteins low for successful SMLM.

The transmitted fluorescence was detected with an industry grade CMOS camera (IDS UI-3270CP Rev.2, IDS, Germany). According to the small physical pixel size of 3.45 μm an additional telescope with a 300 mm and a 160 mm achromatic lenses were used to adjust the projected pixel size to 109 $\frac{\mathrm{nm}}{\mathrm{pixel}}$. In the parallel beam path

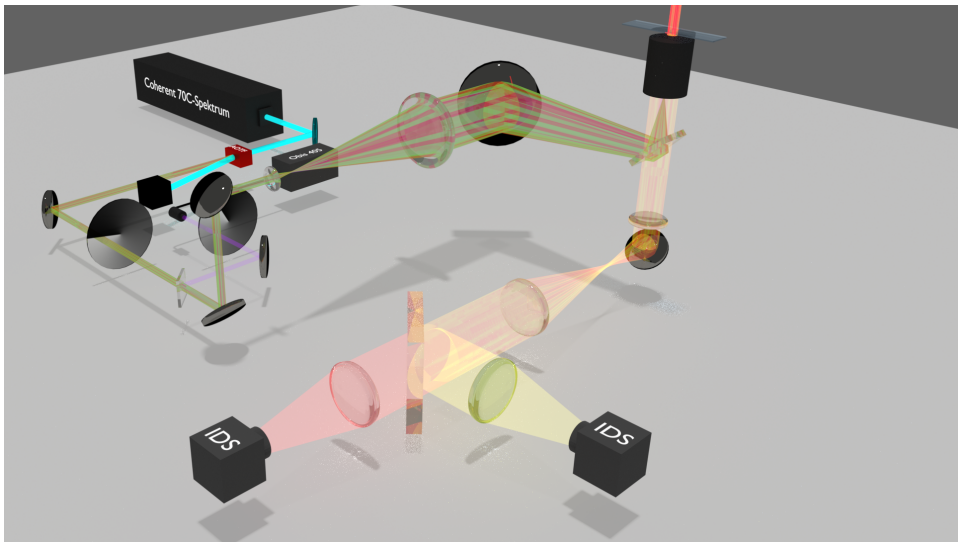

Figure 6.4.: Schematic 3D rendered image of the used setup without specific excitation, emission filter and the cylindrical lens for 3D imaging. Following the laser source, the argon krypton laser, a specific laser line can be chosen by the acousto-optic tunable filter (AOTF) (small red box). A fine tuning of the laser intensity can be done by either the AOTF or the gradient neutral density wheels. The 405 nm pigtailed laser is coupled into the setup via a dichroic mirror. Before the second dichroic mirror reflects the laser towards the objective lens, a telescope expands the laser beams and focuses them on the back focal plane of the objective lens. Emitted light is collected by the same objective lens and transmitted through the dichroic mirror. For the dual-color setup a 300 mm lens is placed in the distance equal to its focal length, with respect to the primary image position. In the parallel beam path a dichroic mirror is placed to split the image into two spectrals path for wavelengths shorter 650 nm and longer than 650 nm. The images are displayed on the two cameras using two separate 160 mm lenses.

two emission filters were inserted. On the one hand, a 470 nm long pass to suppress the 405 nm laser light, which is needed for the photoconversion, and a 568 nm long pass (LP02-568RU, Semrock, USA) to block the remaining excitation light. 3D imaging was enabled by inserting a cylindrical lens in the detection path. Here, the same procedure can be followed as described in the subsection 4.2.2 about 3D calibration for microgels.

6.2.2. Image acquisition and data reconstruction

In total 20000 frames were recorded with an exposure time of 40 ms for the reconstruction of a super-resolution image. Camera control and image acquisition were realized with the open-source software Micro-Manager (version 1.4.22 [195]). Reconstruction was done with the ImageJ plugin ThunderSTORM [197, 286]. For the data sets of the wild type PKP2 and the first truncation mutation, where the tail domain was removed, it was possible to post process the data with a drift correction based on cross-correlation. For the other data sets the cross-correlation method failed due to the missing structures to correlate with. Therefore, a further post processing of the data was neglected. The final reconstructed images were rendered with a five times magnification and the method of averaged shifted histograms [139], where a lateral shift of two, was applied. For a better visualization the look up table orange hot was utilized to the gray scale image.

6.2.3. Data analysis

To compare the different truncation mutations of PKP2, the ratio of two localization densities with respect to localizations within the cell and on the cell membrane was calculated. For the untruncated wild type and the first truncation mutation, where only the tail domain was removed, the dense fluorescence at the cell membrane allows the use ImageJs integrated functions to recognize the cell membrane and generate automatically a region of interest. The first step was a conversion from 32 bit gray scale to 8 bit gray scale with the subsequent use of the morphology tool box. The used setting was 3.5 pixel radius for a circle. Every single pixel in the image was dilated with this circle, which makes it easier to automatically find the cell membrane on the basis of its fluorescence protein localizations. Using the wand tool, the outside of cells could be selected due to the high contrast based on the black background. By inverting the selection the cell was selected. A shrinking of the selection by 400 nm and a following formation of a band selection with a width of 400 nm was done to select only the region of the cell membrane. With the measure function the integrated intensity, the area of the band selection and the inner part of the selected were measured.

For the other truncation mutations, where a ubiquitous distribution of the fluorescence signal was found, the method described before cannot be used because the cell membrane appeared very spotty and therefore difficult to select. Especially for the dense cell culture in which the cells grew on top of each other. Therefore, the outermost parts of the cells were selected based on the reconstructed image with a polygon selection. The straight connections between the points were smoothed with a spline. Then the same process was performed as described above.

6.3. Results and discussion

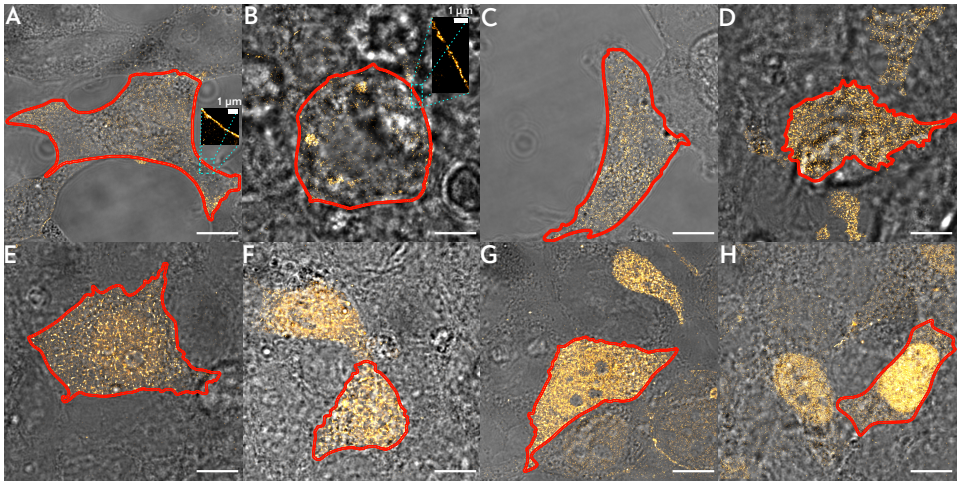

Figure 6.5.: From **A** to **H** exemplary images for each investigated truncation mutation are shown in an overlay of the white light image (gray) with the reconstructed single molecule localization image (orange). **A** and **B** are corresponding to the wild type and the first truncation mutation with the removed tail domain. The red band indicates the membrane area where the localization density is measured and compared in respect to the inside of the cell. Following from **C** to **H** different numbers of armadillo repeats are removed. The scheme for the different types of PKP2 can be seen in figure 6.3, where the truncations from top to bottom can be seen in the images **A** to **H**. Scale bar 10μm.

The results based on the precise localization of the truncated PKP2 fused to mEosFP thermo supports earlier findings that ARVC is related to mutations in PKP2 [118, 132]. The first finding is that for all types of the here investigated proteins, the protein is expressed in transfected cells, which can be seen by the detected fluorescence signal (compare figure 6.5). Based on the localization microscopy data it could be shown that the wild type of plakophilin-2 accumulates at the cell membrane of HEK293T cells. In addition to the accumulation at the cell membrane a fluorescence signal can be found in the nucleoplasm, which is in good agreement with fluorescence images by Stefan Rickelt [172]. The first truncation (804X) results in a mutated PKP2 expressing plakophilin-2 without the tail domain. This mutated protein is still able to show a higher accumulation at the cell membrane in relation to the cytoplasm and nucleus, but with a lower ratio between the localization densities in comparison to the wild type. With respect

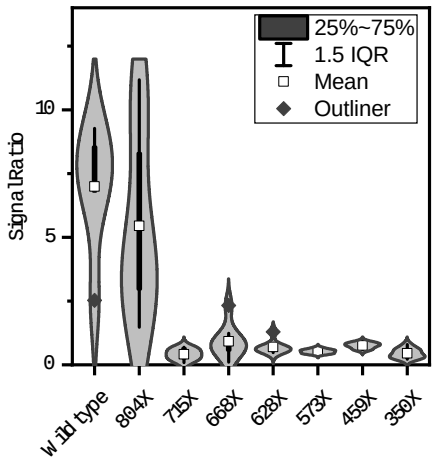

Figure 6.6.: The violin plot indicates the ratio between the localization density at the cell membrane and within the cell. For a single cell this ratio is calculated as described in the data analysis section. The mean is calculated over more than five cells with error bars indicating the standard error of the mean. Within the violin plot the thin bar is the 1.5 times the interquartile range. The outliners of the data set are represented by the light gray data points. By removing the last two armadillo repeats the strong accumulation at the cell membrane vanishes and the fluorescent labeled protein is distributed all over the cell. This could be indicated by a localization ratio of one or below.

to the error bars, the significance is not high enough to state that there is an obvious change in the localization density between the wild type and the tailless truncation. The mutations with at least two or more removed armadillo repeats are showing a similar ubiquitous distribution of the localizations of the photoconverted mEosFP thermo. This can be seen in the violin plot in figure 6.6 for the mutations with missing armadillo repeats. The corresponding mutations are 715X and following with a smaller number (see figure 6.3). An interesting point is that additional to the localization at the cell membrane, PKP2 can be found endogenously formed in the nucleoplasm [172]. From the reconstructed images mainly no additional information is gained, which can also be collected e.g. by conventional confocal microscopy, which is used in most of the studies[77]. But it was possible to confirm that a mutation of PKP2 can lead to a functional loss of the protein, which is shown by the ubiquitous distribution within the cell, which is an indicator that the protein cannot be integrated in the cell membrane anymore. A second indicator for the loss of protein functionality would be an interaction with the desmosomal

protein desmoplakin (DSP). To investigate a change in expression rate for different mutations in comparison to the wild type, the widely used method of western blots can be used to calculate relative numbers of expressed proteins [118, 132]. Another mechanism which can be activated due to truncated proteins, is an activation of the unfolded protein response, in case that a mutation generates miss-folded proteins. A cell response is therefore an increased synthesis of chaperone for a correct protein folding. When this status is held over a longer time the unfolded protein response will initiate apoptosis [142, 144]. The mechanism of cell induced death seems to be only observable for plakophilin-2. It is known for desmoglein-2 that mutated types are also distributed within the cytoplasm, but are still correctly folded and do not initiate apoptosis [93, 154]. All in all, desmosomal proteins are important for cell stability and protect heart muscle cells, reducing stress from stretching, movement and pressure [65, 76, 104, 112]. Therefore, the interplay between the five different desmosomal proteins DSG2, DSC2, JUP, PKP2 and DSP is crucial for the signaling and the integrity of cardiomyocytes. By altering a single protein the whole complex is disturbed in its function.

6.4. Conclusion

With this work earlier results about truncation mutations in PKP2, leading to a delocalized plakophillin-2 within the cell, are supported. Typically, the wild type of plakophilin-2 is located at the cell membrane and the nucleoplasm. In case of an truncated PKP2 gene with the deletion of at least two armadillo repeats the protein is found delocalized in the cell's cytoplasm and the specific localization at the outer cell membrane disappears.

The application of SMLM for the verification of earlier findings was not necessary, but shows that photoconvertable fluorescent proteins can be used to localize single proteins with a higher lateral precision than e.g. confocal laser scanning microscopes. This method can be used for efficient molecule counting, which is of interest to compare the number of expressed proteins in comparison to a control. This quantitative counting can be of great interest because there is still the possibility that mutations are not causing ARVC, but lead to a decreased number of proteins in the cell membrane. A consequence might be a weaker cell to cell adhesion, which would cause a weaker heart muscle. The benefit of high lateral resolution and improved axial resolution by the usage of PSF shaping methods can be a very useful tool to reveal the interaction of desmosomal proteins, in particular with the usage of a dual color approach. Here the dependence of the five proteins (DSG2, DSC2, JUP, PKP2 and DSP) can be investigated. Therefore, it will be interesting which combination of mutations in different genes will still result in a functional desmosomal complex.

The cooperation with the Herz- und Diabeteszentrum in Bad Oeynhausen allows

a further possibility with investigation of heart slices from explanted hearts from patients showing the specific mutations. This makes it possible to verify the results obtained from experiments in cell culture with relevant samples. The problem with heart muscles is the strong scattering of laser light and the fluorescence. In order to investigate the interaction of desmosomal proteins, a 3D super-resolution image is advantageous or even necessary. Therefore, adaptive optics can be used to compensate for image distortion and improve the axial range in which SMLM can be used with various PSF models [274].

7. Probing magnetic fields with super-resolved fluorescence microscopy

This chapter is published in parts as a peer reviewed comment.
Stephan Bergmann, Viola Mönkemöller and Thomas Huser Comment on "Magnetic-field-enabled resolution enhancement in super-resolution imaging" by M. Zhang et al.,Physical Chemistry Chemical Physics, 2015,17, 6722–6727 Physical Chemistry Chemical Physics 19, 4887 (2017))

Summary

Certain fluorophores, in particular those that can undergo photoinduced radical pair reactions, are known to exhibit a magnetic field dependent fluorescence summarized in the term magnetic field effect (MFE). In the experiments carried out, attempts were made to reproduce the results previously shown on magnetic field enhanced fluorescence for commonly used organic dyes with a high quantum yield suitable for single molecule localization microscopy. The result is that the enhanced fluorescence is based on the additional reflected fluorescence from the magnet's surface towards the detector. In the following, a DNA-based approach is shown which can be used for the detection of magnetic fields. Therefore, the chirality of molecules like DNA or peptides can be used as a spin-filter.

7.1. Introduction

Certain fluorophores, in particular those that can undergo photoinduced radical pair reactions [54] are known to exhibit a magnetic field dependent fluorescence summarized in the term magnetic field effect (MFE). In a publication by Zhang et al. [229] standard organic dyes such as the often in *d*STORM experiments used Alexa Fluor 647, Alexa Fluor 532, Cy3 and Cy5 are analyzed on their behavior in weak magnetic fields with the outcome that an enhanced fluorescence was observed depicted by a higher number of emitted photons.

Table 7.1.: List of organic dyes with their respective concentration and solvent as used in this experiment.

Dye	Concentration nM	Solvent
Alexa Fluor 647 NHS Ester	10	Dimethylformamide
Alexa Fluor 532 NHS Ester	1	Dimethylformamide
Cy3	100	Water
Cy5	10	Dimethylformamide

Based on this results the idea is to probe magnetic surfaces by measuring the difference in emitted photons depending on the magnetization direction of the out of plane magnetization and ultimately to use single molecule localization microscopy (SMLM) to resolve single magnetic domains within the magnetic surface. Unfortunately it was not possible to gain any reproducible results. But it was found that the enhanced number of emitted photons in standard organic fluorophores is not a consequence of the MFE.

The findings are based on bulk experiments with low concentrated dye solutions in a fluorimeter with a standard 90° geometry and on quantitative evaluation of single molecule localizations from designed single molecule surfaces.

7.2. Experimental section

7.2.1. Fluorescence spectroscopy

The bulk experiments with low concentrated dye solutions were conducted in a commercial fluorimeter (Cary Eclipse, Varian (now Agilent), USA). Approximately 0.5 ml of the solution were placed in quartz cuvettes (108.002F-QS, Hellma, Germany) with 10 mm path length. The dye solutions with the final concentrations and the used solvents are shown in table 7.1. The applied settings for the fluorescence spectroscopy measurements are shown in table 7.2. To apply an external magnetic field to the dye solutions a cubic NdFeB magnet (Webcraft GmbH, Germany, edge length 10 mm) was placed in opposite direction to the detector. The magnetic flux density is controlled by changing the distance between the quartz cuvette and the magnet. Since only a single cubic magnet was used, an inhomogeneous field is created in which the flux density is measured with a magnetometer (13610-93, Phywe, Germany), approximately at the position in the middle of the cuvette. To reproduce the results of the discussed paper similar magnetic flux densities (8 mT) were used and in addition to this stronger fluxes (50 mT) were evaluated in this

Table 7.2.: Fluorimeter settings for bulk measurements of the magnetic field effect on the fluorescence spectra of organic dyes.

Dye	Excitation wavelength	Excitation slit	Emission slit	Scan rate	Data interval	Averaging time	Excitation filter	Emission filter	PMT voltage
	nm	nm	nm	nm/min	nm	s			V
Alexa Fluor 647 NHS Ester	650	10	10	600	1	0.1	Auto	Open	Medium
Alexa Fluor 532 NHS Ester	532	10	10	600	1	0.1	Auto	Open	Medium
Cy3	520	10	10	600	1	0.1	Auto	Open	Medium
Cy5	649	10	10	600	1	0.1	Auto	Open	Medium

part.

To prove the MFE, five different conditions during the fluorescence spectroscopy measurements were achieved by placing the magnet, a black cardboard and a mirror in the following settings. The spectrometer was used in the standard 90° configuration, this means that the excitation beam is perpendicular to the direction in which where the fluorescence is collected.

1. Reference measurements of the dyes emission spectra without magnetic field (black curves figure 7.1)

2. Fluorescence spectra with magnetic flux density of $\sim$ 50 mT with an additional black cardboard between magnet and cuvette to avoid an increased fluorescence by reflected fluorescence light towards the detector (yellow curves figure 7.1)

3. The black cardboard is removed and emission spectra are again recorded with the same magnetic flux density of 50 mT (green curves figure 7.1)

4. Repeating the measurements with adjusted magnetic flux density to 8 mT and added the black cardboard again (light blue curves figure 7.1)

5. Replacing the magnet and the cardboard by a mirror directly behind the cuvette (dark blue curves figure 7.1)

6. Repeating the reference measurement (orange curves figure 7.1)

7.2.2. Single molecule localization microscopy

In addition to the fluorescence spectrum based measurements SMLM measurements were done with the most prominent organic dye Alexa Fluor 647. Therefore, a single molecule surface was prepared in advance (see Appendix A.5.1). The magnetic flux density of 8 mT was achieved by placing the NdFeB magnet at the matching distance. To avoid back reflection between the single molecule surface and the magnet a, black cardboard was placed. Before the start of the measurement VECTASHIELD, an Antifade Mounting Medium (H-1000, Vector Laboratories, United Kingdom) [188], was added to the surface. Five measurements were done (5000 frames, exposure time 20 ms, irradiance 1.2-1.4 $\frac{kW}{cm^2}$, total internal reflection fluorescence excitation (TIRF) using a 1.49 NA microscopy objective (APON 60x Oil TIRF, Olympus, Japan) at different locations on the single molecule surface.

7.2.3. Evaluation of single molecule localization data

The acquired image stacks with 5000 frames were analyzed by the ImageJ plugin ThunderSTORM [197] to localize single emitter in each frame. Localizations with a larger uncertainty than 20 nm were rejected. All remaining localizations with their number of emitted photons were histogrammed with bins of 200 photons. Normalization was done by calculation of the frequency percentage (see figure 7.2). Afterwards the difference between the frequency percentages was calculated and displayed in the inset of figure 7.2. The on-state lifetime of a single fluorophore was estimated by merging localizations with an uncertainty smaller than 20 nm in consecutive frames where a localization occurred within a distance of 100 nm. The number of frames in which the localization was detected was multiplied with the exposure time of 20 ms. The arithmetic mean and the standard deviation were calculated from all the localizations thus grouped.

7.3. Results and discussion

In the article "Magnetic-field-enabled resolution enhancement in super-resolution imaging." by Zhang et al. [229] an increased fluorescence emission of organic dyes suitable for super-resolution imaging in the presence of a weak magnetic field (8 mT) is reported. To validate that this effect is indeed a MFE, the authors performed bulk and single molecule experiments and recorded fluorescence emission rates, emission spectra, and emission intensity. Based on photon counting by single molecule localization experiments the total number of photons was measured to show an increase in the emitted number of photons per localization in the presence of a magnetic field. A signal increase of approximately 20% for several organic fluorophores, such as Alexa Fluor 647, Alexa Fluor 532, Cy3 and Cy5 was reported.

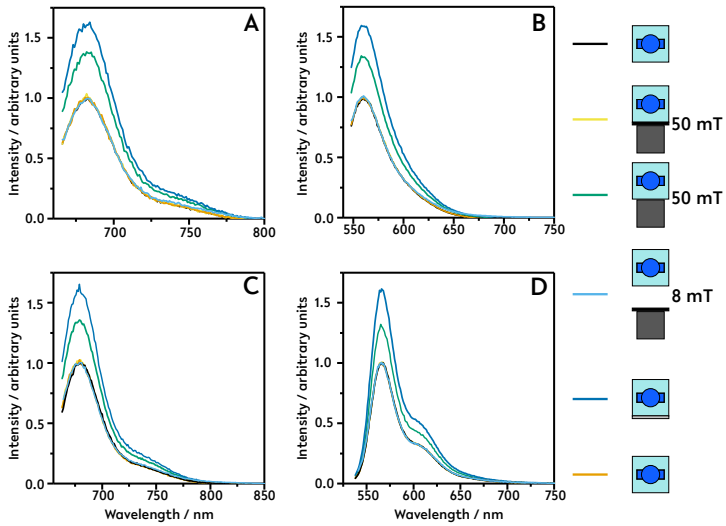

Figure 7.1.: Emission spectra of Alexa 647 (**A**), Alexa 532 (**B**), Cy5 (**C**) and Cy3 (**D**) under different conditions as indicated by the inset. The black curve shows the emission of the four organic dyes without magnetic field and serves as the reference measurement. For the yellow curve a magnet was placed behind the cuvette and covered with black cardboard to avoid reflection towards the detector. The light blue curve shows the emission where the magnet was covered and placed at a distance corresponding to a magnetic field strength of 8 mT. For the green curve the cardboard was removed and an enhancement of approximately 30% in the fluorescence, due to the reflection towards the detector, was measured for all 4 dyes. To show that the reflection is the reason for the increased signal intensity, a mirror with the same surface area like the magnet was placed behind the cuvette (dark blue curve). For all four dyes the signal intensity with the placed mirror was increased by approximately 60%. As final control (orange curve) a second measurement without magnetic field and mirror was performed to exclude photobleaching effects.

The MFE is typically attributed to the interaction between a magnetic field and a fluorophore, e.g. in fluorescent radical pair reactions [155]. A possible application of this effect was demonstrated by Lee et al. [217], who used a specialized magnetic field indicator, phenanthrene-$(CH_2)_{12} - O - (CH_2)_2 - N$,N – dimethylaniline for 3D magnetometry by two-photon fluorescence microscopy. In this case it is believed that small external magnetic fields (1-10 mT) lock the precession of the electrons to the field axis which leads to a preserved coherence and therefore to a partially suppressed intersystem crossing (ISC) to the triplet state. The result is an increased

fluorescence emission [149, 217]. For even larger magnetic fields ISC can also be enhanced, resulting in a reduced fluorescence. This, however, cannot explain the effect of external magnetic fields acting on regular, high quantum yield organic fluorophores, such as the ones used in [229].

A reproduction of the results reported in [229] was not possible, but it could be found that the enhanced fluorescence emission attributed to MFE could not be verified. Comparable bulk experiments show no noticeable change of fluorescence signal in the presence of a magnetic field (8 mT and strong field gradient between 50 mT and 90 mT in the fluorescence spectrometer). Bulk fluorescence emission spectra of the same fluorophores as used in [229] (see figure 7.1 **A** for Alexa Fluor 647, figure 7.1 **B** for Alexa Fluor 532, figure 7.1 **C** for Cy5 and Figure 7.1 **D** for Cy3) were recorded. The fluorophores were prepared from stock solution to a final concentration of 1-100 nM (see table 7.1) and approximately 0.5 ml was placed in quartz cuvettes (108.002F-QS, Hellma, Germany) with 10 mm path length.

These solutions were then measured in a fluorimeter (Varian, Cary Eclipse, settings see table 7.2) under five different conditions roughly described in the experimental section 7.2.1. In this easy to use experimental configuration it was found that no measurable MFE in fluorescence intensity was achievable for the dyes of the the cyanine (Cy3,Cy5 and Alexa Fluor 647) and the rhodamine class (Alexa Fluor 532). Bleaching effects could be excluded by performing a reference measurement at the beginning (see black curves figure 7.1) and as the last part of the experiment (see orange curves figure 7.1). As already briefly described, high magnetic flux densities could have the ability to reduce fluorescence by an increased transition probability (ISC) into the triplet state and thus even stronger red-shifted emissions occur, which was not considered here. This could not be observed for the investigated organic dyes within a magnetic flux density between 50 and 90 mT (yellow curves figure 7.1). Even the proposed magnetic flux density of 8 mT showed neither a fluorescence increasing nor a decreasing effect (light blue curves figure 7.1). As a consequence it was possible to show that the increased fluorescence arises due to the materials reflectivity placed behind the cuvette, namely the mirror or the not covered magnet. The discrepancy between the here found increase of the fluorescence of approximately 30% based on the reflectivity (see green curves figure 7.1) of the magnet and the proposed enhancement of roughly 20% by the MFE might be due to the distance between uncovered magnet and detector or different magnet geometries. That the condition of the reflective material plays a role is shown with the measured fluorescence increased by 60%, if a mirror was placed behind (see dark blue curves figure 7.1). In a second set of experiments SMLM is used to reproduce the data indicating magnetic field enhanced fluorescence. Here, a single molecule surface (Alexa 647, for sample preparation see A.5.1) was prepared to compare the number of emitted photons per localization in the presence and in the absence of a magnetic field. To prevent reflections from the magnet's

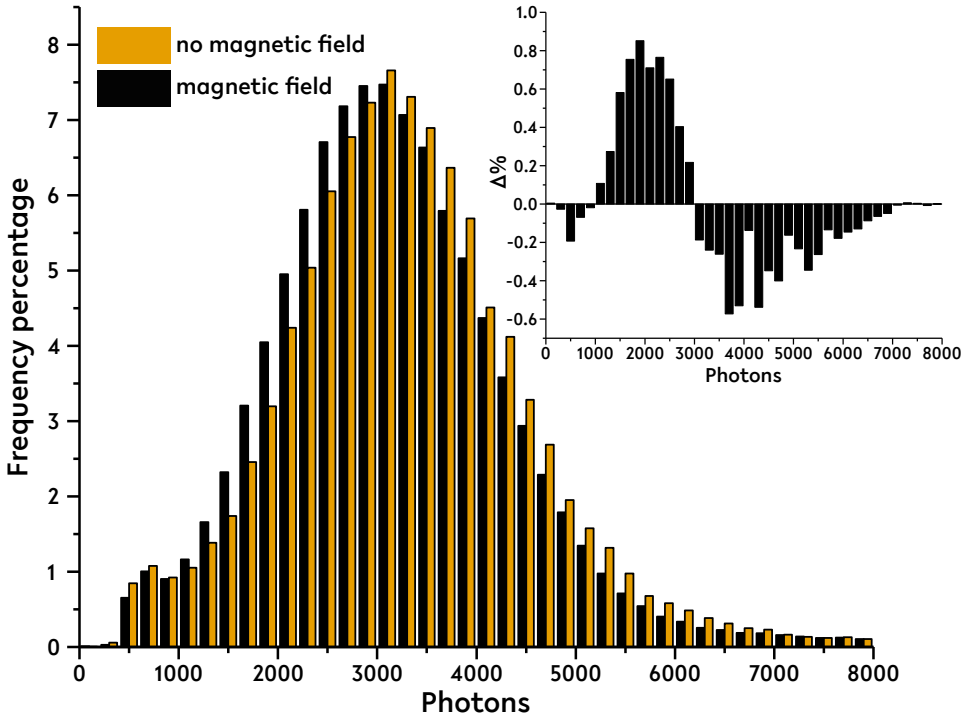

Figure 7.2.: Frequency percentage of emitted photons per frame of single Alexa Fluor 647 molecules obtained by direct Stochastical Optical Reconstruction Microscopy (*d*STORM) with (black) and without external magnetic field (orange). The inset shows the difference in the frequency percentage between measurements conducted with and without magnetic field.

surface, the magnet was again covered with black cardboard. Four measurements were conducted (5000 frames, exposure time 20 ms, irradiance 1.2-1.4 $\frac{kW}{cm^2}$, total internal reflection fluorescence excitation (TIRF) using a 1.49 NA objective lens (60x NA 1.49 ApoN, Olympus, Japan) at different locations on the single molecule surface. For the final evaluation, the data of all measurements was summed up (see table 7.3). The results, were shown as the frequency percentage of photons emitted per localization and the difference between the measurements with and without an external magnetic field is displayed in figure 7.2. The inset shows the difference in percentage of the photon frequency with and without magnetic field which is on a similar order of magnitude to that used by Zhang et al., but does not show any dependence on the magnetic field [229]. To check if there is an increased number of

Table 7.3.: Single molecule localizations were recorded at four different locations on the sample and by alternating the start position where the magnetic field was either applied or absent. The bold face font indicates which measurement was first conducted at the new location.

	Position 1	**Position 2**	**Position 3**	**Position 4**	**Sum**
localizations without magnetic field	**38905**	40350	**52455**	30028	161738
localization with magnetic field	33701	**52786**	37177	**43100**	166764

single molecule localizations when a magnetic field is applied, the single molecule surface was covered with VECTASHIELD Antifade Mounting Medium (H-1000, Vector Laboratories, United Kingdom) to minimize photobleaching effects. 1000 frames are recorded with and without applied magnetic field (magnet covered with black cardboard) at four different locations inside the sample. It is assumed that the number of fluorescent molecules changes only slightly by diffusion so that the results obtained from the same locations should be comparable. To exclude a decreased number of localizations due to photobleaching or long living dark-states, the order of the experiment between starting with or without an applied magnetic field (see table 7.3) was altered. The measurement shows that the number of localizations is strongly dependent on the order. It is clearly seen that in all measurements the highest number of localizations was consistently reconstructed from the very first measurement that was carried out regardless of the initial magnetic field strength. This implies that it is not possible to claim that an applied magnetic field increases the number of localizations in single molecule localization microscopy. In the paper by Zhang et al. it is not clearly stated whether the measurements were performed at the same location on the sample or whether positions were changed, since the labeling density and thus the number of molecules for different fields of view can vary. Additionally, the on-state life times were evaluated from the data by merging consecutive localizations in a distance of 100 nm after filtering out localizations with a larger uncertainty than 20 nm. It was found that no significant change in the on-state lifetime in the absence (78.09 ± 125.34ms) or the presence of a magnetic field (84.86 ± 199.80ms) occurs. The differences between the measured on-state lifetime and the results presented by Zhang et al. might be due to the use of different laser intensities, different components in the imaging buffer or the composition of the single molecule surface. The experiments showed

that an increase of fluorescence from fluorescent dyes, i.e. Alexa Fluor 647, Alexa Fluor 532, Cy3 and Cy5 in the presence of magnetic fields in the range of 50 to 90 mT could not be observed. A signal increase was indeed observed whenever the magnet responsible for the external field was not covered by absorbing black cardboard. The conclusion is therefore that the results shown in [229]are also due to reflections of the fluorescence signal by the surface of the magnet and not to MFE. A more reliable and controllable configuration would be to use Helmholtz coils to achieve an almost uniform magnetic field that can be controlled by the applied current. Nevertheless, a potential method to detect and measure the magnetization direction of small magnetic domains on the basis of SMLM will be introduced in the following.

7.4. Chiral induced spin selectivity effect

At the end of the 20th century Ron Naamann and coworkers [43] came up with an effect called chiral induced spin selectivity effect (CISS). The discovery that spin-polarized electrons have a preferred motion direction along a chiral molecule depending on the chirality. This behaviour is still of great interest to develop biosensors [255, 268], electrochemical water splitting methods [299] or spintronics [240, 241]. But the theoretical description is still an ongoing process and the origin has to be studied further. A qualitative understanding can be given based on the movement of an electron through the electrostatic potential. In case of a chiral molecule the appearing potential as well is chiral. While an electron is traveling with a velocity $\vec{v}$ through the chiral molecule then will feel the electrostatic potential $\vec{E}_{\text{chiral}}$. The generated magnetic field $\vec{B}$ is than described by

$$\vec{B} = \frac{\vec{v}}{c^2} \times \vec{E}_{\text{chiral}} \ , \tag{7.1}$$

with c the speed of light in vacuum. Due to the magnetic moment of the electron itself, the magnetic moments can interact with each other. Therefore, an energetic favorable alignment of the electron's spin can be found for the magnetic moment aligned parallel to the magnetic moment, generated by the movement through the electrostatic potential of the chiral molecule. The coupled electron spin to the magnetic field has additionally the effect, that the degenerated spin energy levels are split within the magnetic field. Different theoretical approaches have in common to calculate the spin-orbit interaction of the electron spin while moving through the electrostatic potential of the molecule. Their general finding is that a chiral potential causes a significant coupling between the electrons linear momentum and its spin [169]. A vivid example to estimate the strength of the spin-orbit coupling can be done with the assumption that the generated force is strong enough to confine the electron within the helical molecule. An easy to apply model is based

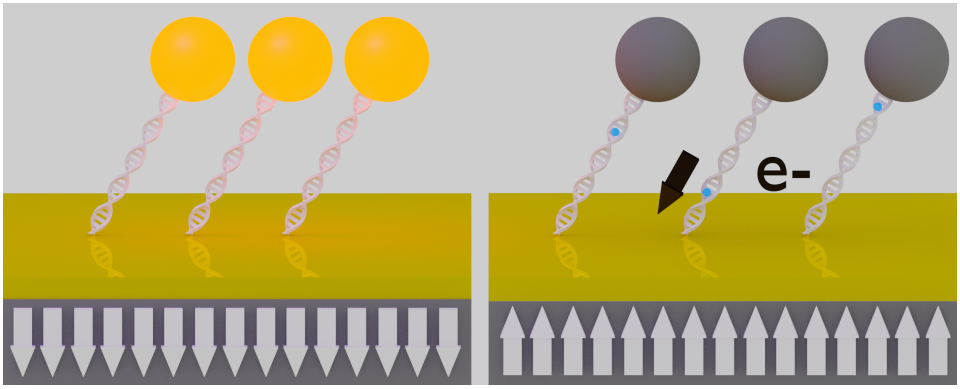

Figure 7.3.: Schematic drawing of a self assembled monolayer made of dsDNA on a gold surface with an underlying softferromagnetic multi-layer structure. On top a core-type cadmium tellurid is attached. The white arrows on the left and right hand side are indicating the out of plane magnetization direction. Depending on the handedness, the magnetization and electron spin, a tunneling or hopping through the dsDNA to the gold substrate is unlikely (left) or likely (right). In the case on the left hand side the electron is available to recombine with the "hole" in the quantum dot. Ultimately a photon is emitted by the recombination process and can therefore be a measure for the magnetization direction indicated by the Qdot's luminescence.

on the cyclotron motion, where the effective magnetic field is given by

$$|B_{\text{eff}}| = \frac{mv}{qr} \ , \tag{7.2}$$

with m, v, q describing the electron's mass, velocity and charge. In this model only the radius e of the helical molecule goes into the calculation for the effective magnetic field. The resulting spin-orbit-coupling is calculated with the effective magnetic field B_{eff} the Bohr magneton μ_B and g the g-factor for the electron.

$$H_{\text{SOC}} = \frac{g\mu_B}{2}|B_{\text{eff}}| = \frac{g\mu_B mv}{2qr} \tag{7.3}$$

Assuming a kinetic energy of 1 eV for the electron, equation 7.3 gives $H_{\text{SOC}} = 390\,\text{meV}$, where the total splitting is twice the calculated energy, which is strong enough to explain the CISS effect. This simplified picture gives a spin-orbit-coupling which exceeds the spin-orbit-coupling for hydrocarbons by several orders of magnitude [222].

The idea is to create a self-assembled monolayer (SAM) of double stranded DNA (dsDNA), which would work as the spin filter, attached to a gold surface with an un-

derlying soft ferromagnetic multi-layer system generating an out-of-plane magnetization which can be switched with an external magnetic field and the magnetization is preserved without the external field. It should be therefore possible to measure the remaining small and local magnetic fields via using quantities measurable with SMLM, like emitted photons or blinking rates. The main idea is comparable to the results shown by Mondal et al. [241], but circumventing the macroscopic and diffraction limited measurements with SMLM.

A schematic drawing is presented in figure 7.3. On the left hand side the out-of-plane magnetization of the underlying multi-layer system consisting of cobalt and platinum is parallel to the movement direction of the electron. Due to the resulting more unstable state at higher energies, a tunneling along the dsDNA is more unlikely. The consequence is that the electron can recombine with in the Qdot remaining "hole" and emits a photon (see figure 2.1 **B**). In the other case, presented on the right hand side in figure 7.3, a preferred and stabilized energy state results based on the constellation of chirality and the out-of-plane magnetization. With this constellation it is more likely, that the electron is guided to the underlying gold substrate. Without the electron no recombination can take place and no photon is emitted. Therefore, the quantity of emitted photons, which is accessible in SMLM, can be used to quantify the spin polarization in an optical manner. Which of the both electron spins is stable or unstable depends on the relative movement direction, the magnetic field direction and the molecules chirality.

7.4.1. Experimental section

Sample preparation

The underlying substrate is produced by sputter deposition in a Leybold Vakuum GmbH CLAB 600. A thin natural silicon oxide layer is on top of the silicon wafer. At first a 5 nm thin layer of tantalum is sputtered on the silicon oxide and subsequent a 2 nm layer platinum, followed by three times 0.28 nm cobalt and 0.3 nm platinum with a final 0.28 nm cobalt layer before the whole soft ferromagnetic multi-layer system is covered by 6 nm gold.

Before the SAM growth is initiated the substrate has to be cleaned sufficiently by 20 min ultraviolet light ozone cleaning, storage for 20 min in absolute ethanol and drying with nitrogen. Long term storage can be done under an argon atmosphere.

The used 26 base pair long dsDNA was created by the hybridization of ssDNA, where each strand was based on the sequence taken from the supporting information by Göhler et al. [152]. To attach a Qdot on top of the dsDNA the 5'-end was modified by a C_3NH_2 group. To create a dsDNA based SAM, the final 50 μM dsDNA solution in 0.4 M potassium phosphate buffer at pH 7.4 was pipetted on the substrate. The important point is, that the surface does not dry out over the incubation time of 20 h at room temperature. To remove unbound dsDNA

the sample was sonicated in potassium buffer. The potassium buffer consists of dipotassium phosphate and monopotassium phosphate, for both a one molar stock solution was used for the final 0.4 M buffer with the desired pH of 7.4. Therefore, a 1 M stock-solution is generated by e.g. using 80.2 ml dipotassium phosphate and 19.8 ml monopotassium phosphate [94].

The cadmium tellurid Qdots (777951, Sigma-Aldrich) are coupled to the dsDNA via a zero-length cross-linker reaction [184]. The following components are used for the coupling reaction:

- 0.1 M EDC (1-ethyl-3-(3-dimethylaminopropyl)carbodiimide hydrochloride) (22980, Sigma-Aldrich)
- 0.05 M Sulfo-NHS (N-hydroxysulfosuccinimide) (24510, Sigma-Aldrich)
- 100μg/ml CdTe core-type quantum dot (777951, Sigma-Aldrich)

The previously prepared SAMs on gold were covered with this solution and incubation time was set to 2 h at room temperature before the sample was sonicated for 20 s with the potassium phosphate buffer. This step follows a careful rinsing step with double distilled water. The final preparation step was the drying with compressed air.

Sample imaging and data analysis

Prior to the imaging step, a small drop of the potassium phosphate buffer was placed on a # 1.5 coverslip (0107032, Paul Marienfeld GmbH & Co.KG, Germany). The small wafer with the dsDNA SAM and the coupled Qdots was positioned head over on the coverslip. On top lied a NdFeB magnet (Webcraft GmbH, Germany, edge length 10 mm) to generate the magnetic field. The direction of the magnetic field is switched by rotating the magnet 180°. As excitatio the laserline with a wavelength of 514 nm from an argon krypton ion laser source (70C-Spectrum, Coherent Inc., USA) is used, due to a better separation with the available filter. The illumination beam is focused to the objectives lens back focal plane with a 540 nm dichroic mirror (DCXR 540, Chroma, USA). Further separation between the luminescence of the Qdots and the illumination light was done with two long pass filters (BLP01-532R-25, LP02-514RU-25, Semrock, USA) and an additional band pass filter (ET632/60m, Chroma, USA). The image series was acquired with an EMCCD camera (iXON+ DU-888E-C00-BV, Andor Technology, Ireland) with an exposure time of 20 ms per frame.

In total 10000 frames were taken for each magnetization direction. Data analysis is done with the ImageJ [173] plugin ThunderSTORM [197], where the number of emitted photons for each localization is calculated based on the performed 2D Gaussian fit on each blinking event. All localized Qdots, with a smaller uncertainty

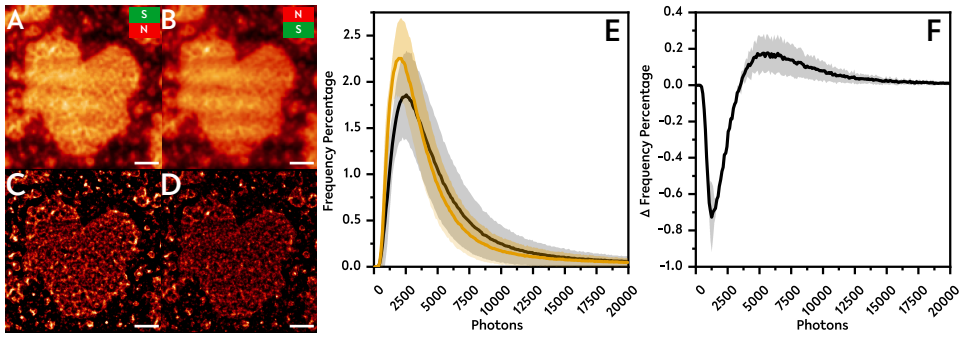

Figure 7.4.: Exemplary luminescence data set of Qdots coupled to dsDNA under different orientation of the external magnetic field (**A** magnetic north pole on the backside of the waver, **B** magnetic south pole on the wafers back side). Images **A** and **B** show an averaged image of the 10000 frames acquired during the measurement for SMLM. The corresponding super-resolved images are shown below in **C** and **D**. Scale bar 2μm. The occurrence of localizations with a certain photon number up to 20000 photons per localization is shown in **E**. The black curve shows the distribution for measurements with the magnetic north pole on the back side of the waver and the orange curve with a 180˚rotated magnet. The standard deviation of four independent measurements is shown in light orange and gray. In **F** the difference in the frequency percentage between the magnetization directions is shown in black (mean value) and the corresponding standard deviation shown in gray.

than 20 nm, were taken into account for final photon count evaluation. Therefore, the total number of localizations were histogrammed in bins of 500 photons and the measurements were repeated with the opposite magnetization direction (see figure 7.4 **E**). For a better visualization the histograms are displayed with connected lines in figures 7.4 **E** and **F**. Based on the overall localization number per data set the frequency percentage was calculated. The difference in the occurrence was then calculated by subtracting the both data sets from each other (see figure 7.4 **F**).

7.4.2. Results and discussion

The results in previously published work about spin filtering with helical molecules and the further development of this topic show that it is possible to use helical molecules for different purposes [169, 222, 303, 314]. With regard to develop an improved method for the detection of nanoscopic magnetic domains based on super-resolution optical microscopy the approaches by Mondal et al. [241] and Roy et al. [248] were adapted. The artificial dsDNA constructs presented by Göhler et al. [152] were used as a starting point. Here the hybridization of two single stranded

DNA was done before the growth of the SAM was initialized with a subsequently coupling of Qdots to the dsDNA. Due to a missing purification step after the hybridization it is not guaranteed that all to the gold bound DNA strand are double stranded DNAs. Nevertheless, the fraction of ssDNA bound to the surface should be low due to the same initial concentration of the stock solutions of the single strands. The measurements to verify the CISS effect were done with a very basic experimental setup and the acquired data is presented in figure 7.4. Between the diffraction limited images presented in figure 7.4 **A** and **B** a slight intensity difference can be seen in the look up table. Here light red to white is an indicator for higher signal count compared to dark red. A more quantitative evaluation is done by using the blinking characteristics of Qdots to achieve single molecule localizations, where the number of emitted photons per localization is taken as a measure for the CISS. Therefore, the implemented uncertainty filter function in ThunderSTORM [197] was used to remove localizations with a larger uncertainty than 20 nm. The remaining localizations were grouped together in bin of 500 photons. For a better visualization the bars of the histogram are represented via the connected curves (black and orange) in figure 7.4 **E**. Here, it is possible to see for the localizations detected with the magnetic north pole on the back side of the wafer localizations with a photon count between 5000 and 10000 photons occur more frequently in comparison to the follow up measurement with the magnetic south pole in contact with the wafer. But the increase in frequency among these photon counts is quite small with an increased mean occurrence of around 0.1%. To achieve this results only four measurements were done, so that the statistics are not large enough. To exclude potential bleaching effects, which can take place, but are more unlikely for Qdots, than for organic fluorescent dyes, the imaging scheme was changed between beginning with the magnetic north and south pole on the back side of the wafer.

All in all, it could be shown that the idea of using dsDNA as a spin filter works in combination with an optical detection by counting emitted photons during a blinking event. The number of emitted photons is an indirect measurement of the hopping or tunneling process of the created charge along the dsDNA. It depends on the spin-orbit-coupling strength and the spin, which is aligned to the external magnetic field.

Nonetheless further measurements and tests have to be done. With the magnet placed direct on top of the wafer the external magnetic field is responsible for the splitting of the energy levels and not the magnetic field of the soft ferromagnetic substrate, which will generate a much weaker magnetic field. Furthermore, a sample geometry which includes reference surface where no magnetic field should remain after removing the external field would have been of great advance. This was achieved by a structured sample where 20 μm in diameter large circles are arranged in a three times three configuration leaving one spot empty. Four of them have

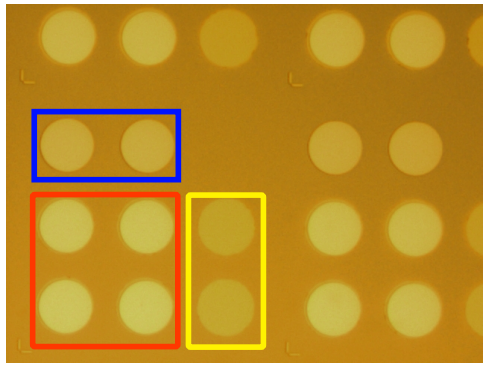

Figure 7.5.: Structured sample with circles with underlying soft-ferromagnetic multi-layers (red) and circles containing only a top gold layer as reference (yellow). The blue highlighted circles have the soft-ferromagnetic multi-layer system, but no gold on top. Therfore, no SAM should be formed on this circles.

a multi-layer soft ferromagnetic system with a gold layer on top (highlighted in red). As a reference without a magnetic field circles with only a gold layer are placed beside the ones with soft-magnetic layers (highlighted in yellow). Finally, a reference is created where no SAM should assemble, where ruthenium is the top layer (highlighted in blue). The main problem with this type of substrate was the creation of SAMs. In addition, the permanent magnet was replaced by a single coil for generating the magnetic field. With the coil, the probability of moving the sample when rotating the permanent magnet was reduced. Nevertheless, axial drift problems were observed and while changing the direction of the magnetic field the non-magnetic objective lens was moved by the magnetic field. This was, in addition to the problems forming a homogeneous SAM with coupled Qdots a further reason why a more quantitative evaluation was not possible.

8. Summary and comprehensive outlook

The focus of this work was the development of an easy to use approach to investigate the morphology of polymer particles. These particles form a dense network and respond to external stimuli, which makes them promising candidates for various applications in the life sciences, medicine and industry. It was found that rhodamine 6G, a well known, cheap and very bright laser dye worked well for this purpose, due to its interaction with the polymer network. This allows to label the network indirectly and keep the polymer network unaltered. Since the real world consists of three spatial directions a two dimensional projection does not represent the real world. By assuming that the microgels are adsorbed to the glass coverslip, but still maintain their spherical shape, a recalculation of the three dimensional network density could be performed. To proof the validity of this method the widely studied N-isopropylacrylamide (NIPAM) was investigated at different degrees of cross-linking of the polymer network. The fuzzy-sphere model, which was established based on small angle neutron scattering data could be reproduced and new findings regarding highly cross-linked NIPAM microgels were achieved. These microgels are currently under-studied and the theoretical description of their behaviour is still in progress. The method was also applied to microgels made of different polymers, which resulted in a completely different density distribution compared to NIPAM. Finally, microgels made of two different polymers were investigated and it is found that the initial core particle showed a rather low localization number while a shell forming around the core exhibited an interpenetration of the core network. This result is indicated by a higher localization number within the whole microgel. With increasing thickness the density of the shell increases and the interpenetration degree increases as can be seen by decrease of the localization density towards the middle of the microgel. This could be the result of the higher network density especially in the core region resulting in the formation of a diffusion barrier. The knowledge about the interpenetration and the increasing density or the formation of an diffusion barrier provide important information for further applications of these core-shell particles, such as their use for drug delivery, where the microgel needs to be loaded with drugs. This work also showed, that the presented method can be used to analyze a range of different microgels consisting of a single polymer or several ones.

Nevertheless, this method can be improved further if one includes 3D imaging techniques such as inducing astigmatism in the detection path of an SMLM system. This concept was used in parts of this thesis. It could also be used to check if the calculated density distribution obtained from the projected 2D data is valid and how large the deviation from the assumed model is. Recently, Hoppe Alvarez et al. [308] showed that microgels undergo a deformation in contact with coated coverslips. They also showed that this effect can be reduced by a surface modification with polyethylene glycol (PEG). The flattening of microgels at surfaces could also be observed to a certain extend for microgels where SMLM was achieved by introducing a cylindrical lens in the detection path (Chapter 4 and 5), as well as in the atomic force microscopy measurements in chapter 3 for the different cross-linker densities. It was found that higher cross-linked microgels show a lower tendency to flatten across the surface. So far the structural change of the polymer network induced by the appropriate stimulus (e.g. temperature change or pH change) was not yet investigated by super-resolution microscopy, which makes it an interesting topic for further studies. Here, all measurements were done at temperatures where the microgels are completely swollen by solvent.

For further studies on core-shell microgels the use of dual-color imaging in 3D SMLM would give further insight into the distribution of the different layers of the microgel. To show, for example, that a diffusion barrier has established due to higher cross-linking degree, fluorescence resonance energy transfer (FRET) could be used to investigate the interaction of the different interpenetrated networks in core-shell microgels, where e.g. denser areas of the gel would exhibit a higher degree of FRET. This approach does, however, cause additional challenges for the chemical labeling of the network structure.

SMLM allows to localize molecules very precisely on the scale of a few tens of nanometers. A good example for highly localized protein complexes are desmosomes, which, as an integral part of the plasma membrane in some cells, serve as an anchor of the outer membrane to the cell's cytoskeleton. These proteins enable the cell to interact with neighboring cells and to retain the cell's stability and the integrity of cell-cell interactions. As part of this study, the protein plakophilin-2 was investigated by SMLM. Plakophilin-2 is encoded in the gene PKP2 and consists of armadillo repeats plus a head and tail domain. Plakophilin-2 is the only such structural protein expressed in cardiac desmosomes. In desomosomes of the skin, the proteins plakophilin-1 and plakophilin-3 can also be found. Through a mutation of the gene it is possible to change the proteins such that parts of the protein are missing, resulting in a so-called truncation mutation. Within the cardiac desmosome, the protein plakophilin-2 connects the extra cellular cadherines desmoglein-2 and desmocollin-2 with the cytoskeleton via desmoplakin and desmin. In 90% of all genetic heart diseases one of the five named proteins is mutated and in 42.5% the origin of the disease is a mutation of PKP2. Therefore, plakophilin-2 is a

central anchor within the desmosome and a mutation leading to a displacement of the protein has dramatic consequences such as sudden heart death or arrhythmia of the heart. With specific and deliberate induction of these mutations and by introducing a fluorescent label it was possible to visualize the location of the protein within human embryonic kidney cells (HEK293T) as a model. Missing armadillo repeats of plakophilin-2 resulted in an ubiquitous distribution of the protein within the cells and this observation implies that the function of the protein is not given anymore. Alternatively, one could also use induced pluripotent stem cell, which can be induced to differentiate into cardiomyocytes [214, 279], and which would provide a more realistic framework for studying plakophilin-2 modifications as the cause of heart disease. In the entire cardiac desmosome complex there are, however, four other proteins interacting with plakophilin-2, so the question remains, which impact a single altered protein has on the entire complex. Dual-color 3D SMLM would enable to localize different interacting proteins at the same time and with high precision to help determine if the mutation in the gene is pathologic or not. A main goal for the future is the comparison and correlation of experiments performed in cell culture with heart slices from ARVC patients. Of particular interest, here, are the interactions and the interplay of desmocollin-2 / desmoglein-2 and plakophilin-2. In pathological samples the intersection between two cardiomyocytes is a favorable area of investigation. Nowadays, with advanced freezing and cutting techniques, tissue slices with a thickness of five to ten microns can be obtained. Due to the high density of muscle tissue light is scattered more strongly within tissue as compared to cell cultures with very flat growing cells. Therefore, more advanced microscopy methods are necessary to resolve the locations of plakophilin-2 and desmocollin-2 / desmoglein-2 with the necessary precision. A promising solution could be the implementation of a deformable mirror in the Fourier plane of the detection path to induce phase changes that result in a modified PSF, which is easier and more precise to detect. This can be achieved by an improved intensity distribution of the PSF (double helix [136],saddle point [201], tetrapod [224]), where the height information is encoded in the shape and symmetry of the PSF obtained from single fluorescent molecules located in different axial positions. Such a framework is the recently published ZOLA 3D method [274] which enables single molecule detection in an axial range of up to five microns. In comparison, the astigmatism based approach works well up to 600 nm depth but for longer distances along the z-axis the signal gets too weak. By using these improved PSFs it should be possible to achieve a precise localization within the intercalated disk to visualize cadherins and plakophilin-2 in pathologic cardiac muscle samples. Plakophilin-2 is exclusively expressed in the cardiac desmosomes, but it might be possible to compensate its dysfunction by introducing plakophilin-1 and plakophilin-3 enabled by CRISPR-Cas9 [216], which could then be expressed in cardiomyocytes. A successful implementation of this approach could be monitored by super-resolution microscopy. A question which

has to be answered, though, is how molecular transport processes might be altered due to the truncated protein. Within the cells this process is enabled by transport vesicles. To track the transport path over short time periods in living cells the proteins could e.g. be labeled with a fluorescent photo-activatable protein. This could also be done with the system where plakophilin-1 and plakophilin-3 are expressed. In living cells the vesicle transport could then be followed using single particle tracking methods.

Lastly, an important contribution to the credibility of scientific research was made in the course of this thesis by demonstrating that the claim that magnetic fields could improve the total number of emitted photons from organic fluorophores and therefore enable a higher localization precision is wrong. Nevertheless, special fluorescent probes exist which can be influenced by an external magnetic field and can therefore be used for fluorescence microscopy in the presence of magnetic fields [155, 217]. As of this writing, though wide-field microscopy techniques that can probe magnetic fields on the nanoscale are still missing. A scanning probe technique for measuring the magnetic field strength on the nanoscale is, for example, a modified AFM called magnetic force microscope (MFM). The quantitation of MFM measurements is, however, not straightforward, because the tip geometry has to be taken into account and the tip has to be used at a higher elevation to avoid the electrostatic and atomic forces. In recent publications chiral molecules were shown to be used as spin-filter [152, 165, 183, 241, 287, 293, 296, 314]. A possible idea is to use the methods demonstrated in the publications by Mondal et al. [241] and Roy et al. [248]. Here, a fluorescent quantum dot is bound to chiral oligomers or bacteriorhodopsin in a purple membrane. Depending on the magnetic field direction (up or down) a change in the luminescence intensity could be measured due to a transfer of charges from excitons to a nearby metal layer and the resulting modification of the photon emission process. The recombination of excitons can be inhibited when one part of the exciton (typically the electron) can tunnel through the chiral molecule and is absorbed by the underlying substrate, resulting in "quenching". Such experiments were, however, so far accomplished by measuring the signal of an ensemble of quantum-dot labeled chiral molecules. To improve the lateral resolution of such experiments single molecule techniques can be used. It was shown that Qdots are suitable probes for super-resolution microscopy techniques such as SOFI [129] where the blinking rates [164, 313] can also be used as a measure for quenching. Another measure that could be used is the total number of photons emitted, which can be measured with localization methods. To accomplish this, though, it is necessary to take benefit of core type Qdots because in comparison to core-shell Qdots they exhibit rapid blinking behaviour between a fluorescent on- and off-state [233]. This would make it possible to read out the emission for every single Qdots. To control the off-times of Qdots Gadolinium ions can be added to the surrounding liquid environment [247] to generate a

sufficiently sparse emitter density. It is, however, still quite challenging to set up a super-resolution microscope, which can be operated stably in the presence of high magnetic fields.

All in all, fluorescence super-resolution microscopy techniques can be used for different topics in the life sciences, material sciences and physics. In particular for the development and the characterization of new responsive microgels, SMLM is very useful, due to its ability to perform experiments in a liquid environment (swollen microgel by the solvent) and to control their stimulus to phase changes, such as ionic strength, temperature or magnetic fields. Similar spatial resolution to what was achieved in the course of this work can otherwise only be achieved by electron microscopy or Helium ion microscopy [297] and, therefore, opens up an entirely new parameter space for experiments that could otherwise not be done.

Bibliography

(1) R. Hooke, *Micrographia: Some physiological descriptions of minute bodies made by magnifying glasses : with observations and inquiries thereupon*, The Royal Society of London, London, 1665, DOI: 10.5962/bhl.title.904.

(2) J. Herschel, *Philosophical Transactions of the Royal Society of London*, 1845, **135**, 143–145, DOI: 10.1098/rstl.1845.0004.

(3) G. G. Stokes, *Philosophical Transactions of the Royal Society of London*, 1852, **142**, 463–562, DOI: 10.1098/rstl.1852.0022.

(4) G. G. Stokes, *Proceedings of the Royal Society of London*, 1853, **6**, 333–335, DOI: 10.1098/rspl.1850.0124.

(5) A. Baeyer, *Berichte der deutschen chemischen Gesellschaft*, 1871, **4**, 555–558, DOI: 10.1002/cber.18710040209.

(6) E. Abbe, *Archiv für Mikroskopische Anatomie*, 1873, **9**, 413–418, DOI: 10.1007/BF02956173.

(7) C. M. Sparrow, *The Astrophysical Journal*, 1916, **44**, 76, DOI: 10.1086/142271.

(8) E. Condon, *Physical Review*, 1926, **28**, 1182–1201, DOI: 10.1103/PhysRev.28.1182.

(9) J. Franck and E. G. Dymond, *Transactions of the Faraday Society*, 1926, **21**, 536, DOI: 10.1039/tf9262100536.

(10) E. U. Condon, *Physical Review*, 1928, **32**, 858–872, DOI: 10.1103/PhysRev.32.858.

(11) H. Nyquist, *Transactions of the American Institute of Electrical Engineers*, 1928, **47**, 617–644, DOI: 10.1109/T-AIEE.1928.5055024.

(12) v. F. Zernike, *Physica*, 1934, **1**, 689–704, DOI: 10.1016/S0031-8914(34)80259-5.

(13) K. A. Kobe and W. L. Gooding, *Industrial & Engineering Chemistry*, 1935, **27**, 331–333, DOI: 10.1021/ie50303a020.

(14) A. H. Coons, H. J. Creech and R. N. Jones, *Experimental Biology and Medicine*, 1941, **47**, 200–202, DOI: 10.3181/00379727-47-13084P.

(15) P. J. Flory and J. Rehner, *The Journal of Chemical Physics*, 1943, **11**, 521–526, DOI: 10.1063/1.1723792.

(16) C. E. Shannon, *Proceedings of the IRE*, 1949, **37**, 10–21, DOI: 10.1109/JRPROC.1949.232969.

(17) O. Shimomura, F. H. Johnson and Y. Saiga, *Journal of Cellular and Comparative Physiology*, 1962, **59**, 223–239, DOI: 10.1002/jcp.1030590302.

(18) D. Magde, E. Elson and W. W. Webb, *Physical Review Letters*, 1972, **29**, 705–708, DOI: 10.1103/PhysRevLett.29.705.

(19) S. W. Provencher, *Computer Physics Communications*, 1982, **27**, 213–227, DOI: 10.1016/0010-4655(82)90173-4.

(20) S. W. Provencher, *Computer Physics Communications*, 1982, **27**, 229–242, DOI: 10.1016/0010-4655(82)90174-6.

(21) D. Axelrod, T. P. Burghardt and N. L. Thompson, *Annual review of biophysics and bioengineering*, 1984, **13**, 247–268, DOI: 10.1146/annurev.bb.13.060184.001335.

(22) T. Yanagida, M. Nakase, K. Nishiyama and F. Oosawa, *Nature*, 1984, **307**, 58–60, DOI: 10.1038/307058a0.

(23) R. H. Pelton and P. Chibante, *Colloids and Surfaces*, 1986, **20**, 247–256, DOI: 10.1016/0166-6622(86)80274-8.

(24) S. Englander, D. B. Calhoun and J. J. Englander, *Analytical biochemistry*, 1987, **161**, 300–306, DOI: 10.1016/0003-2697(87)90454-4.

(25) Moerner and Kador, *Physical review letters*, 1989, **62**, 2535–2538, DOI: 10.1103/PhysRevLett.62.2535.

(26) Y. Harada, K. Sakurada, T. Aoki, D. D. Thomas and T. Yanagida, *Journal of Molecular Biology*, 1990, **216**, 49–68, DOI: 10.1016/S0022-2836(05)80060-9.

(27) M. Shibayama, T. Tanaka and C. C. Han, *The Journal of Chemical Physics*, 1992, **97**, 6842–6854, DOI: 10.1063/1.463637.

(28) D. C. Neckers and O. M. Valdes-Aguilera, in *Advances in photochemistry*, ed. D. H. Volman, G. S. Hammond and D. C. Neckers, John Wiley, New York, 1993, vol. 55, pp. 315–394, DOI: 10.1002/9780470133491.ch4.

(29) S. W. Hell and J. Wichmann, *Optics Letters*, 1994, **19**, 780–782, DOI: 10.1364/ol.19.000780.

(30) E. Betzig, *Optics Letters*, 1995, **20**, 237–239, DOI: 10.1364/OL.20.000237.

(31) S. W. Hell and M. Kroug, *Applied Physics B Lasers and Optics*, 1995, **60**, 495–497, DOI: 10.1007/BF01081333.

(32) M. Ester, H.-P. Kriegel, J. Sander and X. Xu, Proceedings of the Second International Conference on Knowledge Discovery and Data Mining, AAAI Press, 1996, pp. 226–231, http://dl.acm.org/citation.cfm?id=3001460.3001507.

(33) M. Shibayama, T. Norisuye and S. Nomura, *Macromolecules*, 1996, **29**, 8746–8750, DOI: 10.1021/ma9609994.

(34) M. J. Snowden, B. Z. Chowdhry, B. Vincent and G. E. Morris, *Journal of the Chemical Society, Faraday Transactions*, 1996, **92**, 5013, DOI: 10.1039/ft9969205013.

(35) R. M. Dickson, A. B. Cubitt, R. Y. Tsien and W. E. Moerner, *Nature*, 1997, **388**, 355–358, DOI: 10.1038/41048.

(36) A. Gruber, A. Dräbenstedt, C. Tietz, L. Fleury, J. Wrachtrup and C. v. Borczyskowski, *Science (New York, N.Y.)*, 1997, **276**, 2012–2014, DOI: 10.1126/science.276.5321.2012.

(37) S. J. Mears, Y. Deng, T. Cosgrove and R. Pelton, *Langmuir : the ACS journal of surfaces and colloids*, 1997, **13**, 1901–1906, DOI: 10.1021/la960515x.

(38) H. M. Crowther, B. R. Saunders, S. J. Mears, T. Cosgrove, B. Vincent, S. M. King and G.-E. Yu, *Colloids and Surfaces A: Physicochemical and Engineering Aspects*, 1999, **152**, 327–333, DOI: 10.1016/S0927-7757(98)00875-9.

(39) R. Heintzmann and C. G. Cremer, Optical Biopsies and Microscopic Techniques III, ed. I. J. Bigio, H. Schneckenburger, J. Slavik, K. Svanberg and P. M. Viallet, SPIE, 1999, pp. 185–196, DOI: 10.1117/12.336833.

(40) D. Ito and K. Kubota, *Polymer Journal*, 1999, **31**, 254–257, DOI: 10.1295/polymj.31.254.

(41) T. A. Klar and S. W. Hell, *Optics Letters*, 1999, **24**, 954–956, DOI: 10.1364/ol.24.000954.

(42) N. Panchuk-Voloshina, R. P. Haugland, J. Bishop-Stewart, M. K. Bhalgat, P. J. Millard, F. Mao and W. Y. Leung, *The journal of histochemistry and cytochemistry : official journal of the Histochemistry Society*, 1999, **47**, 1179–1188, DOI: 10.1177/002215549904700910.

(43) K. Ray, *Science*, 1999, **283**, 814–816, DOI: 10.1126/science.283.5403.814.

(44) H. Senff and W. Richtering, *The Journal of Chemical Physics*, 1999, **111**, 1705–1711, DOI: 10.1063/1.479430.

(45) C. Groussard, I. Morel, M. Chevanne, M. Monnier, J. Cillard and A. Delamarche, *Journal of Applied Physiology*, 2000, **89**, 169–175, DOI: 10.1152/jappl.2000.89.1.169.

(46) M. G. L. Gustafsson, *Journal of Microscopy*, 2000, **198**, 82–87, DOI: 10.1046/j.1365-2818.2000.00710.x.

(47) T. A. Klar, S. Jakobs, M. Dyba, A. Egner and S. W. Hell, *Proceedings of the National Academy of Sciences of the United States of America*, 2000, **97**, 8206–8210, DOI: 10.1073/pnas.97.15.8206.

(48) P. V. Patil and D. P. Ballou, *Analytical biochemistry*, 2000, **286**, 187–192, DOI: 10.1006/abio.2000.4802.

(49) R. Pelton, *Advances in Colloid and Interface Science*, 2000, **85**, 1–33, DOI: 10.1016/S0001-8686(99)00023-8.

(50) A. Fernández-Nieves, A. Fernández-Barbero and F. J. de las Nieves, *The Journal of Chemical Physics*, 2001, **115**, 7644–7649, DOI: 10.1063/1.1403002.

(51) K. Kratz, T. Hellweg and W. Eimer, *Polymer*, 2001, **42**, 6631–6639, DOI: 10.1016/S0032-3861(01)00099-4.

(52) M. Ono, T. Murakami, A. Kudo, M. Isshiki, H. Sawada and a. Segawa, *Journal of Histochemistry & Cytochemistry*, 2001, **49**, 305–311, DOI: 10.1177/002215540104900304.

(53) *Monodispersed Particles*, ed. T. Sugimoto, Elsevier, Amsterdam, 2001.

(54) B. Brocklehurst, *Chemical Society Reviews*, 2002, **31**, 301–311, DOI: 10.1039/B107250C.

(55) A. Fernández-Barbero, A. Fernández-Nieves, I. Grillo and E. López-Cabarcos, *Physical review. E, Statistical, nonlinear, and soft matter physics*, 2002, **66**, 051803, DOI: 10.1103/PhysRevE.66.051803.

(56) T. Hellweg, K. Kratz, S. Pouget and W. Eimer, *Colloids and Surfaces A: Physicochemical and Engineering Aspects*, 2002, **202**, 223–232, DOI: 10.1016/S0927-7757(01)01077-9.

(57) R. E. Thompson, D. R. Larson and W. W. Webb, *Biophysical Journal*, 2002, **82**, 2775–2783, DOI: 10.1016/S0006-3495(02)75618-X.

(58) M. Bijlmakers, *Trends in Cell Biology*, 2003, **13**, 32–42, DOI: 10.1016/S0962-8924(02)00008-9.

(59) E. Fernandez and P. Artal, *Optics express*, 2003, **11**, 1056–1069, DOI: 10.1364/oe.11.001056.

(60) K.-C. Ho, J. K. Leach, K. Eley, R. B. Mikkelsen and P.-S. Lin, *American journal of clinical oncology*, 2003, **26**, e86–91, DOI: 10.1097/01.COC.0000077937.91824.44.

(61) R. Zondervan, F. Kulzer, S. B. Orlinskii and M. Orrit, *The Journal of Physical Chemistry A*, 2003, **107**, 6770–6776, DOI: 10.1021/jp034723r.

(62) S. C. Blanchard, R. L. Gonzalez, H. D. Kim, S. Chu and J. D. Puglisi, *Nature structural & molecular biology*, 2004, **11**, 1008–1014, DOI: 10.1038/nsmb831.

(63) S. C. Blanchard, H. D. Kim, R. L. Gonzalez, J. D. Puglisi and S. Chu, *Proceedings of the National Academy of Sciences of the United States of America*, 2004, **101**, 12893–12898, DOI: 10.1073/pnas.0403884101.

(64) A. Fernández-Nieves, F. J. de las Nieves and A. Fernández-Barbero, *The Journal of Chemical Physics*, 2004, **120**, 374–378, DOI: 10.1063/1.1629281.

(65) S. Getsios, A. C. Huen and K. J. Green, *Nature reviews. Molecular cell biology*, 2004, **5**, 271–281, DOI: 10.1038/nrm1356.

(66) J. Huisken, J. Swoger, F. Del Bene, J. Wittbrodt and E. H. K. Stelzer, *Science (New York, N.Y.)*, 2004, **305**, 1007–1009, DOI: 10.1126/science.1100035.

(67) N. Jalili and K. Laxminarayana, *Mechatronics*, 2004, **14**, 907–945, DOI: 10.1016/j.mechatronics.2004.04.005.

(68) A. Keppler, H. Pick, C. Arrivoli, H. Vogel and K. Johnsson, *Proceedings of the National Academy of Sciences of the United States of America*, 2004, **101**, 9955–9959, DOI: 10.1073/pnas.0401923101.

(69) J. Kim, M. J. Serpe and L. A. Lyon, *Journal of the American Chemical Society*, 2004, **126**, 9512–9513, DOI: 10.1021/ja047274x.

(70) S. Nayak and L. A. Lyon, *Chemistry of Materials*, 2004, **16**, 2623–2627, DOI: 10.1021/cm049650i.

(71) B. R. Saunders, *Langmuir*, 2004, **20**, 3925–3932, DOI: 10.1021/la036390v.

(72) M. J. Serpe and L. A. Lyon, *Chemistry of Materials*, 2004, **16**, 4373–4380, DOI: 10.1021/cm048844v.

(73) M. Stieger, W. Richtering, J. S. Pedersen and P. Lindner, *The Journal of Chemical Physics*, 2004, **120**, 6197–6206, DOI: 10.1063/1.1665752.

(74) J. Wiedenmann, S. Ivanchenko, F. Oswald, F. Schmitt, C. Röcker, A. Salih, K.-D. Spindler and G. U. Nienhaus, *Proceedings of the National Academy of Sciences of the United States of America*, 2004, **101**, 15905–15910, DOI: 10.1073/pnas.0403668101.

(75) R. Zhang, L. Zhang and P. Somasundaran, *Journal of colloid and interface science*, 2004, **278**, 453–460, DOI: 10.1016/j.jcis.2004.06.045.

(76) D. R. Garrod, M. Y. Berika, W. F. Bardsley, D. Holmes and L. Tabernero, *Journal of cell science*, 2005, **118**, 5743–5754, DOI: 10.1242/jcs.02700.

(77) L. M. Godsel, S. N. Hsieh, E. V. Amargo, A. E. Bass, L. T. Pascoe-McGillicuddy, A. C. Huen, M. E. Thorne, C. A. Gaudry, J. K. Park, K. Myung, R. D. Goldman, T.-L. Chew and K. J. Green, *The Journal of cell biology*, 2005, **171**, 1045–1059, DOI: 10.1083/jcb.200510038.

(78) M. G. L. Gustafsson, *Proceedings of the National Academy of Sciences of the United States of America*, 2005, **102**, 13081–13086, DOI: 10.1073/pnas.0406877102.

(79) M. Hofmann, C. Eggeling, S. Jakobs and S. W. Hell, *Proceedings of the National Academy of Sciences of the United States of America*, 2005, **102**, 17565–17569, DOI: 10.1073/pnas.0506010102.

(80) S. Meyer and W. Richtering, *Macromolecules*, 2005, **38**, 1517–1519, DOI: 10.1021/ma047776v.

(81) S. Nayak and L. A. Lyon, *Angewandte Chemie (International ed. in English)*, 2005, **44**, 7686–7708, DOI: 10.1002/anie.200501321.

(82) K. Nienhaus, G. U. Nienhaus, J. Wiedenmann and H. Nar, *Proceedings of the National Academy of Sciences of the United States of America*, 2005, **102**, 9156–9159, DOI: 10.1073/pnas.0501874102.

(83) P.-G. de Gennes, *Soft matter*, 2005, **1**, 16, DOI: 10.1039/b419223k.

(84) M. A. Rizzo and D. W. Piston, *Biophysical Journal*, 2005, **88**, L14–6, DOI: 10.1529/biophysj.104.055442.

(85) I. Berndt, C. Popescu, F.-J. Wortmann and W. Richtering, *Angewandte Chemie (International ed. in English)*, 2006, **45**, 1081–1085, DOI: 10.1002/anie.200502893.

(86) E. Betzig, G. H. Patterson, R. Sougrat, O. W. Lindwasser, S. Olenych, J. S. Bonifacino, M. W. Davidson, J. Lippincott-Schwartz and H. F. Hess, *Science (New York, N.Y.)*, 2006, **313**, 1642–1645, DOI: 10.1126/science.1127344.

(87) M. Das, H. Zhang and E. Kumacheva, *Annual Review of Materials Research*, 2006, **36**, 117–142, DOI: 10.1146/annurev.matsci.36.011205.123513.

(88) S. T. Hess, T. P. K. Girirajan and M. D. Mason, *Biophysical Journal*, 2006, **91**, 4258–4272, DOI: 10.1529/biophysj.106.091116.

(89) C. Joo, S. A. McKinney, M. Nakamura, I. Rasnik, S. Myong and T. Ha, *Cell*, 2006, **126**, 515–527, DOI: 10.1016/j.cell.2006.06.042.

(90) Y. Lu, Y. Mei, M. Ballauff and M. Drechsler, *The journal of physical chemistry. B*, 2006, **110**, 3930–3937, DOI: 10.1021/jp057149n.

(91) Y. Lu, Y. Mei, M. Drechsler and M. Ballauff, *Angewandte Chemie (International ed. in English)*, 2006, **45**, 813–816, DOI: 10.1002/anie.200502731.

(92) J. B. Pawley, *Handbook of biological confocal microscopy*, Springer, New York, NY, 3. ed., 2006, DOI: 10.1007/978-0-387-45524-2.

(93) K. Pilichou, A. Nava, C. Basso, G. Beffagna, B. Bauce, A. Lorenzon, G. Frigo, A. Vettori, M. Valente, J. Towbin, G. Thiene, G. A. Danieli and A. Rampazzo, *Circulation*, 2006, **113**, 1171–1179, DOI: 10.1161/CIRCULATIONAHA.105.583674.

(94) *Cold Spring Harbor Protocols*, 2006, **2006**, pdb.tab19, DOI: 10.1101/pdb.tab19.

(95) I. Rasnik, S. A. McKinney and T. Ha, *Nature methods*, 2006, **3**, 891–893, DOI: 10.1038/nmeth934.

(96) M. J. Rust, M. Bates and X. Zhuang, *Nature methods*, 2006, **3**, 793–795, DOI: 10.1038/nmeth929.

(97) A. Sharonov and R. M. Hochstrasser, *Proceedings of the National Academy of Sciences of the United States of America*, 2006, **103**, 18911–18916, DOI: 10.1073/pnas.0609643104.

(98) J. Wiedenmann and G. U. Nienhaus, *Expert review of proteomics*, 2006, **3**, 361–374, DOI: 10.1586/14789450.3.3.361.

(99) M. Ballauff, *Progress in Polymer Science*, 2007, **32**, 1135–1151, DOI: 10.1016/j.progpolymsci.2007.05.002.

(100) S. Bhattacharya, F. Eckert, V. Boyko and A. Pich, *Small (Weinheim an der Bergstrasse, Germany)*, 2007, **3**, 650–657, DOI: 10.1002/smll.200600590.

(101) W. Choi, C. Fang-Yen, K. Badizadegan, S. Oh, N. Lue, R. R. Dasari and M. S. Feld, *Nature Methods*, 2007, **4**, 717–719, DOI: 10.1038/NMETH1078.

(102) D. M. Chudakov, S. Lukyanov and K. A. Lukyanov, *Nature protocols*, 2007, **2**, 2024–2032, DOI: 10.1038/nprot.2007.291.

(103) C.-C. Fu, H.-Y. Lee, K. Chen, T.-S. Lim, H.-Y. Wu, P.-K. Lin, P.-K. Wei, P.-H. Tsao, H.-C. Chang and W. Fann, *Proceedings of the National Academy of Sciences of the United States of America*, 2007, **104**, 727–732, DOI: 10.1073/pnas.0605409104.

(104) K. J. Green and C. L. Simpson, *The Journal of investigative dermatology*, 2007, **127**, 2499–2515, DOI: 10.1038/sj.jid.5701015.

(105) T.-H. Lee, L. J. Lapidus, W. Zhao, K. J. Travers, D. Herschlag and S. Chu, *Biophysical Journal*, 2007, **92**, 3275–3283, DOI: 10.1529/biophysj.106.094623.

(106) J. B. Munro, R. B. Altman, N. O'Connor and S. C. Blanchard, *Molecular cell*, 2007, **25**, 505–517, DOI: 10.1016/j.molcel.2007.01.022.

(107) D. Suzuki, S. Tsuji and H. Kawaguchi, *Journal of the American Chemical Society*, 2007, **129**, 8088–8089, DOI: 10.1021/ja072258w.

(108) S. C. Thickett and R. G. Gilbert, *Polymer*, 2007, **48**, 6965–6991, DOI: 10.1016/j.polymer.2007.09.031.

(109) J. Widengren, A. Chmyrov, C. Eggeling, P.-A. Löfdahl and C. A. M. Seidel, *The Journal of Physical Chemistry A*, 2007, **111**, 429–440, DOI: 10.1021/jp0646325.

(110) C. E. Aitken, R. A. Marshall and J. D. Puglisi, *Biophysical Journal*, 2008, **94**, 1826–1835, DOI: 10.1529/biophysj.107.117689.

(111) B. Alberts, J. Wilson, T. Hunt and A. Johnson, *Molecular biology of the cell*, Garland Science, New York, NY, 5. ed., 2008.

(112) D. Garrod and M. Chidgey, *Biochimica et biophysica acta*, 2008, **1778**, 572–587, DOI: 10.1016/j.bbamem.2007.07.014.

(113) M. G. L. Gustafsson, L. Shao, P. M. Carlton, C. J. R. Wang, I. N. Golubovskaya, W. Z. Cande, D. A. Agard and J. W. Sedat, *Biophysical Journal*, 2008, **94**, 4957–4970, DOI: 10.1529/biophysj.107.120345.

(114) B. Harke, J. Keller, C. K. Ullal, V. Westphal, A. Schönle and S. W. Hell, *Optics express*, 2008, **16**, 4154–4162, DOI: 10.1364/oe.16.004154.

(115) M. Heilemann, S. van de Linde, M. Schüttpelz, R. Kasper, B. Seefeldt, A. Mukherjee, P. Tinnefeld and M. Sauer, *Angewandte Chemie (International ed. in English)*, 2008, **47**, 6172–6176, DOI: 10.1002/anie.200802376.

(116) T. Hirano, K. Nakamura, T. Kamikubo, S. Ishii, K. Tani, T. Mori and T. Sato, *Journal of Polymer Science Part A: Polymer Chemistry*, 2008, **46**, 4575–4583, DOI: 10.1002/pola.22797.

(117) B. Huang, W. Wang, M. Bates and X. Zhuang, *Science (New York, N.Y.)*, 2008, **319**, 810–813, DOI: 10.1126/science.1153529.

(118) R. Joshi-Mukherjee, W. Coombs, H. Musa, E. Oxford, S. Taffet and M. Delmar, *Heart rhythm*, 2008, **5**, 1715–1723, DOI: 10.1016/j.hrthm.2008.09.009.

(119) M. F. Juette, T. J. Gould, M. D. Lessard, M. J. Mlodzianoski, B. S. Nagpure, B. T. Bennett, S. T. Hess and J. Bewersdorf, *Nature methods*, 2008, **5**, 527–529, DOI: 10.1038/nmeth.1211.

(120) M. Karg, I. Pastoriza-Santos, B. Rodriguez-González, R. von Klitzing, S. Wellert and T. Hellweg, *Langmuir : the ACS journal of surfaces and colloids*, 2008, **24**, 6300–6306, DOI: 10.1021/la702996p.

(121) G. V. Los, L. P. Encell, M. G. McDougall, D. D. Hartzell, N. Karassina, C. Zimprich, M. G. Wood, R. Learish, R. F. Ohana, M. Urh, D. Simpson, J. Mendez, K. Zimmerman, P. Otto, G. Vidugiris, J. Zhu, A. Darzins, D. H. Klaubert, R. F. Bulleit and K. V. Wood, *ACS chemical biology*, 2008, **3**, 373–382, DOI: 10.1021/cb800025k.

(122) J. K. Oh, R. Drumright, D. J. Siegwart and K. Matyjaszewski, *Progress in Polymer Science*, 2008, **33**, 448–477, DOI: 10.1016/j.progpolymsci.2008.01.002.

(123) S. Ram, P. Prabhat, J. Chao, E. S. Ward and R. J. Ober, *Biophysical Journal*, 2008, **95**, 6025–6043, DOI: 10.1529/biophysj.108.140392.

(124) U. Resch-Genger, M. Grabolle, S. Cavaliere-Jaricot, R. Nitschke and T. Nann, *Nature methods*, 2008, **5**, 763–775, DOI: 10.1038/nmeth.1248.

(125) L. Schermelleh, P. M. Carlton, S. Haase, L. Shao, L. Winoto, P. Kner, B. Burke, M. C. Cardoso, D. A. Agard, M. G. L. Gustafsson, H. Leonhardt and J. W. Sedat, *Science*, 2008, **320**, 1332–1336, DOI: 10.1126/science.1156947.

(126) H. Shroff, C. G. Galbraith, J. A. Galbraith and E. Betzig, *Nature methods*, 2008, **5**, 417–423, DOI: 10.1038/nmeth.1202.

(127) C. Steinhauer, C. Forthmann, J. Vogelsang and P. Tinnefeld, *Journal of the American Chemical Society*, 2008, **130**, 16840–16841, DOI: 10.1021/ja806590m.

(128) M. Tokunaga, N. Imamoto and K. Sakata-Sogawa, *Nature methods*, 2008, **5**, 159–161, DOI: 10.1038/nmeth1171.

(129) T. Dertinger, R. Colyer, G. Iyer, S. Weiss and J. Enderlein, *Proceedings of the National Academy of Sciences of the United States of America*, 2009, **106**, 22287–22292, DOI: 10.1073/pnas.0907866106.

(130) B. W. Garner, T. Cai, S. Ghosh, Z. Hu and A. Neogi, *Applied Physics Express*, 2009, **2**, 057001, DOI: 10.1143/APEX.2.057001.

(131) C. Gell, M. Berndt, J. Enderlein and S. Diez, *Journal of microscopy*, 2009, **234**, 38–46, DOI: 10.1111/j.1365-2818.2009.03147.x.

(132) C. Hall, S. Li, H. Li, V. Creason and J. K. Wahl, *Cell communication & adhesion*, 2009, **16**, 15–27, DOI: 10.1080/15419060903009329.

(133) M. Karg, Y. Lu, E. Carbó-Argibay, I. Pastoriza-Santos, J. Pérez-Juste, L. M. Liz-Marzán and T. Hellweg, *Langmuir : the ACS journal of surfaces and colloids*, 2009, **25**, 3163–3167, DOI: 10.1021/la803458j.

(134) R. Liu, M. Fraylich and B. R. Saunders, *Colloid and Polymer Science*, 2009, **287**, 627–643, DOI: 10.1007/s00396-009-2028-x.

(135) H. Montón, C. Nogués, E. Rossinyol, O. Castell and M. Roldán, *Journal of nanobiotechnology*, 2009, **7**, 4, DOI: 10.1186/1477-3155-7-4.

(136) S. R. P. Pavani, M. A. Thompson, J. S. Biteen, S. J. Lord, N. Liu, R. J. Twieg, R. Piestun and W. E. Moerner, *Proceedings of the National Academy of Sciences of the United States of America*, 2009, **106**, 2995–2999, DOI: 10.1073/pnas.0900245106.

(137) B. R. Saunders, N. Laajam, E. Daly, S. Teow, X. Hu and R. Stepto, *Advances in Colloid and Interface Science*, 2009, **147-148**, 251–262, DOI: 10.1016/j.cis.2008.08.008.

(138) G. Shtengel, J. A. Galbraith, C. G. Galbraith, J. Lippincott-Schwartz, J. M. Gillette, S. Manley, R. Sougrat, C. M. Waterman, P. Kanchanawong, M. W. Davidson, R. D. Fetter and H. F. Hess, *Proceedings of the National Academy of Sciences of the United States of America*, 2009, **106**, 3125–3130, DOI: 10.1073/pnas.0813131106.

(139) D. Baddeley, M. B. Cannell and C. Soeller, *Microscopy and microanalysis : the official journal of Microscopy Society of America, Microbeam Analysis Society, Microscopical Society of Canada*, 2010, **16**, 64–72, DOI: 10.1017/S143192760999122X.

(140) D. M. Chudakov, M. V. Matz, S. Lukyanov and K. A. Lukyanov, *Physiological reviews*, 2010, **90**, 1103–1163, DOI: 10.1152/physrev.00038.2009.

(141) P. A. L. Fernandes, S. Schmidt, M. Zeiser, A. Fery and T. Hellweg, *Soft matter*, 2010, **6**, 3455, DOI: 10.1039/c0sm00275e.

(142) R. S. Hegde and H. L. Ploegh, *Current opinion in cell biology*, 2010, **22**, 437–446, DOI: 10.1016/j.ceb.2010.05.005.

(143) Y. Lu, J. Yuan, F. Polzer, M. Drechsler and J. Preussner, *ACS nano*, 2010, **4**, 7078–7086, DOI: 10.1021/nn102622d.

(144) T. Minamino, I. Komuro and M. Kitakaze, *Circulation research*, 2010, **107**, 1071–1082, DOI: 10.1161/CIRCRESAHA.110.227819.

(145) K. I. Mortensen, L. S. Churchman, J. A. Spudich and H. Flyvbjerg, *Nature methods*, 2010, **7**, 377–381, DOI: 10.1038/nmeth.1447.

(146) S. Schachschal, A. Balaceanu, C. Melian, D. E. Demco, T. Eckert, W. Richtering and A. Pich, *Macromolecules*, 2010, **43**, 4331–4339, DOI: 10.1021/ma100184h.

(147) S. Schmidt, M. Zeiser, T. Hellweg, C. Duschl, A. Fery and H. Möhwald, *Advanced Functional Materials*, 2010, **20**, 3235–3243, DOI: 10.1002/adfm.201000730.

(148) H. Zang, S. Zhang and K. Hapeshi, *Journal of Bionic Engineering*, 2010, **7**, S232–S237, DOI: 10.1016/S1672-6529(09)60240-7.

(149) M. T. Colvin, A. B. Ricks, A. M. Scott, A. L. Smeigh, R. Carmieli, T. Miura and M. R. Wasielewski, *Journal of the American Chemical Society*, 2011, **133**, 1240–1243, DOI: 10.1021/ja1094815.

(150) G. T. Dempsey, J. C. Vaughan, K. H. Chen, M. Bates and X. Zhuang, *Nature methods*, 2011, **8**, 1027–1036, DOI: 10.1038/nmeth.1768.

(151) J. Engelhardt, J. Keller, P. Hoyer, M. Reuss, T. Staudt and S. W. Hell, *Nano letters*, 2011, **11**, 209–213, DOI: 10.1021/nl103472b.

(152) B. Göhler, V. Hamelbeck, T. Z. Markus, M. Kettner, G. F. Hanne, Z. Vager, R. Naaman and H. Zacharias, *Science (New York, N.Y.)*, 2011, **331**, 894–897, DOI: 10.1126/science.1199339.

(153) P. Hoyer, T. Staudt, J. Engelhardt and S. W. Hell, *Nano letters*, 2011, **11**, 245–250, DOI: 10.1021/nl103639f.

(154) C. A. Krusche, B. Holthöfer, V. Hofe, A. M. van de Sandt, L. Eshkind, E. Bockamp, M. W. Merx, S. Kant, R. Windoffer and R. E. Leube, *Basic research in cardiology*, 2011, **106**, 617–633, DOI: 10.1007/s00395-011-0175-y.

(155) H. Lee, N. Yang and A. E. Cohen, *Nano letters*, 2011, **11**, 5367–5372, DOI: 10.1021/nl202950h.

(156) Y. Lu and M. Ballauff, *Progress in Polymer Science*, 2011, **36**, 767–792, DOI: 10.1016/j.progpolymsci.2010.12.003.

(157) V. N. Mochalin, O. Shenderova, D. Ho and Y. Gogotsi, *Nature nanotechnology*, 2011, **7**, 11–23, DOI: 10.1038/nnano.2011.209.

(158) R. Pelton and T. Hoare, in *Microgel suspensions*, ed. A. Fernandez-Nieves, Wiley-VCH, Weinheim, 2011, vol. 41, pp. 1–32, DOI: 10.1002/9783527632992.ch1.

(159) I. Schoen, J. Ries, E. Klotzsch, H. Ewers and V. Vogel, *Nano letters*, 2011, **11**, 4008–4011, DOI: 10.1021/nl2025954.

(160) S. van de Linde, I. Krstić, T. Prisner, S. Doose, M. Heilemann and M. Sauer, *Photochemical & photobiological sciences : Official journal of the European Photochemistry Association and the European Society for Photobiology*, 2011, **10**, 499–506, DOI: 10.1039/c0pp00317d.

(161) N. Welsch, M. Ballauff and Y. Lu, in *Chemical Design of Responsive Microgels*, ed. A. Pich and K. Albrecht, Springer-Verlag Berlin Heidelberg, Berlin, Heidelberg, 2011, vol. 234, pp. 129–163, DOI: 10.1007/12_2010_71.

(162) Y. Zhang and A. Clapp, *Sensors (Basel, Switzerland)*, 2011, **11**, 11036–11055, DOI: 10.3390/s111211036.

(163) Y. Dai, P. Ma, Z. Cheng, X. Kang, X. Zhang, Z. Hou, C. Li, D. Yang, X. Zhai and J. Lin, *ACS nano*, 2012, **6**, 3327–3338, DOI: 10.1021/nn300303q.

(164) S. Geissbuehler, N. L. Bocchio, C. Dellagiacoma, C. Berclaz, M. Leutenegger and T. Lasser, *Optical Nanoscopy*, 2012, **1**, 4, DOI: 10.1186/2192-2853-1-4.

(165) R. Gutierrez, E. Díaz, R. Naaman and G. Cuniberti, *Physical Review B*, 2012, **85**, 1109, DOI: 10.1103/PhysRevB.85.081404.

(166) T. Ha and P. Tinnefeld, *Annual review of physical chemistry*, 2012, **63**, 595–617, DOI: 10.1146/annurev-physchem-032210-103340.

(167) T. Mappes, N. Jahr, A. Csaki, N. Vogler, J. Popp and W. Fritzsche, *Angewandte Chemie (International ed. in English)*, 2012, **51**, 11208–11212, DOI: 10.1002/anie.201204688.

(168) A. L. McEvoy, H. Hoi, M. Bates, E. Platonova, P. J. Cranfill, M. A. Baird, M. W. Davidson, H. Ewers, J. Liphardt and R. E. Campbell, *PLoS ONE*, 2012, **7**, e51314, DOI: 10.1371/journal.pone.0051314.

(169) R. Naaman and D. H. Waldeck, *The journal of physical chemistry letters*, 2012, **3**, 2178–2187, DOI: 10.1021/jz300793y.

(170) D. Nečas and P. Klapetek, *Open Physics*, 2012, **10**, 99, DOI: 10.2478/s11534-011-0096-2.

(171) M. Pernia Leal, A. Torti, A. Riedinger, R. La Fleur, D. Petti, R. Cingolani, R. Bertacco and T. Pellegrino, *ACS nano*, 2012, **6**, 10535–10545, DOI: 10.1021/nn3028425.

(172) S. Rickelt, *Cell and tissue research*, 2012, **348**, 281–294, DOI: 10.1007/s00441-011-1314-3.

(173) J. Schindelin, I. Arganda-Carreras, E. Frise, V. Kaynig, M. Longair, T. Pietzsch, S. Preibisch, C. Rueden, S. Saalfeld, B. Schmid, J.-Y. Tinevez, D. J. White, V. Hartenstein, K. Eliceiri, P. Tomancak and A. Cardona, *Nature methods*, 2012, **9**, 676–682, DOI: 10.1038/nmeth.2019.

(174) K. F. Sonnen, L. Schermelleh, H. Leonhardt and E. A. Nigg, *Biology open*, 2012, **1**, 965–976, DOI: 10.1242/bio.20122337.

(175) C. D. Sorrell and M. J. Serpe, *Analytical and bioanalytical chemistry*, 2012, **402**, 2385–2393, DOI: 10.1007/s00216-012-5736-x.

(176) O. M. Subach, D. Entenberg, J. S. Condeelis and V. V. Verkhusha, *Journal of the American Chemical Society*, 2012, **134**, 14789–14799, DOI: 10.1021/ja3034137.

(177) M. Swoboda, J. Henig, H.-M. Cheng, D. Brugger, D. Haltrich, N. Plumeré and M. Schlierf, *ACS nano*, 2012, **6**, 6364–6369, DOI: 10.1021/nn301895c.

(178) B. Wedel, M. Zeiser and T. Hellweg, *Zeitschrift für Physikalische Chemie*, 2012, **226**, 737–748, DOI: 10.1524/zpch.2012.0267.

(179) M. Zeiser, I. Freudensprung and T. Hellweg, *Polymer*, 2012, **53**, 6096–6101, DOI: 10.1016/j.polymer.2012.10.001.

(180) J. Zhou, J. Wei, T. Ngai, L. Wang, D. Zhu and J. Shen, *Macromolecules*, 2012, **45**, 6158–6167, DOI: 10.1021/ma300454h.

(181) N. Banterle, K. H. Bui, E. A. Lemke and M. Beck, *Journal of structural biology*, 2013, **183**, 363–367, DOI: 10.1016/j.jsb.2013.05.004.

(182) H. Calkins, *Current problems in cardiology*, 2013, **38**, 103–123, DOI: 10.1016/j.cpcardiol.2012.12.002.

(183) R. Gutierrez, E. Díaz, C. Gaul, T. Brumme, F. Domínguez-Adame and G. Cuniberti, *The Journal of Physical Chemistry C*, 2013, **117**, 22276–22284, DOI: 10.1021/jp401705x.

(184) G. T. Hermanson, in *Bioconjugate Techniques*, ed. G. T. Hermanson, Elsevier/AP, Amsterdam, 2013, pp. 259–273, DOI: 10.1016/B978-0-12-382239-0.00004-2.

(185) F. Huang, T. M. P. Hartwich, F. E. Rivera-Molina, Y. Lin, W. C. Duim, J. J. Long, P. D. Uchil, J. R. Myers, M. A. Baird, W. Mothes, M. W. Davidson, D. Toomre and J. Bewersdorf, *Nature methods*, 2013, **10**, 653–658, DOI: 10.1038/nmeth.2488.

(186) F. I. Marcus, S. Edson and J. A. Towbin, *Journal of the American College of Cardiology*, 2013, **61**, 1945–1948, DOI: 10.1016/j.jacc.2013.01.073.

(187) R. P. J. Nieuwenhuizen, K. A. Lidke, M. Bates, D. L. Puig, D. Grünwald, S. Stallinga and B. Rieger, *Nature methods*, 2013, **10**, 557–562, DOI: 10.1038/nmeth.2448.

(188) N. Olivier, D. Keller, V. S. Rajan, P. Gönczy and S. Manley, *Biomedical Optics Express*, 2013, **4**, 885–899, DOI: 10.1364/BOE.4.000885.

(189) J. Ries, V. Udayar, A. Soragni, S. Hornemann, K. P. R. Nilsson, R. Riek, C. Hock, H. Ewers, A. A. Aguzzi and L. Rajendran, *ACS chemical neuroscience*, 2013, **4**, 1057–1061, DOI: 10.1021/cn400091m.

(190) J. Romero, E. Mejia-Lopez, C. Manrique and R. Lucariello, *Clinical Medicine Insights. Cardiology*, 2013, **7**, 97–114, DOI: 10.4137/CMC.S10940.

(191) S. Thaiboonrod, C. Berkland, A. H. Milani, R. Ulijn and B. R. Saunders, *Soft matter*, 2013, **9**, 3920, DOI: 10.1039/c3sm27728c.

(192) A. G. York, P. Chandris, D. D. Nogare, J. Head, P. Wawrzusin, R. S. Fischer, A. Chitnis and H. Shroff, *Nature methods*, 2013, **10**, 1122–1126, DOI: 10.1038/nmeth.2687.

(193) M. P. Backlund, M. D. Lew, A. S. Backer, S. J. Sahl and W. E. Moerner, *Chemphyschem : a European journal of chemical physics and physical chemistry*, 2014, **15**, 587–599, DOI: 10.1002/cphc.201300880.

(194) H. Deschout, F. Cella Zanacchi, M. Mlodzianoski, A. Diaspro, J. Bewersdorf, S. T. Hess and K. Braeckmans, *Nature methods*, 2014, **11**, 253–266, DOI: 10.1038/nmeth.2843.

(195) A. D. Edelstein, M. A. Tsuchida, N. Amodaj, H. Pinkard, R. D. Vale and N. Stuurman, *Journal of biological methods*, 2014, **1**, DOI: 10.14440/jbm.2014.36.

(196) U. Endesfelder, S. Malkusch, F. Fricke and M. Heilemann, *Histochemistry and cell biology*, 2014, **141**, 629–638, DOI: 10.1007/s00418-014-1192-3.

(197) M. Ovesný, P. Křížek, J. Borkovec, Z. Svindrych and G. M. Hagen, *Bioinformatics (Oxford, England)*, 2014, **30**, 2389–2390, DOI: 10.1093/bioinformatics/btu202.

(198) D. M. Patel and K. J. Green, *Cell communication & adhesion*, 2014, **21**, 109–128, DOI: 10.3109/15419061.2014.906533.

(199) W. Richtering and B. R. Saunders, *Soft matter*, 2014, **10**, 3695–3702, DOI: 10.1039/c4sm00208c.

(200) R. Schirhagl, K. Chang, M. Loretz and C. L. Degen, *Annual review of physical chemistry*, 2014, **65**, 83–105, DOI: 10.1146/annurev-physchem-040513-103659.

(201) Y. Shechtman, S. J. Sahl, A. S. Backer and W. E. Moerner, *Physical review letters*, 2014, **113**, 133902, DOI: 10.1103/PhysRevLett.113.133902.

(202) D. Suzuki, Y. Nagase, T. Kureha and T. Sato, *The journal of physical chemistry. B*, 2014, **118**, 2194–2204, DOI: 10.1021/jp410983x.

(203) K. Uhlig, H. Boerner, E. Wischerhoff, J.-F. Lutz, M. Jaeger, A. Laschewsky and C. Duschl, *Polymers*, 2014, **6**, 1164–1177, DOI: 10.3390/polym6041164.

(204) C. M. Winterflood and H. Ewers, *Chemphyschem : a European journal of chemical physics and physical chemistry*, 2014, **15**, 3447–3451, DOI: 10.1002/cphc.201402423.

(205) Q. M. Zhang, W. Xu and M. J. Serpe, *Angewandte Chemie (International ed. in English)*, 2014, **53**, 4827–4831, DOI: 10.1002/anie.201402641.

(206) A. von Appen, J. Kosinski, L. Sparks, A. Ori, A. L. DiGuilio, B. Vollmer, M.-T. Mackmull, N. Banterle, L. Parca, P. Kastritis, K. Buczak, S. Mosalaganti, W. Hagen, A. Andres-Pons, E. A. Lemke, P. Bork, W. Antonin, J. S. Glavy, K. H. Bui and M. Beck, *Nature*, 2015, **526**, 140–143, DOI: 10.1038/nature15381.

(207) S. Backes, M. U. Witt, E. Roeben, L. Kuhrts, S. Aleed, A. M. Schmidt and R. von Klitzing, *The journal of physical chemistry. B*, 2015, **119**, 12129–12137, DOI: 10.1021/acs.jpcb.5b03778.

(208) M. Booth, D. Andrade, D. Burke, B. Patton and M. Zurauskas, *Microscopy (Oxford, England)*, 2015, **64**, 251–261, DOI: 10.1093/jmicro/dfv033.

(209) F. Causa, A. Aliberti, A. M. Cusano, E. Battista and P. A. Netti, *Journal of the American Chemical Society*, 2015, **137**, 1758–1761, DOI: 10.1021/ja511644b.

(210) K. C. Clarke, S. N. Dunham and L. A. Lyon, *Chemistry of Materials*, 2015, **27**, 1391–1396, DOI: 10.1021/cm504649t.

(211) J. J. Crassous, A. M. Mihut, L. K. Månsson and P. Schurtenberger, *Nanoscale*, 2015, **7**, 15971–15982, DOI: 10.1039/c5nr03827h.

(212) F. Fricke, J. Beaudouin, R. Eils and M. Heilemann, *Scientific reports*, 2015, **5**, 14072, DOI: 10.1038/srep14072.

(213) Y. Ishitsuka, N. Savage, Y. Li, A. Bergs, N. Grün, D. Kohler, R. Donnelly, G. U. Nienhaus, R. Fischer and N. Takeshita, *Science advances*, 2015, **1**, e1500947, DOI: 10.1126/sciadv.1500947.

(214) H. Kempf, C. Kropp, R. Olmer, U. Martin and R. Zweigerdt, *Nature protocols*, 2015, **10**, 1345–1361, DOI: 10.1038/nprot.2015.089.

(215) M. Kettner, B. Göhler, H. Zacharias, D. Mishra, V. Kiran, R. Naaman, C. Fontanesi, D. H. Waldeck, S. Sęk, J. Pawłowski and J. Juhaniewicz, *The Journal of Physical Chemistry C*, 2015, **119**, 14542–14547, DOI: 10.1021/jp509974z.

(216) S. Konermann, M. D. Brigham, A. E. Trevino, J. Joung, O. O. Abudayyeh, C. Barcena, P. D. Hsu, N. Habib, J. S. Gootenberg, H. Nishimasu, O. Nureki and F. Zhang, *Nature*, 2015, **517**, 583–588, DOI: 10.1038/nature14136.

(217) H. Lee, D. Brinks and A. E. Cohen, *Optics express*, 2015, **23**, 28022–28030, DOI: 10.1364/OE.23.028022.

(218) D. Li, L. Shao, B.-C. Chen, X. Zhang, M. Zhang, B. Moses, D. E. Milkie, J. R. Beach, J. A. Hammer, M. Pasham, T. Kirchhausen, M. A. Baird, M. W. Davidson, P. Xu and E. Betzig, *Science (New York, N.Y.)*, 2015, **349**, aab3500, DOI: 10.1126/science.aab3500.

(219) M. A. Lifson, J. A. Carter and B. L. Miller, *Analytical chemistry*, 2015, **87**, 7887–7893, DOI: 10.1021/acs.analchem.5b01669.

(220) J. McCord, *EPL (Europhysics Letters)*, 2015, **48**, 333001, DOI: 10.1088/0022-3727/48/33/333001.

(221) O. Mergel, P. Wünnemann, U. Simon, A. Böker and F. A. Plamper, *Chemistry of Materials*, 2015, **27**, 7306–7312, DOI: 10.1021/acs.chemmater.5b02740.

(222) R. Naaman and D. H. Waldeck, *Annual review of physical chemistry*, 2015, **66**, 263–281, DOI: 10.1146/annurev-physchem-040214-121554.

(223) D. Sage, H. Kirshner, T. Pengo, N. Stuurman, J. Min, S. Manley and M. Unser, *Nature methods*, 2015, **12**, 717–724, DOI: 10.1038/nmeth.3442.

(224) Y. Shechtman, L. E. Weiss, A. S. Backer, S. J. Sahl and W. E. Moerner, *Nano letters*, 2015, **15**, 4194–4199, DOI: 10.1021/acs.nanolett.5b01396.

(225) B. Wedel, Dissertation, Universität Bielefeld, Bielefeld, 2015, https://pub.uni-bielefeld.de/record/2900093.

(226) D. R. Whelan and T. D. M. Bell, *Scientific reports*, 2015, **5**, 7924, DOI: 10.1038/srep07924.

(227) C. M. Winterflood, E. Platonova, D. Albrecht and H. Ewers, *Biophysical Journal*, 2015, **109**, 3–6, DOI: 10.1016/j.bpj.2015.05.026.

(228) J. Xu, K. F. Tehrani and P. Kner, *ACS nano*, 2015, **9**, 2917–2925, DOI: 10.1021/nn506952g.

(229) M. Zhang, J. Chen, J. Gao, Z. Wang, H. Xu, M. Cai, J. Jiang, Z. Tian and H. Wang, *Physical chemistry chemical physics : PCCP*, 2015, **17**, 6722–6727, DOI: 10.1039/C4CP05914J.

(230) A. Aloi, N. Vilanova, L. Albertazzi and I. K. Voets, *Nanoscale*, 2016, **8**, 8712–8716, DOI: 10.1039/c6nr00445h.

(231) V. O. Chagin, C. S. Casas-Delucchi, M. Reinhart, L. Schermelleh, Y. Markaki, A. Maiser, J. J. Bolius, A. Bensimon, M. Fillies, P. Domaing, Y. M. Rozanov, H. Leonhardt and M. C. Cardoso, *Nature communications*, 2016, **7**, 11231, DOI: 10.1038/ncomms11231.

(232) G. M. Conley, S. Nöjd, M. Braibanti, P. Schurtenberger and F. Scheffold, *Colloids and Surfaces A: Physicochemical and Engineering Aspects*, 2016, **499**, 18–23, DOI: 10.1016/j.colsurfa.2016.03.010.

(233) A. L. Efros and D. J. Nesbitt, *Nature nanotechnology*, 2016, **11**, 661–671, DOI: 10.1038/nnano.2016.140.

(234) A. P. H. Gelissen, A. Oppermann, T. Caumanns, P. Hebbeker, S. K. Turnhoff, R. Tiwari, S. Eisold, U. Simon, Y. Lu, J. Mayer, W. Richtering, A. Walther and D. Wöll, *Nano letters*, 2016, **16**, 7295–7301, DOI: 10.1021/acs.nanolett.6b03940.

(235) N. Gustafsson, S. Culley, G. Ashdown, D. M. Owen, P. M. Pereira and R. Henriques, *Nature communications*, 2016, **7**, 12471, DOI: 10.1038/ncomms12471.

(236) W. R. Legant, L. Shao, J. B. Grimm, T. A. Brown, D. E. Milkie, B. B. Avants, L. D. Lavis and E. Betzig, *Nature methods*, 2016, **13**, 359–365, DOI: 10.1038/nmeth.3797.

(237) D. Leyton-Puig, K. M. Kedziora, T. Isogai, B. van den Broek, K. Jalink and M. Innocenti, *Biology open*, 2016, **5**, 1001–1009, DOI: 10.1242/bio.019570.

(238) P. Y. Liu, L. K. Chin, W. Ser, H. F. Chen, C.-M. Hsieh, C.-H. Lee, K.-B. Sung, T. C. Ayi, P. H. Yap, B. Liedberg, K. Wang, T. Bourouina and Y. Leprince-Wang, *Lab on a chip*, 2016, **16**, 634–644, DOI: 10.1039/c5lc01445j.

(239) A. Mazouchi and J. N. Milstein, *Bioinformatics (Oxford, England)*, 2016, **32**, 747–754, DOI: 10.1093/bioinformatics/btv630.

(240) P. C. Mondal, C. Fontanesi, D. H. Waldeck and R. Naaman, *Accounts of chemical research*, 2016, **49**, 2560–2568, DOI: 10.1021/acs.accounts.6b00446.

(241) P. C. Mondal, P. Roy, D. Kim, E. E. Fullerton, H. Cohen and R. Naaman, *Nano letters*, 2016, **16**, 2806–2811, DOI: 10.1021/acs.nanolett.6b00582.

(242) M. Müller, V. Mönkemöller, S. Hennig, W. Hübner and T. Huser, *Nature communications*, 2016, **7**, 10980, DOI: 10.1038/ncomms10980.

(243) L. Nahidiazar, A. V. Agronskaia, J. Broertjes, B. van den Broek and K. Jalink, *PLoS ONE*, 2016, **11**, DOI: 10.1371/journal.pone.0158884.

(244) O. Nevskyi, D. Sysoiev, A. Oppermann, T. Huhn and D. Wöll, *Angewandte Chemie (International ed. in English)*, 2016, **55**, 12698–12702, DOI: 10.1002/anie.201606791.

(245) S. V. Pageon, P. R. Nicovich, M. Mollazade, T. Tabarin and K. Gaus, *Molecular biology of the cell*, 2016, **27**, 3627–3636, DOI: 10.1091/mbc.E16-07-0478.

(246) D. I. Phua, K. Herman, A. Balaceanu, J. Zakrevski and A. Pich, *Langmuir : the ACS journal of surfaces and colloids*, 2016, **32**, 3867–3879, DOI: 10.1021/acs.langmuir.6b00241.

(247) S. d. Quinn, A. Rafferty, E. Dick, M. J. Morten, F. J. Kettles, C. Knox, M. Murrie and S. W. Magennis, *The Journal of Physical Chemistry C*, 2016, **120**, 19487–19491, DOI: 10.1021/acs.jpcc.6b07779.

(248) P. Roy, N. Kantor-Uriel, D. Mishra, S. Dutta, N. Friedman, M. Sheves and R. Naaman, *ACS nano*, 2016, **10**, 4525–4531, DOI: 10.1021/acsnano.6b00333.

(249) S. N. Stahley, E. I. Bartle, C. E. Atkinson, A. P. Kowalczyk and A. L. Mattheyses, *Journal of cell science*, 2016, **129**, 2897–2904, DOI: 10.1242/jcs.185785.

(250) S. N. Stahley, M. F. Warren, R. J. Feldman, R. A. Swerlick, A. L. Mattheyses and A. P. Kowalczyk, *The Journal of investigative dermatology*, 2016, **136**, 59–66, DOI: 10.1038/JID.2015.353.

(251) K. Uhlig, T. Wegener, J. He, M. Zeiser, J. Bookhold, I. Dewald, N. Godino, M. Jaeger, T. Hellweg, A. Fery and C. Duschl, *Biomacromolecules*, 2016, **17**, 1110–1116, DOI: 10.1021/acs.biomac.5b01728.

(252) B. Wedel, Y. Hertle, O. Wrede, J. Bookhold and T. Hellweg, *Polymers*, 2016, **8**, DOI: 10.3390/polym8040162.

(253) J. Wei, Y. Li and T. Ngai, *Colloids and Surfaces A: Physicochemical and Engineering Aspects*, 2016, **489**, 122–127, DOI: 10.1016/j.colsurfa.2015.10.042.

(254) Q. M. Zhang, W. Wang, Y.-Q. Su, E. J. M. Hensen and M. J. Serpe, *Chemistry of Materials*, 2016, **28**, 259–265.

(255) A. C. Aragonès, E. Medina, M. Ferrer-Huerta, N. Gimeno, M. Teixidó, J. L. Palma, N. Tao, J. M. Ugalde, E. Giralt, I. Díez-Pérez and V. Mujica, *Small (Weinheim an der Bergstrasse, Germany)*, 2017, **13**, DOI: 10.1002/smll.201602519.

(256) H. P. Babcock and X. Zhuang, *Scientific reports*, 2017, **7**, 552, DOI: 10.1038/s41598-017-00622-w.

(257) F. Balzarotti, Y. Eilers, K. C. Gwosch, A. H. Gynnå, V. Westphal, F. D. Stefani, J. Elf and S. W. Hell, *Science (New York, N.Y.)*, 2017, **355**, 606–612, DOI: 10.1126/science.aak9913.

(258) S. Bergmann, V. Mönkemöller and T. Huser, *Physical chemistry chemical physics : PCCP*, 2017, **19**, 4887–4890, DOI: 10.1039/c6cp05108a.

(259) N. Boon and P. Schurtenberger, *Physical chemistry chemical physics : PCCP*, 2017, **19**, 23740–23746, DOI: 10.1039/c7cp02434g.

(260) G. M. Conley, P. Aebischer, S. Nöjd, P. Schurtenberger and F. Scheffold, *Science advances*, 2017, **3**, e1700969, DOI: 10.1126/sciadv.1700969.

(261) M. Cors, O. Wrede, A.-C. Genix, D. Anselmetti, J. Oberdisse and T. Hellweg, *Langmuir : the ACS journal of surfaces and colloids*, 2017, **33**, 6804–6811, DOI: 10.1021/acs.langmuir.7b01199.

(262) R. Diekmann, K. Till, M. Müller, M. Simonis, M. Schüttpelz and T. Huser, *Scientific reports*, 2017, **7**, 14425, DOI: 10.1038/s41598-017-14762-6.

(263) C. Franke, M. Sauer and S. van de Linde, *Nature methods*, 2017, **14**, 41–44, DOI: 10.1038/nmeth.4073.

(264) X. Gong, X. Gao and L. Jiang, *Advanced materials (Deerfield Beach, Fla.)*, 2017, **29**, DOI: 10.1002/adma.201703002.

(265) R. Heintzmann and T. Huser, *Chemical reviews*, 2017, **117**, 13890–13908, DOI: 10.1021/acs.chemrev.7b00218.

(266) N. Ji, *Nature methods*, 2017, **14**, 374–380, DOI: 10.1038/nmeth.4218.

(267) Y. Ke, X. Wen, D. Zhao, R. Che, Q. Xiong and Y. Long, *ACS nano*, 2017, **11**, 7542–7551, DOI: 10.1021/acsnano.7b02232.

(268) A. Kumar, E. Capua, M. K. Kesharwani, J. M. L. Martin, E. Sitbon, D. H. Waldeck and R. Naaman, *Proceedings of the National Academy of Sciences of the United States of America*, 2017, **114**, 2474–2478, DOI: 10.1073/pnas.1611467114.

(269) J. Liang, F. Teng, T.-M. Chou and M. Libera, *Polymer*, 2017, **116**, 1–4, DOI: 10.1016/j.polymer.2017.03.050.

(270) S. Liu, M. J. Mlodzianoski, Z. Hu, Y. Ren, K. McElmurry, D. M. Suter and F. Huang, *Nature methods*, 2017, **14**, 760–761, DOI: 10.1038/nmeth.4379.

(271) F. A. Plamper and W. Richtering, *Accounts of chemical research*, 2017, **50**, 131–140, DOI: 10.1021/acs.accounts.6b00544.

(272) A. Ruba, W. Luo, J. Kelich and W. Yang, *Obtaining 3D Super-resolution Information from 2D Super-resolution Images through a 2D-to-3D Transformation Algorithm*, 2017, vol. 19, DOI: 10.1101/188060.

(273) X. Zhou, J. Nie and B. Du, *ACS applied materials & interfaces*, 2017, **9**, 20913–20921, DOI: 10.1021/acsami.7b06337.

(274) A. Aristov, B. Lelandais, E. Rensen and C. Zimmer, *Nature communications*, 2018, **9**, 2409, DOI: 10.1038/s41467-018-04709-4.

(275) H. P. Babcock, *Scientific reports*, 2018, **8**, 1726, DOI: 10.1038/s41598-018-19981-z.

(276) S. Bergmann, O. Wrede, T. Huser and T. Hellweg, *Physical chemistry chemical physics : PCCP*, 2018, **20**, 5074–5083, DOI: 10.1039/c7cp07648g.

(277) A. M. Bittel, I. S. Saldivar, N. J. Dolman, X. Nan and S. L. Gibbs, *PLoS ONE*, 2018, **13**, e0206104, DOI: 10.1371/journal.pone.0206104.

(278) C. Cabriel, N. Bourg, G. Dupuis and S. Lévêque-Fort, *Optics letters*, 2018, **43**, 174–177, DOI: 10.1364/OL.43.000174.

(279) H. D. Devalla and R. Passier, *Science translational medicine*, 2018, **10**, DOI: 10.1126/scitranslmed.aah5457.

(280) Y. Guo, Di Li, S. Zhang, Y. Yang, J.-J. Liu, X. Wang, C. Liu, D. E. Milkie, R. P. Moore, U. S. Tulu, D. P. Kiehart, J. Hu, J. Lippincott-Schwartz, E. Betzig and D. Li, *Cell*, 2018, **175**, 1430–1442.e17, DOI: 10.1016/j.cell.2018.09.057.

(281) T. M. P. Hartwich, K. K. H. Chung, L. Schroeder, J. Bewersdorf, C. Soeller and D. Baddeley, *A stable, high refractive index, switching buffer for super-resolution imaging*, 2018, DOI: 10.1101/465492.

(282) A. A. Karanastasis, Y. Zhang, G. S. Kenath, M. D. Lessard, J. Bewersdorf and C. K. Ullal, *Materials horizons*, 2018, **5**, 1130–1136, DOI: 10.1039/c8mh00644j.

(283) M. Kettner, V. V. Maslyuk, D. Nürenberg, J. Seibel, R. Gutierrez, G. Cuniberti, K.-H. Ernst and H. Zacharias, *The journal of physical chemistry letters*, 2018, **9**, 2025–2030, DOI: 10.1021/acs.jpclett.8b00208.

(284) N. Kilian, A. Goryaynov, M. D. Lessard, G. Hooker, D. Toomre, J. E. Rothman and J. Bewersdorf, *Nature methods*, 2018, **15**, 755–756, DOI: 10.1038/s41592-018-0145-5.

(285) Y. Li, M. Mund, P. Hoess, J. Deschamps, U. Matti, B. Nijmeijer, V. J. Sabinina, J. Ellenberg, I. Schoen and J. Ries, *Nature methods*, 2018, **15**, 367–369, DOI: 10.1038/nmeth.4661.

(286) K. J. A. Martens, A. N. Bader, S. Baas, B. Rieger and J. Hohlbein, *The Journal of Chemical Physics*, 2018, **148**, 123311, DOI: 10.1063/1.5005899.

(287) P. C. Mondal, W. Mtangi and C. Fontanesi, *Small Methods*, 2018, **2**, 1700313, DOI: 10.1002/smtd.201700313.

(288) O. Nevskyi, D. Sysoiev, J. Dreier, S. C. Stein, A. Oppermann, F. Lemken, T. Janke, J. Enderlein, I. Testa, T. Huhn and D. Wöll, *Small (Weinheim an der Bergstrasse, Germany)*, 2018, **14**, DOI: 10.1002/smll.201703333.

(289) K. N. Richter, N. H. Revelo, K. J. Seitz, M. S. Helm, D. Sarkar, R. S. Saleeb, E. D'Este, J. Eberle, E. Wagner, C. Vogl, D. F. Lazaro, F. Richter, J. Coy-Vergara, G. Coceano, E. S. Boyden, R. R. Duncan, S. W. Hell, M. A. Lauterbach, S. E. Lehnart, T. Moser, T. F. Outeiro, P. Rehling, B. Schwappach, I. Testa, B. Zapiec and S. O. Rizzoli, *The EMBO journal*, 2018, **37**, 139–159, DOI: 10.15252/embj.201695709.

(290) E. Siemes, O. Nevskyi, D. Sysoiev, S. K. Turnhoff, A. Oppermann, T. Huhn, W. Richtering and D. Wöll, *Angewandte Chemie (International ed. in English)*, 2018, **57**, 12280–12284, DOI: 10.1002/anie.201807741.

(291) M. Siemons, C. N. Hulleman, R. Ø. Thorsen, C. S. Smith and S. Stallinga, *Optics express*, 2018, **26**, 8397–8416, DOI: 10.1364/OE.26.008397.

(292) M. Sivaguru, M. A. Urban, G. Fried, C. J. Wesseln, L. Mander and S. W. Punyasena, *Microscopy research and technique*, 2018, **81**, 101–114, DOI: 10.1002/jemt.22732.

(293) F. Tassinari, D. R. Jayarathna, N. Kantor-Uriel, K. L. Davis, V. Varade, C. Achim and R. Naaman, *Advanced materials (Deerfield Beach, Fla.)*, 2018, **30**, e1706423, DOI: 10.1002/adma.201706423.

(294) Thermo Fisher Scientific, *Fluorescence SpectraViewer*, ed. Thermo Fisher Scientific, 2018.

(295) K. Uhlig, T. Wegener, Y. Hertle, J. Bookhold, M. Jaeger, T. Hellweg, A. Fery and C. Duschl, *Polymers*, 2018, **10**, DOI: 10.3390/polym10060656.

(296) V. Varade, T. Markus, K. Vankayala, N. Friedman, M. Sheves, D. H. Waldeck and R. Naaman, *Physical chemistry chemical physics : PCCP*, 2018, **20**, 1091–1097, DOI: 10.1039/c7cp06771b.

(297) O. Wrede, Y. Reimann, S. Lülsdorf, D. Emmrich, K. Schneider, A. J. Schmid, D. Zauser, Y. Hannappel, A. Beyer, R. Schweins, A. Gölzhäuser, T. Hellweg and T. Sottmann, *Scientific reports*, 2018, **8**, 13781, DOI: 10.1038/s41598-018-31976-4.

(298) D. Yang, M. Viitasuo, F. Pooch, H. Tenhu and S. Hietala, *Polymer Chemistry*, 2018, **9**, 517–524, DOI: 10.1039/C7PY01950E.

(299) W. Zhang, K. Banerjee-Ghosh, F. Tassinari and R. Naaman, *ACS Energy Letters*, 2018, **3**, 2308–2313, DOI: 10.1021/acsenergylett.8b01454.

(300) *Spectroscopy and Dynamics of Single Molecules*, ed. Carey K. Johnson, Elsevier, 2019.

(301) G. M. Conley, C. Zhang, P. Aebischer, J. L. Harden and F. Scheffold, *Nature communications*, 2019, **10**, 2436, DOI: 10.1038/s41467-019-10181-5.

(302) M. Cors, O. Wrede, L. Wiehemeier, A. Feoktystov, F. Cousin, T. Hellweg and J. Oberdisse, *Scientific reports*, 2019, **9**, 13812, DOI: 10.1038/s41598-019-50164-6.

(303) S. Dalum and P. Hedegård, *Nano letters*, 2019, **19**, 5253–5259, DOI: 10.1021/acs.nanolett.9b01707.

(304) A. Descloux, K. S. Grußmayer and A. Radenovic, *Nature methods*, 2019, **16**, 918–924, DOI: 10.1038/s41592-019-0515-7.

(305) M. S. Dietz and M. Heilemann, *Nanoscale*, 2019, **11**, 17981–17991, DOI: 10.1039/C9NR06364A.

(306) L. Etchenausia, E. Villar-Alvarez, J. Forcada, M. Save and P. Taboada, *Materials Science and Engineering: C*, 2019, **104**, 109871, DOI: 10.1016/j.msec.2019.109871.

(307) K. C. Gwosch, J. K. Pape, F. Balzarotti, P. Hoess, J. Ellenberg, J. Ries and S. W. Hell, *MINFLUX nanoscopy delivers multicolor nanometer 3D-resolution in (living) cells*, 2019, vol. 121, DOI: 10.1101/734251.

(308) L. Hoppe Alvarez, S. Eisold, R. A. Gumerov, M. Strauch, A. A. Rudov, P. Lenssen, D. Merhof, I. I. Potemkin, U. Simon and D. Wöll, *Nano letters*, 2019, **2019**, DOI: 10.1021/acs.nanolett.9b03688.

(309) A. Jimenez, K. Friedl and C. Leterrier, *Methods (San Diego, Calif.)*, 2019, DOI: 10.1016/j.ymeth.2019.05.008.

(310) M. Karg, A. Pich, T. Hellweg, T. Hoare, L. A. Lyon, J. J. Crassous, D. Suzuki, R. A. Gumerov, S. Schneider, I. I. Potemkin and W. Richtering, *Langmuir : the ACS journal of surfaces and colloids*, 2019, **35**, 6231–6255, DOI: 10.1021/acs.langmuir.8b04304.

(311) Y. Li, Y.-L. Wu, P. Hoess, M. Mund and J. Ries, *Biomedical Optics Express*, 2019, **10**, 2708, DOI: 10.1364/BOE.10.002708.

(312) A. Markwirth, M. Lachetta, V. Mönkemöller, R. Heintzmann, W. Hübner, T. Huser and M. Müller, *Nature communications*, 2019, **10**, 4315, DOI: 10.1038/s41467-019-12165-x.

(313) B. Moeyaert, W. Vandenberg and P. Dedecker, *SOFIevaluator: a strategy for the quantitative quality assessment of SOFI data*, 2019, vol. 27, DOI: 10.1101/802199.

(314) R. Naaman, Y. Paltiel and D. H. Waldeck, *Nature Reviews Chemistry*, 2019, **3**, 250–260, DOI: 10.1038/s41570-019-0087-1.

(315) J. P. Newsom, K. A. Payne and M. D. Krebs, *Acta biomaterialia*, 2019, **88**, 32–41, DOI: 10.1016/j.actbio.2019.02.011.

(316) C. S. O'Bryan, C. P. Kabb, B. S. Sumerlin and T. E. Angelini, *ACS Applied Bio Materials*, 2019, **2**, 1509–1517, DOI: 10.1021/acsabm.8b00784.

(317) A. Purohit, S. P. Centeno, S. K. Wypysek, W. Richtering and D. Wöll, *Chemical Science*, 2019, **50**, 131, DOI: 10.1039/C9SC03373D.

(318) D. Sage, T.-A. Pham, H. Babcock, T. Lukes, T. Pengo, J. Chao, R. Velmurugan, A. Herbert, A. Agrawal, S. Colabrese, A. Wheeler, A. Archetti, B. Rieger, R. Ober, G. M. Hagen, J.-B. Sibarita, J. Ries, R. Henriques, M. Unser and S. Holden, *Nature Methods*, 2019, **313**, 1642, DOI: 10.1038/s41592-019-0364-4.

(319) A. Sandmeyer, M. Lachetta, H. Sandmeyer, W. Hübner, T. Huser and M. Müller, *DMD-based super-resolution structured illumination microscopy visualizes live cell dynamics at high speed and low cost*, 2019, vol. 9, DOI: 10.1101/797670.

(320) L. Schermelleh, A. Ferrand, T. Huser, C. Eggeling, M. Sauer, O. Biehlmaier and G. P. C. Drummen, *Nature cell biology*, 2019, **21**, 72–84, DOI: 10.1038/s41556-018-0251-8.

(321) M. J. Serpe, *Nature*, 2019, **565**, 438–439, DOI: 10.1038/d41586-019-00084-2.

(322) J. V. Thevathasan, M. Kahnwald, K. Cieśliński, P. Hoess, S. K. Peneti, M. Reitberger, D. Heid, K. C. Kasuba, S. J. Hoerner, Y. Li, Y.-L. Wu, M. Mund, U. Matti, P. M. Pereira, R. Henriques, B. Nijmeijer, M. Kueblbeck, V. J. Sabinina, J. Ellenberg and J. Ries, *Nature methods*, 2019, **16**, 1045–1053, DOI: 10.1038/s41592-019-0574-9.

(323) L. Wiehemeier, M. Cors, O. Wrede, J. Oberdisse, T. Hellweg and T. Kottke, *Physical chemistry chemical physics : PCCP*, 2019, **21**, 572–580, DOI: 10.1039/c8cp05911j.

(324) A. M. Wojciechowski, P. N. M. Mrózek, K. Sycz, A. Kruk, M. Ficek, M. Głowacki, R. Bogdanowicz and W. Gawlik, *Materials (Basel, Switzerland)*, 2019, **12**, DOI: 10.3390/ma12182951.

(325) X. Zhou, F. Chen, H. Lu, L. Kong, S. Zhang, W. Zhang, J. Nie, B. Du and X. Wang, *Industrial & Engineering Chemistry Research*, 2019, **58**, 10922–10930, DOI: 10.1021/acs.iecr.9b01904.

(326) P. Otto, S. Bergmann, A. Sandmeyer, M. Dirksen, O. Wrede, T. Hellweg and T. Huser, *Nanoscale Adv*, 2020, -, DOI: 10.1039/C9NA00670B.

A. Appendix

A.1. Super-resolution optical microscopy resolves network morphology of smart colloidal microgels

A.1.1. Microgel synthesis

N-isopropylacrylamide (NIPAM, TCI, Tokyo, Japan) based microgels with different cross-linker contents were prepared under usage of the established surfactant free precipitation polymerization [49]. 11.55 mmol of the monomer together with the respective cross-linker amount (0.58, 0.87 and 1.16 mmol of N,N'-methylenbisacrylamide (BIS, Sigma-Aldrich, St-Louis, U.S.A.)) were added to 150 ml purified water. The solution was heated to 70 °C and purged with nitrogen gas under continuous stirring inside a 250 ml three neck flask. The reaction was started after 1 h equilibration with the addition of 1 ml of a 0.4 M ammonium peroxidisulfate (APS, Sigma-Aldrich, USA) to the solution. After 4 h the reaction mixture was cooled to room temperature and left stirring overnight.

A.1.2. Macrogel synthesis

The NIPAM based macrogel with a cross-linker content of 5.0 mol% was synthesized via the synthetic approach of Tanaka.[27] 3.9 ml of an aqueous solution containing NIPAM, BIS and APS was purged with nitrogen at 0 °C for 1 h. Afterwards this solution was combined with 0.1 ml of a 0.025 mM tetramethylethylendiamin (TMEDA, Sigma-Aldrich, USA) in water solution inside a self-built heating block having a rectangular inner shape ($10 \cdot 10 \cdot 40$ mm) at 20 °C. The finished product was removed from the apparatus after 1 h and put into purified water. The solvent was exchanged 5 times to remove impurities.

A.1.3. Fluorescent labeling and microgel deposition

The synthesized polymer colloids with 5.0 %, 7.5 % and 10 % *N*,*N*'-methylenebisacrylamide (BIS) (Sigma-Aldrich, USA) were added to rhodamine 6G (R6G) in purified water (Arium® pro VF system, Satorius AG, Göttingen, Germany) solution (1 mM) leading to a final concentration of 0.5 % (m/m) of the microgels with 100 μM R6G. Multiple different fluorophores were tested at the beginning of

these experiments, but only R6G was found to be able to penetrate the whole polymer network with minimal, but still sufficiently strong interactions to make the *d*STORM experiments possible. Storing the microgel dye solution for 24 h in a light protected environment at room temperature resulted in dye saturation of the particles. Afterwards the microgel in dye solution was diluted by a factor of 5 (0.1 % microgel (m/m), 0.2 mM dye). # 1.5 coverslips (Menzel Gläser, Thermofisher Scientific) were cleaned in a plasma cleaner (0.4 mbar O_2) for 30 min and afterwards were sonicated in 2 % (v/v) Hellmanex III solution (Hellma GmbH) at room temperature for 30 min. Remaining Hellmanex solution was removed by a continuous water flow while spinning at high velocities (approximately 10 s) from both sides. Before mounting the microgels, the cleaned and washed coverglass was coated with a few nm thin polyethylenimine (PEI) film. The microgel R6G solution is pipetted on the PEI coated coverlsip until the entire coverslip was covered. After a waiting time of 30 min, the sample was spin cast at 500 rpm for 15 min. Free dye is removed by washing twice with water.

A.1.4. SoMaCoFit

Before fitting the localization data with SoMaCoFit [234][i], the data was normalized to the sum of 1. This was recommended in the SoMaCoFit manual to achieve comparable results in the 3D density ρ_{3D} between different measurements. For fitting of the 2D data the fuzzy sphere model was chosen and all fitting parameters were free. After calculating the 2D fit the data was regularized and inverted. To find the optimal regularization parameter λ, the minimum in the provided generalized cross validation was chosen. For the data $\lambda = 3.8614$ showed the minimal value. For small regularization values ρ_{3D} deviates strong from the expected distribution in the microgels (figures A1.1-A1.3).

[i] SoMaCoFit downloadable from: `https://publications.rwth-aachen.de/record/670555/`

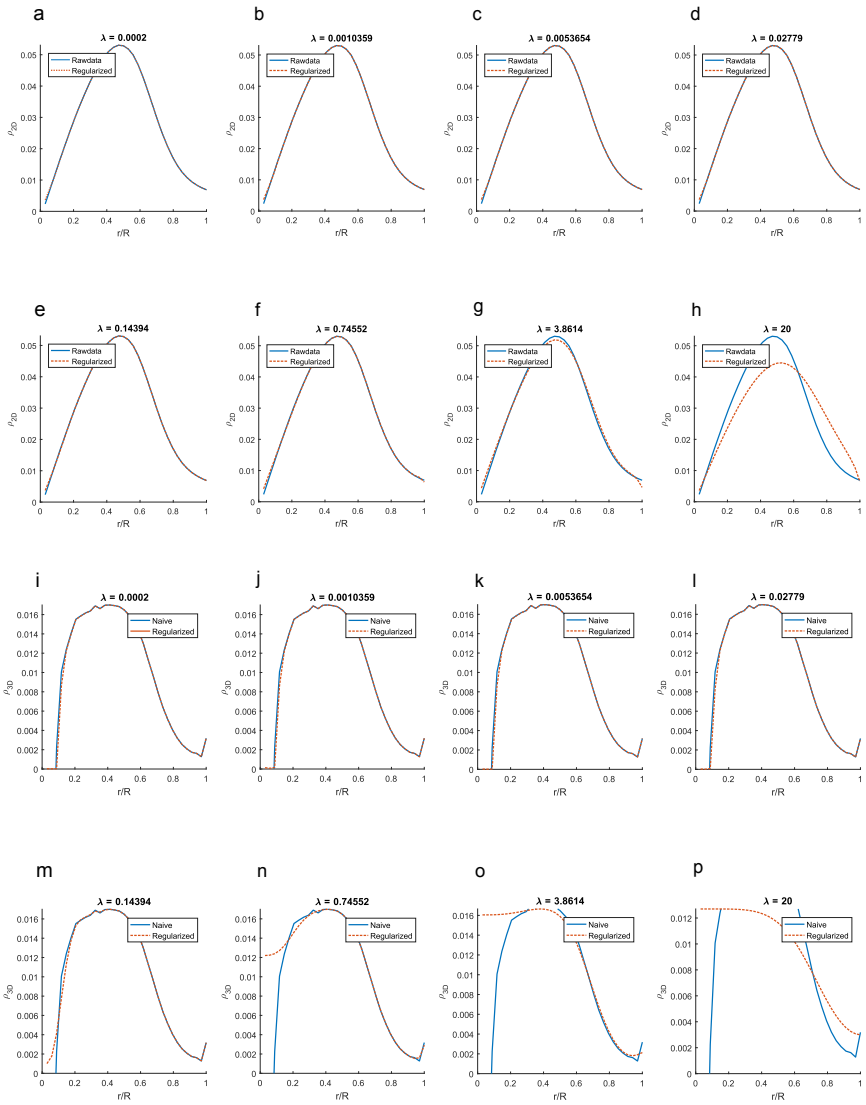

Figure A1.1.: SoMaCoFit was used to calculate the 3D profile density from the data of 5.0 mol% BIS microgels. As a result the software calculates the normalized 2D (figure A1.1 **a** to **h**) and 3D density (figure A1.1 **i** to **p**) for different regularizations λ of the given data. For a stronger regularization ($\lambda > 0.74552$) the data was smoothed to a high extend and especially close to the microgel centers the model differs strongly from the measured data.

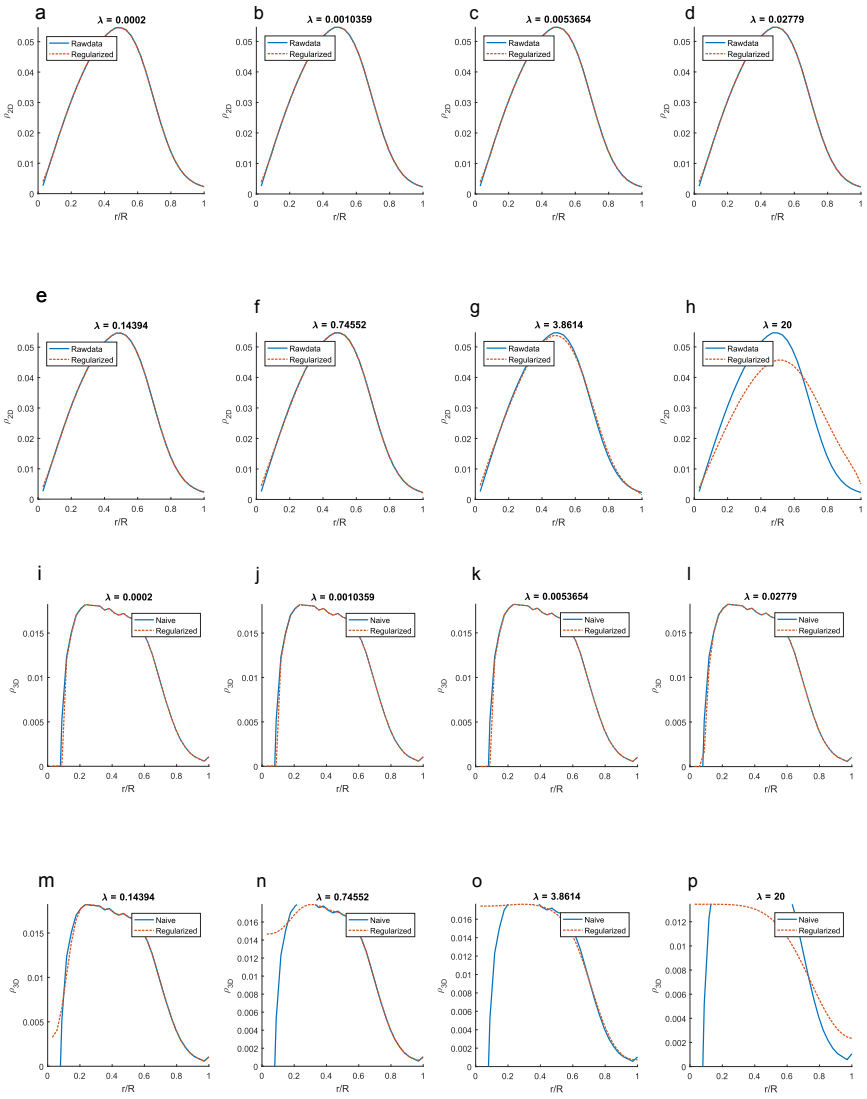

Figure A1.2.: SoMaCoFit is used to calculate the 3D profile density from thw data of 7.5 mol% BIS microgels. As a result the software calculates the normalized 2D (figure A1.2 **a** to **h**) and 3D density (figure A1.2 **i** to **p**) for different regularizations λ of the given data. For a stronger regularization ($\lambda > 0.74552$) the data was smoothed to a high extend and especially close to the microgel centers the model differs strongly from the measured data.

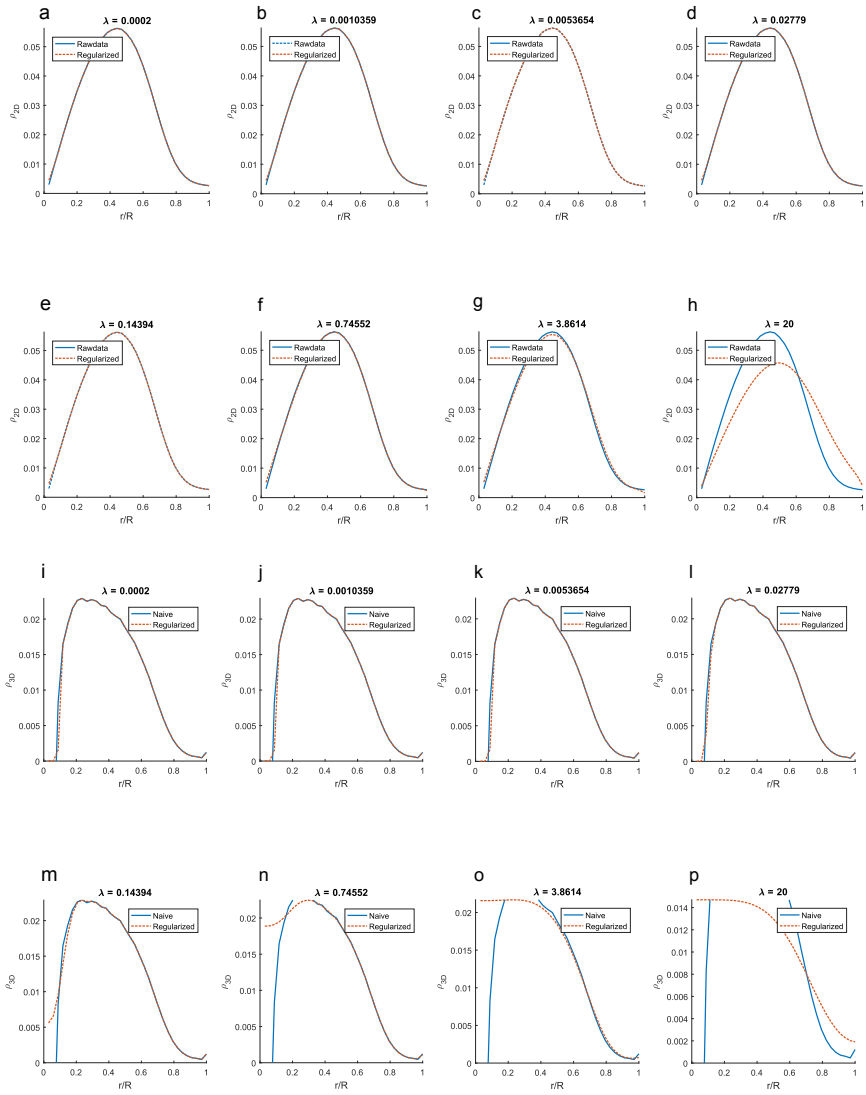

Figure A1.3.: SoMaCoFit is used to calculate the 3D profile density from thw data of 10 mol% BIS microgels. As a result the software calculates the normalized 2D (figure A1.3 **a** to **h**) and 3D density (figure A1.3 **i** to **p**) for different regularizations λ of the given data. For a stronger regularization ($\lambda > 0.74552$) the data was smoothed to a high extend and especially close to the microgel centers the model differs strongly from the measured data.

A.2. Smart microgels investigated by super-resolution fluorescence microscopy: Influence of the monomer structure on the particle morphology

A.2.1. Microgel synthesis

The microgel particles were prepared using an established precipitation polymerisation procedure [252] based on work by Pelton et al. [23]. 11.55 mmol were used of the respective monomer, together with a varying amount of cross-linker (0.58, 0.87 and 1.16 mmol) in a 150 ml ultra-pure water based synthesis. The polymerisation was started by adding an ammonium persulfate (APS) solution (total amount of APS: 0.4 mmol) after an equilibration period of 1 h where the solution was heated to 70 °C and purged using nitrogen gas. The reaction ran for 4 h at increased temperatures and was kept stirring at room temperature overnight. The purified particles were achieved after 5 centrifugation-decantation-redispersion cycles.

A.2.2. Fluorescent labeling and microgel deposition

The synthesized polymer colloids with 5.0%, 7.5% and 10% *N*,*N*'-methylenebisacrylamide (BIS) (Sigma-Aldrich, USA) were added to R6G in purified water (Arium® pro VF system, Satorius AG, Germany) solution (1 mM) led to a final concentration of 0.5 % (m/m) of the microgels with 100 μM R6G. Storing the microgel dye solution for at least 24 h in a light protected environment at room temperature results in dye saturation of the particles. Afterwards the microgel in dye solution was diluted by a factor of 5 (0.1 % microgel (m/m), 0.2 mM dye). # 1.5 coverslips (Menzel Gläser, Thermofisher Scientific) were cleaned in a plasma cleaner (0.4 mbar O_2) for 30 min and afterwards were sonicated in 2 % (v/v) Hellmanex III solution (Hellma GmbH, Germany) at room temperature for 30 min. Remaining Hellmanex solution was removed by a continuous water flow while spinning at high velocities (approximately 10 s) from both sides. Before mounting the microgels, the cleaned and washed coverslip is coated with a few nm thin polyethylenimine (PEI) film. The microgel R6G solution was pipetted on the PEI coated coverslip until the entire coverslip is covered. After a waiting time of 30 min, the sample is spin cast at 500 rpm for 15 min. Free dye is removed by washing twice with water.

A.2.3. Photon correlation spectroscopy

The photon correlation spectroscopy measurements were performed on a custom built fixed angle setup (scattering angle: 45°) utilizing a Helium-Neon-Laser (632.8 nm, 21 mW, Thorlabs, Newton, USA) and two photomultipiers (ALV/SO-SIPD, ALV-GmbH, Germany) in a pseudo-cross correlation configuration. The

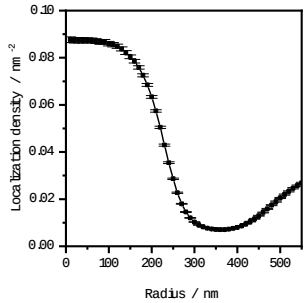

Figure A2.4.: This 2D localization density measurement of NIPMAM cross-linked with 10 mol% BIS exceeds the measured hydrodynamic radius of approximately 400 nm. It can be seen that after 350 nm the localization density increases. This can be attributed to the background of free diffusing dyes in the imaging buffer.

signal was correlated with an ALV-6010 multiple-tau correlator (ALV-GmbH, Germany) and analyzed using an inverse Laplace transformation with the CONTIN algorithm [19, 20]. The temperature was controlled via a thermostat (Phoenix II, Thermo Fisher Scientific, USA togerther with Haake C25P, Thermo Fisher Scientific, USA). The sample was equilibrated for 25 minutes inside the decaline filled refractive index matching bath.

A.3. Resolving the internal morphology of core-shell microgels with super-resolution fluorescence microscopy

A.3.1. Syntheses

The microgel syntheses are well established precipitation polymerizations performed under nitrogen gas with purified water.[23] The syntheses for the PNIPMAM core particles and of the shell around these collapsed cores are described in the following.

Core microgels made of PNIPMAM

For the core particle synthesis the cross-linker N, N'-methylenbisacrylamide (BIS, 3.85 mmol, Sigma-Aldrich, USA), sodium dodecyl sulfate (SDS, 0.49 mmol, Carl Roth, Germany) and 500 ml purified water were mixed in a 1 l three- neck

flask, heated up to 70 °C and stirred for 90 minutes while purged with N_2. After 85 minutes the monomer *N*-isopropylmethacrylamide (NIPMAM, 38.5 mmol, Sigma Aldrich, USA) was added. The polymerization was initiated by ammoniumpersulfate (APS, 0.31 g, ≥ 98 %, Sigma Aldrich, USA). The solution was stirred at 70 °C for additional 4 hours at 300 rpm. Afterwards it was cooled down to room temperature and stirred over night.

The particles were purified by five repetitions of centrifugation (Beckman-Coulter Avanti™J-301 Centrifuge, rotor: JA-30.50, USA, 15000 rpm (27216 G), 20 °C, 30 minutes), decantation and redispersion with purified water.

Core-shell particles

The core-shell particles were synthesized with three different nominal shell thicknesses (thin, intermediate and thick) by precipitating the PNNPAM shell on the collapsed core of PNIPMAM [179, 261].

For the shell synthesis a 500 ml three-neck flask was used. For the PNIPMAM-core particles (0.15 wt%), *N*-n-propylacrylamide (NNPAM, 4.15 mmol, 8.25 mmol and 12.45 mmol, synthesis via Schotten-Baumann reaction [116]), BIS (0.08 mmol (thin), 0.16 mmol (intermediate) and 0.25 mmol (thick)), SDS (0.17 mmol) and 150 ml water were mixed. The solution was heated up to 70 °C and stirred for 75 minutes at 400 rpm. The reaction was initialized by addition of APS (0.094 g). Subsequently, the mixture was kept at 70 °C and stirred for 4 h. Afterwards the flask was cooled down to room temperature and got stirred over night. The core-shell particles were purified in the same way as the core-only particles.

A.3.2. Photon correlation spectroscopy

The photon correlation spectroscopy measurements were performed on a custom built fixed angle setup (scattering angle: 45 °) utilizing a Helium-Neon-Laser (632.8 nm, 21 mW, Thorlabs, USA) and two photomultipliers (ALV/SO-SIPD, ALV-GmbH, Langen, Germany) in a pseudo-cross correlation configuration. The signal was correlated with an ALV-6010 multiple-tau correlator (ALV-GmbH, Germany) and analyzed using an inverse Laplace transformation wit the CONTIN algorithm by S. Provencher [19, 20]. The temperature was controlled via a thermostat (Phoenix II, Thermo Fisher Scientific, USA together with Haake C25P, Thermo Fisher Scientific, USA). The samples were placed in a decalin filled refractive index matching bath which is equilibrated at the desired temperature for 25 minutes.

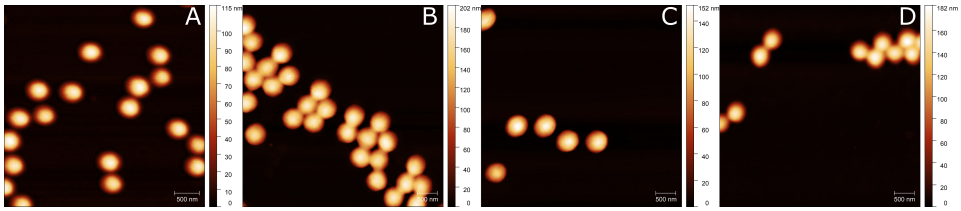

Figure A3.5.: Atomic force microscopy images of core-only microgels (**A**) and core-shell microgels with thin (**B**), intermediate (**C**) and thick (**D**) shells.

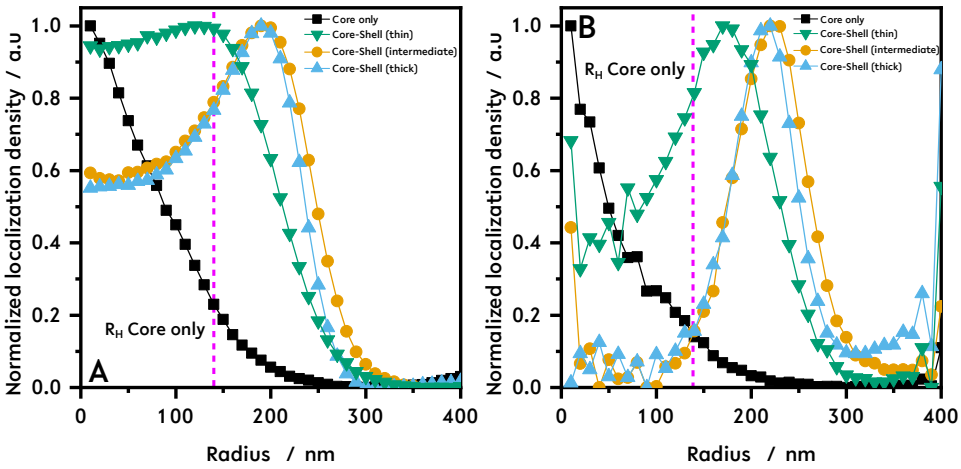

Figure A3.6.: In addition to the 2D- and 3D localization densities shown in figure 5.6 **A** and **B** shows the localization density normalized to values between zero and one.

A.3.3. Atomic force microscopy

All measurements were performed on a DI Nanoscope IIIa (Digital Instruments, now Bruker, Germany) mounted on a Zeiss Axiovert 135 inverted microscope (Carl Zeiss Microscopy GmbH, Jena, Germany) in semi-contact mode using Budget Sensors (Innovative Solution Bulgaria Ltd., Bulgaria) Al-Reflex Tap300Al-G cantilevers with a tip radius of $< 10\,\text{nm}$, a resonance frequency of about $300\,\text{kHz}$ and a spring constant of $40\,\text{N/m}$ at room temperature in the dried state. For the sample preparation a silicon wafer (Siegert Wafer GmbH, Germany) was spincast with a PEI solution ($0.25\,\text{wt\%}$, $0.1\,\text{ml}$) and of a diluted microgel suspension ($c = 0.1\,\text{wt\%}$). Prior to the PEI-coating, the wafer was treated in a plasma cleaner (Zepto, Diener Electronics, Germany) and cleaned with ethanol (HPLC grade). The resulting images were analyzed with GWYDDION [170].

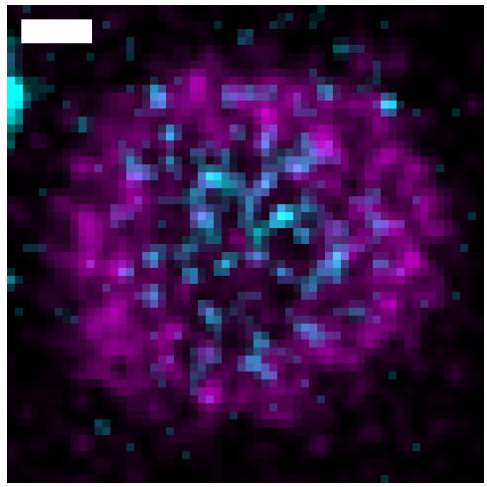

Figure A3.7.: Pseudo two color 2D representation of the core-shell microgel. Here, the localizations from a core microgel are represented with the cyan lookup table and the localizations from the core-shell microgel with a magenta lookup table. To generate this image two single microgels (core-only and core-shell image) were cut out and placed matching over each other. This image is only for visualization purposes. Scale bar: 100 nm.

A.4. Photoactivation localization microscopy of cardiomyopathy associated plakophilin-2 mutants

Human embryonic kidney cells (HEK293T) were cultivated in 1x DMEM with additional 50 ml fetal bovine serum and 5 ml penicillin-streptomycin per 1 l. For the PALM experiments the cells were cultivated in Nunc Lab-Tek chambers with # 1.5 glass coverslips or the equivalent μ-slides from Ibidi with eight wells. The cells were transfected with plasmids provided by Dr. Andreas Brodehl (Herz- und Diabeteszentrum, Bad Oeynhausen, Germany), where the constructs were fused to mEosFP thermo.

- pLenti-Puro-mEosFP-PKP2a
- pLenti-Puro-mEosFP-PKP2a-804x
- pLenti-Puro-mEosFP-PKP2a-715x
- pLenti-Puro-mEosFP-PKP2a-668x
- pLenti-Puro-mEosFP-PKP2a-628x
- pLenti-Puro-mEosFP-PKP2a-573x
- pLenti-Puro-mEosFP-PKP2a-459x
- pLenti-Puro-mEosFP-PKP2a-R350x

The transfections were accordingly done to the Lipofectamine 3000 reagent pro-

tocol with modified volumes. For the transfection of cells in four wells, two Eppendorf tubes were prepared with 40 μl Optimem in each tube. In the first tube 1.2 μl Lipofectamin 3000 was added and in the second 1.6 μl P3000 reagent. 2.96 μl (approximately 200 ng) of the plasmid was added to the tube with P3000 reagent. In the next step two tubes were mixed together and incubated for 10 min at room temperature. Afterwards 20 μl were added to each well with cells to transfect. A day later the transfection was controlled with a wide-field fluorescence microscope (GE Healthcare, DeltaVision). Typically, on the second day after transfection the HEK293T cells were imaged. Before imaging the cells are fixed with a 8% paraformaldehyde solution for 5 min at 37 C°. In the subsequent step the fixed cells were washed twice with PBS and stored with PBS in a fridge until usage.

A.5. Probing magnetic fields via super-resolved fluorescence microscopy

A.5.1. Sample preparation of single molecule surfaces investigating MFE on standard organic fluorophores

1. Ø 25 mm #1 (Menzel-Gläser, Thermo Scientific) coverslips were sonicated with 5% Hellmanex III (Hellma GmbH, Germany) at 40°C for at least 30 min. They were washed then with double distilled water (ddH_2O) and dried with compressed air.

2. The clean coverslip was placed in a stainless steel sample holder. To prepare the coverslip for dye immobilization, the glass surface is incubated in 200 μl bovine serum albumin (BSA) (A2153, Sigma-Aldrich Co) / Albumin, biotin labeled bovine (BSA-biotin) (A8549, Sigma-Aldrich Co, USA), fraction 3:1, for 12 h in a refrigerator at 4°C.

3. Subsequently, the BSA/BSA-biotin solution is washed off and the glass surface is then incubated with 200 μl streptavidin (S4762, Sigma-Aldrich Co,USA) dissolved in ddH2O for another 12 h in the fridge at 4°C.

4. After washing the streptavidin solution off the surface, 200 μl of a solution containing 10 nM Alexa Fluor 647 dye coupled to a 10mer of biotinylated single-stranded DNA (IBA GmbH, Germany), was placed on the coverslip and incubated for 2 h at 4°C.

5. The solution was aspired from the coverslip and was rinsed three times with Phosphate Buffered Saline Solution (PBS) to remove unbound fluorophores. Before imaging an buffer was added.

A.5.2. Sample preparation of SAMs on softferromagnetic multilayer systems

The preparation of SAMs on a softferromagnetic multi layer system is described in chapter 7.4.1. Further information about the SAM preparation can be found in the Bachelor thesis by Maren Eilers (Bielefeld University, Bielefeld, 2018).

A.6. dSTORM imaging buffer

All *d*STORM measurements were performed by using a special buffer system consisting of an enzymatic oxygen scavenging system (1 mg/mL glucose oxidase (Sigma Aldrich, USA), 20 μg/mL catalase (Sigma Aldrich, USA) and 10 % w/v glucose) through which the oxygen contained in the sample medium is temporally removed. Adding β-mercaptoethylamine (MEA-HCl, Sigma Aldrich, USA) to the buffer (until a concentration of 100 mM was achieved) results in an efficient blinking behavior of R6G. The pH is adjusted to 7.4 by adding highly concentrated (25 M) potassium hydroxide (KOH) to minimize pH dependent effects.

As an alternative to the mentioned simple standard glucose oxidase catalase buffer a high refractive index buffer based on glycerol can be used with the suggested components and concentrations [281]. The proposed benefits with this buffer are that the oxygen scavenging mechanism is enzyme free and prolongs up to 30 days.

Table A6.1.: Suggested composition for an enzyme free high refractive index switching buffer for long term acquisition and better quantitative comparison.

Component	Concentration
Glycerol	80%-90% v/v
β-mercaptoethylamine	100 mM
Sodium sulfite	35 mM
Double distilled water	for dilution

B. Acronyms

AFM Atomic force microscope
AOTF Acousto-optical tunable filter
APS Ammonium persulfate
BIS N,N'-Methylenebisacrylamide
CdSe Cadmium selenide
ddH_2O double distilled water
DNA Deoxyribonucleic acid
DSC2 Desmocollin-2
DSG2 Desmoglein-2
DSP Desmoplakin
dSTORM *direct* Stochastical optical reconstruction microscopy
EDTA Ethylenediaminetetraacetic acid
EMCCD Electron multiplying charged coupled device
ER Endoplasmatic reticulum
ERFC Error function
FCS Fluorescence correlation spectroscopy
FWHM Full width at half maximum
FRC Fourier ring correlation
GFP Green fluorescent protein
GODCAT Glucose oxidase catalase
HILO Highly inclined and laminated optical sheet
HOMO Highest occupied molecular orbit
HWHM Half width at half maximum
iSIM instant structured illumination microscopy
LUMO Lowest unoccupied molecular orbit
JUP Plakoglobin
LCST Lower critical solution temperature
KOH Potassium hydroxide
MEA β-Mercaptoethylamine
MFE Magnetic field effect
MINFLUX description
MOKE Magnteo-optical Kerr effect
NA Numerical aperture
NaCl Sodium chloride
NdFeB Neodymium magnet
NIPAM N-Isopropylacrylamide
NIPMAM N-isopropylmethacrylamide
NNPAM N-n-propylacrylamide
NNPMAM N-n-Propylmethacrylamid
NV Nitrogen vacancy
ODMR Optically detected magnetic resonance
OTF Optical transfer function
OR Overall resolution
PALM Photoactivation localization microscopy
PBS Phosphate buffered saline
PbS Lead sulfide
PCA Protocatechuic acid
PCD Protocatechuate dioxygenase
PCS Photon correlation spectroscopy
PKP2 Plakophilin-2
PSF Point spread function
Qdot Quantum dot
R6G Rhodamine 6G
RESOLFT Reversible saturable optical fluorescence transition
SANS Small angle neutron scattering
SIM Structured illumination microscopy
SLM Spatial light modulator
SMLM Single molecule localization microscopy
SOFI Stochastical optical fluctuation imaging
SRRF Super-resolution radial fluctuations
STED Stimulated emission depletion
STORM Stochastical optical reconstruction microscopy
TIR Total internal reflection
TIRF Total internal reflection fluorescence
TRABI Temporal, radial-aperture based intensity estimation
Trisma Tris(hydroxymethyl)aminomethane
VPTT Volume phase transition temperature

C. Publications

This work is based in major parts on the following peer reviewed publications:

Stephan Bergmann†, Oliver Wrede†, Thomas Huser and Thomas Hellweg. Super-resolution optical microscopy resolves network morphology of smart colloidal microgels.
Physical Chemistry Chemical Physics 20, 5074-5083 (2018)

O.W and S.B. wrote the manuscript. O.W. did the microgel syntheses, photon correlation spectroscopy, atomic force microscopy and fluorescence correlation spectroscopy. S.B. imaged and reconstructed the **d**STORM images of the microgels. S.B. wrote the 2D localization density script. O.W. and S.B. programmed the calculation for the 3D localization density recalculation. T.Hu and T.He did the proofreading and supervised the work.

Pia Otto†, Stephan Bergmann†, Alice Sandmeyer, Maxim Dirksen, Oliver Wrede, Thomas Hellweg and Thomas Huser. Resolving the internal morphology of core-shell microgels with super-resolution fluorescence microscopy. Nanoscale Advances 00, 0000-0000 (2019)

P.O. performed the syntheses of the microgels, performed the Photon Correlation Spectroscopy (PCS) experiments, and wrote parts of the manuscript. S.B. performed SMLM experiments, evaluated and reconstructed the related *d*STORM images and wrote parts of the manuscript. A.S. performed the SIM experiments and wrote parts of the manuscript. M.D. conducted the atomic force microscopy (AFM) measurements. O.W. wrote parts of the manuscript and structured the whole article. T.He and T.Hu supervised the work and proofread the manuscript.

Stephan Bergmann, Viola Mönkemöller and Thomas Huser Comment on "Magnetic-field-enabled resolution enhancement in super-resolution imaging" by M. Zhang et al., Phys. Chem. Chem. Phys., 2015, 17, 6722–6727

S.B performed all experiments and wrote the manuscript. V.M. introduced S.B. to SMLM. T.H proofread the manuscript and supervised the work.

(†equal contribution)

D. Acknowledgment

Diese Arbeit wäre nicht möglich gewesen ohne die Unterstützung vieler Menschen, die mich auf dem langen Weg begleitet haben.
Mein erste Dank gilt meinem Doktorvater Prof. Dr. Thomas Huser, der es mir erst ermöglicht hat diese Arbeit in seiner Arbeitsgruppe anzufertigen. Die gegebenen Freiheiten, die ich während der Promotion hatte, haben erst zu den vielfältigen Anwendungsgebieten von Einzelmoleküllokalisationsmikroskopie und deren Ergebnissen geführt.

Des Weiteren möchte ich Prof. Dr. Thomas Hellweg, Physikalischen Chemie III, Universität Bielefeld, für die sehr erfolgreiche Kooperation danken und für das Erstellen des Gutachtens zu dieser Dissertation. Der Einblick ins Innere von Mikrogelen ist faszinierend und ich erhoffe mir, dass der geebnete Weg zur Analyse von Mikrogelen mittels Fluoreszenzmikroskopie weiter beschritten wird. Es gibt noch viel zu erforschen.

Ein ganz besonderer Dank geht hier an Dr. Oliver Wrede, der die notwendigen Proben bereit gestellt hat und zusammen mit mir den neuartigen Pfad der Mikrogelanalyse eröffnet hat. In guter Erinnerung bleibt die Strahlzeit in Garching; Weißwurst und Hefeweizen zum Mittag gibt es auch nur an einer Uni in Bayern. Die vielen Abende in denen wir gemeinsam mit Jessica Klocke, Lena Bögeholz und Saskia Bannister verbracht haben, um erst mit mittelmäßigem Erfolg die Pandemie zu verhindern und anschließend die Welt aufzubauen.

Vielen Dank an Dr. Andreas Brodehl, vom Herz- und Diabeteszentrum in Bad Oeynhausen, für den Einstieg das extrem spannende und relevante Gebiet zur Erforschung von genetisch bedingten Herzkrankheiten. Hier hoffe ich, dass die gesammelten Erfahrungen und weitergehenden Entwicklungen der Mikroskope der Arbeitsgruppe zu weiteren Erkenntnissen führen kann.

In diesem Zusammenhang auch ein großes Dankeschön an Dr. Wolfgang Hübner, welcher vor Ort Hilfestellung bezüglich biologischer Fragestellungen leisten konnte und Experimente immer mit einer gesunden Portion Skepsis, über deren Sinnhaftigkeit, hinterfragt hat. Ich hoffe mein Sofa wird noch eine gute Zeit in Bielefeld verbringen.

Manch einer würde sagen ich habe "Magnetesoterik" betrieben, aber diese Arbeiten hatte nichtsdestotrotz ein Ergebnis. Für die vielen Arbeitsstunden, die ins Sputtern und Ätzen, sowie der Charakterisierung der magnetischen Oberflächen, geflossen sind vielen Dank an Dr. Karsten Rott und Dr. Niklas Dohmeier aus der

Arbeitsgruppe Dünne Schichten & Physik der Nanostrukturen.

Die wissenschaftlichen Erkenntnisse hätten nicht ohne das notwendige technische Know-How erlangt werden können. Seit mehr als sieben Jahr steht Dr. Gerd Wiebusch mit Rat und Tat zur Seite. Dank ihm hat die Laserquelle immer gute Dienste leisten können, auch wenn in letzter Zeit die Wartungsintervalle immer kürzer wurden. Vielen Dank für die zahlreichen "Streicheleinheiten" am Laser.

Gemeinsam haben wir den Aufbau des X-Gebäudes beobachten können, haben Abstellräume in Büros verwandelt und werden dann fast zur selben Zeit die Promotion abschließen und irgendwie konsequent zur ähnlichen Zeit in Bonn beginnen. Es war eine verrückte Zeit, negativ Tassen gegen positiv Tassen, Besonnenheit gegen impulsiven Charakter. Dementsprechend ein ganz besonderes Dankeschön gilt Alice Sandmeyer für die sehr gute Büroatmosphäre und Zusammenarbeit.

Bei optomechanischen Problemen sind Dr. Christian Pilger und Henning Hachmeister immer eine große Hilfe gewesen und der Kaffee war immer hervorragend, konnte aber nicht mit dem selbstgebrautem Bier konkurrieren. Vielen Dank.

Außerdem möchte ich noch bei ehemaligen Mitgliedern der Arbeitsgruppe Biomolekulare Photonik bedanken, allen voran Dr. Robin Diekmann, der mit Rat und Tat der "Bling Bling"-Fraktion immer geholfen hat und dies auch immer noch tut. Vielen Dank für die gemeinsame Zeit im Büro und im Labor und das Einführen der morgendlichen Kaffeerunde. Ein Dankeschön an Dr. Viola Mönkemöller, speziell zu Beginn der Promotionszeit für die Hilfestellung bei den Mikrogelen und den magnetischen Oberflächen. Dr. Matthias Simonis ist der Begründer der legendären Obstschale, welche nur einmal mit Obst gefüllt war. Seine Gelassenheit war immer beeindruckend.

Natürlich geht auch ein riesiges Dankeschön an die aktuellen Mitglieder der Arbeitsgruppe. Die unvergessenen Abende mit Bierverkostung, Halloweenfilmabend ("Bong of the dead") oder der norwegischen Tradition des Lønningspils mit anschließender Einkehr ins "Wohnzimmer", daher ein großes Dankeschön an Anders, Alex, Luis, Maren, Jakub, Henning, Julian, Kathi und Gabriel.

Für die Ablenkung vom Alltag haben immer Daniel, Hauke und Alice sorgen können, sei es durch Mountainbike fahren oder in einer langen Sitzung der Mars mal wieder terraformed wird oder Tränke gebraut und deren Ergebnisse publiziert werden können. Die abendlichen Filmsitzungen mit "großartigen" Filmen oder das frequentierte verlieren bei Innovation werde ich definitiv vermissen. Es war eine großartige Zeit. Vielen Dank dafür!

Meiner Familie gilt ein ganz besonderer Dank für die Unterstützung während des gesamten Studiums und für die Ermutigung meinen eigenen Weg zu gehen.

Mein finaler Dank gilt einer ganz besonderen Person, die eine sehr große Stütze über das gesamte vergangene Jahr war und mein Leben bereichert. Yey Motivation :). Danke für alles Maren.

E. Statutory declaration

Hiermit erkläre ich,

- dass mir die geltende Promotionsordnung der Fakultät für Physik der Universität Bielefeld bekannt ist.
- dass ich die vorliegende Dissertation selbst angefertigt, dabei keine Textabschnitte von Dritten oder eigenen Prüfungsarbeiten ohne Kennzeichnung übernommen und alle von mir benutzten Hilfsmittel und Quellen in der Arbeit angegeben habe.
- dass Dritte weder unmittelbar noch mittelbar geldwerte Leistungen von mir für Vermittlungstätigkeiten oder für Arbeiten erhalten habe, die im Zusammenhang mit dem Zustandekommen oder dem Inhalt dieser Dissertation stehen.
- dass ich diese Dissertation oder wesentliche Teile daraus nicht als Prüfungsarbeit für eine staatliche oder andere wissenschaftliche Prüfung eingereicht habe.
- dass ich die gleiche, eine in wesentlichen Teilen ähnliche oder eine andere Abhandlung bei einer anderen Hochschule als Dissertation eingereicht habe.

Bielefeld, 11. Dezember 2019

Stephan Bergmann